2014-10-07

Characterizing Susceptibility Weighted MRI in the Experimental Autoimmune Encephalomyelitis Mouse Model of Multiple Sclerosis

Nathoo, Nabeela

UNIVERSITY OF CALGARY

Characterizing Susceptibility Weighted MRI in the Experimental Autoimmune Encephalomyelitis Mouse Model of Multiple Sclerosis

by

Nabeela Nathoo

A THESIS

SUBMITTED TO THE FACULTY OF GRADUATE STUDIES

IN PARTIAL FULFILMENT OF THE REQUIREMENTS FOR THE

DEGREE OF DOCTOR OF PHILOSOPHY

GRADUATE PROGRAM IN NEUROSCIENCE

CALGARY, ALBERTA

OCTOBER, 2014

Abstract

Susceptibility-based magnetic resonance imaging (MRI) methods have been used in multiple sclerosis (MS) patients for lesion detection, visualization of the venous vasculature and to show abnormal iron accumulation in the deep grey matter structures of the brain. The overarching goal of this thesis was to characterize one of the susceptibility-based MRI methods, susceptibility weighted imaging (SWI), in the experimental autoimmune encephalomyelitis (EAE) mouse model of MS. First, we investigated if SWI could detect lesions (or hypointensities) in the lumbar spinal cords and cerebella of EAE mice. We found that SWI hypointensities were present in a region-specific manner in the CNS of EAE mice, where most of these lesions were attributed to deoxyhemoglobin and a smaller number were due to parenchymal iron deposition. Next, we validated a method to identify deoxyhemoglobin-based SWI hypointensities *in vivo* which entailed combining SWI with hyperoxygenation. Following this, we sought to investigate when SWI hypointensities appear during the EAE disease course and how they change over the course of the disease. This was studied by carrying out serial SWI *in vivo* in naïve mice and mice immunized for EAE. Here, we found that SWI hypointensities are prominent before signs of motor dysfunction in EAE mice. SWI hypointensities were also observed to evolve over the disease course. Of note, the number of SWI hypointensities was always at a maximum before or at the same time as maximum motor dysfunction. Unlike EAE mice, the number of SWI hypointensities remained stable through all imaging time points in naïve mice, suggesting that SWI hypointensities are linked to EAE pathophysiology. Lastly we used SWI to assess treatment response to an anti-inflammatory treatment (dexamethasone) in EAE mice. This was carried out under the premise that SWI hypointensities may be linked

to inflammation, so reducing inflammation could reduce the number of SWI hypointensities present. Our preliminary data suggest that SWI may be able to act as a surrogate marker of inflammation. Overall, findings from this thesis support the use of SWI in future studies in the EAE model to investigate the venous vasculature and parenchymal iron deposition.

Preface

Portions of the work presented within this thesis have been published previously in peer-reviewed journals.

Portions of the text in Chapter 1 have been revised from a published review article listed below. All portions of text were written by NN.

Nathoo N, Yong VW, Dunn JF (2014) Using magnetic resonance imaging in animal models to guide drug development in multiple sclerosis. *Multiple Sclerosis J.* 20(1):3-11.

Portions of the text in Chapter 1 have been used or revised from a published review article. Table 1.3 was fully taken from the article listed below. Text was written by NN.

Nathoo N, Yong VW, Dunn JF (2014) Understanding disease processes in multiple sclerosis through magnetic resonance imaging studies in animal models. *NeuroImage: Clinical* 4:743-756.

Portions of the text in Chapter 1 and Chapter 7 have been used or revised from a published review article. Tables 1.4 and 1.5 were fully or partially taken from the article listed below. Text was written by NN and ES.

Stephenson E, **Nathoo N**, Mahjoub Y, Dunn JF, Yong VW (2014) Iron in multiple sclerosis: roles in neurodegeneration and repair. *Nature Reviews Neurology* 10:459-468.

Portions of the text and figures in Chapter 3 have been used from a published article. Figures 3.2 through 3.9 were fully or partially published in the journal listed below. All experiments and portions of text and figures used were written or prepared by NN.

Nathoo N, Agrawal S, Wu Y, Haylock-Jacobs S, Yong VW, Foniok T, Barnes S, Obenaus A, Dunn JF (2013) Susceptibility-weighted imaging in the experimental autoimmune encephalomyelitis model of multiple sclerosis indicates elevated deoxyhemoglobin, iron deposition and demyelination. *Multiple Sclerosis J*. 19(6):721-731.

Acknowledgements

First and foremost, I would like to thank my supervisor, **Dr. Jeff Dunn**, not only for being an amazing supervisor, but also for being an excellent mentor. Thank you for having so much faith in me and for providing an environment where I could thrive. Thank you for pushing me beyond what I thought were my limits, as you helped me aim for excellence. I will always cherish the numerous conversations we shared in your office that kept me excited about science and research.

I would also like to thank my co-supervisor, **Dr. V. Wee Yong**, for being an amazing mentor from day one, long before you were my co-supervisor. Thank you for opening your lab and resources to me. I am grateful to you for including me in your lab meetings, as it was in that setting that I learned a substantial amount about neuroimmunology. Lastly, thank you for always, without fail, setting an example of what it means to be an incredible scientist.

Thank you to my other thesis committee members, **Drs. Shalina Ousman and Mark Swain**, for your support and guidance throughout the last few years. I appreciate that you pushed me to be more thorough in my scientific pursuits and to think outside the box.

Thank you to my internal-external examiner, **Dr. Penny Pexman**, and my external examiner, **Dr. Alan Wilman**, for taking the time to serve as examiners for my thesis defense.

Thank you to my funding sources, the **Multiple Sclerosis Society of Canada** and **Alberta-Innovates Health Solutions**, for supporting my research.

A special thanks to the **Dunn lab** – my lab family. Thank you for your encouragement and assistance over the years, and for sharing your excitement of science and research with me. You have been such a fun and interesting bunch to work with.

Thank you also to my co-supervised lab, the **Yong lab**, for making me feel like one of your own. Thank you for teaching me anything and everything about the EAE model, for our collaborations, and for being around to bounce ideas off of.

Thank you also to **Dr. Quentin Pittman and the Pittman lab** for making me feel like I had a third lab I was working in, both with respect to science and otherwise. Thank you for letting me learn from you, for using your equipment and for being a great bunch to socialize with.

Thank you to **Dave Kirk, Dave Rushforth and Tad Foniok** in the Experimental Imaging Centre for your help with the 9.4T system and for sharing your expertise with me; it was greatly appreciated.

I'd like to thank **my friends**, both those inside and outside of research, for your support and for being there for me for the last four years. It has been wonderful to share this journey with you.

Last, but certainly not least, I would like to thank **my family**. Thank you for your incredible support on a daily basis; words cannot express how much this has meant to me.

Dedication

To my incredible family – for your love, guidance, support, and for nurturing my love of neuroscience for many years.

Table of Contents

List of Tables

List of Figures

List of Abbreviations

Abbreviation	Definition
ANOVA	Analysis of variance
CFA	Complete Freund's adjuvant
CIS	Clinically isolated syndrome
CNR	Contrast to noise ratio
CNS	Central nervous system
CSF	Cerebrospinal fluid
DAB	3,3-diaminobenzidine
Dex	Dexamethasone
DMT	Disease modifying therapy
DTI	Diffusion tensor imaging
EAE	Experimental autoimmune encephalomyelitis
EDSS	Expanded disability status scale
FID	Free induction decay
FITC	Fluorescein isothiocyanate
FLASH	Fast low angle shot
Gd	Gadolinium
GEFC	Gradient echo with flow compensation
Gf	Gadofluorine M
HIF-1α	Hypoxia-inducible factor 1 alpha
IκBα	Inhibitor of nuclear factor kappa-light-chain-enhancer of activated B cells
IL-1β	Interleukin-1 beta

IFN-γ	Interferon gamma
i.p.	Intraperitoneal
MBP	Myelin basic protein
MEMRI	Manganese-enhanced MRI
MOG	Myelin oligodendrocyte glycoprotein
MRI	Magnetic resonance imaging
mRNA	Messenger ribonucleic acid
MRS	Magnetic resonance spectroscopy
MS	Multiple sclerosis
MTI	Magnetization transfer imaging
MTR	Magnetization transfer ratio
NAA	N-acetylaspartate
NAWM	Normal-appearing white matter
NF-κB	Nuclear factor kappa-light-chain-enhancer of activated B cells
NMR	Nuclear magnetic resonance
OEF	Oxygen extraction fraction
PET	Positron emission tomography
PLP	Proteolipid protein
PPMS	Primary progressive MS
PTX	Pertussis toxin
QSM	Quantitative susceptibility mapping
RF	Radiofrequency

ROS	Reactive oxygen species
RRMS	Relapsing-remitting MS
SEM	Standard error of the mean
SPMS	Secondary progressive MS
SWI	Susceptibility weighted imaging
TE	Echo time
TMEV	Theiler's murine encephalomyelitis virus
TNF-α	Tumour necrosis factor alpha
TR	Repetition time
USPIO	Ultrasmall superparamagnetic iron oxide
VCAM-1	Vascular cell adhesion molecule 1
VLA-4	Very late antigen-4

Chapter One: Introduction

1.1 Multiple sclerosis: general overview

Multiple sclerosis (MS) is a neurological condition characterized by inflammation, demyelination and neurodegeneration. At present, the cause of MS is unknown. MS is present in over 100 countries worldwide. Canada has one of the highest rates of MS in the world (2008).

There is great heterogeneity in the MS disease course. Over time, four main classifications of MS have emerged: relapsing-remitting MS (RRMS), secondary progressive MS (SPMS), primary progressive MS (PPMS) and progressive relapsing MS. RRMS is characterized by clearly defined periods of attacks (relapses) (Lublin and Reingold, 1996). A relapse is defined as a period of at least 24 hours where a patient has reported worsening of symptoms and/or where there are objectively observed signs indicative of an acute inflammatory, demyelinating event in the central nervous system (CNS) without the presence of fever or infection (Polman et al., 2011). Common MS symptoms include sensory disturbances in the limbs, ataxia and optic nerve dysfunction (Goodin et al., 2002), to name a few. Following relapses, full recovery may result, or there may be residual deficit upon recovery (Lublin and Reingold, 1996).

Approximately 65% of patients with RRMS transition to SPMS (Compston and Coles, 2008) which consists of progression with fewer relapses and minor remissions (Lublin and Reingold, 1996). PPMS is progressive from onset without remissions, or with temporary minor improvements (Lublin and Reingold, 1996). Progressive relapsing MS is also progressive from onset but has clear relapses (like in RRMS) with or without full recovery (Lublin and Reingold, 1996).

There is also a classification called clinically isolated syndrome (CIS) where one has experienced a demyelinating episode, but a second episode has not occurred yet, so the patient cannot be defined as having clinically definite MS. Between 30-70% of those with CIS ultimately transition to being classified as having clinically definite MS (Miller et al., 2005).

Although there is no cure for MS, there are a number of treatments available which affect the pathophysiology of the disease to benefit the patient, referred to as disease modifying therapies (DMTs) (Cummings, 2009). There are nine DMTs approved by Health Canada: interferon beta-1a (Avonex, Rebif), interferon beta-1b (Betaseron, Extavia), glatiramer acetate (Copaxone), natalizumab (Tysabri), teriflunomide (Aubagio), fingolimod (Gilenya) and dimethyl fumarate (Tecfidera). These agents have been shown to reduce the number of relapses in MS patients (Saidha et al., 2012), but do not cure the disease. Corticosteroids such as methylprednisolone and dexamethasone (dex) are commonly used to treat relapses in MS, and have been shown to help accelerate recovery from relapses (Myhr and Mellgren, 2009). However, whether they have any long term beneficial effects in MS patients is unknown.

Diagnosis of MS is challenging and often occurs by a process of excluding other possible causes for a patient's symptoms. Currently the McDonald criteria (which have been revised twice, in 2005 and 2010) are used in diagnosing patients with MS, with magnetic resonance imaging (MRI) playing a major role in the process of diagnosis. The criteria for diagnosing one with MS involves the dissemination of lesions in both space and time (McDonald et al., 2001). The 2010 McDonald criteria for showing the dissemination of lesions in space is demonstrated by having ≥ 1 T_2 lesion in at least two of four areas of

the CNS (periventricular, juxtacortical, infratentorial and spinal cord) (Polman et al., 2011) (**Figure 1.1**). The 2010 McDonald MRI criteria for showing the dissemination of lesions in time can be demonstrated with a new T_2 and/or gadolinium (Gd)-enhanced lesion on a follow up MRI with reference to a baseline scan, or by the simultaneous presence of asymptomatic Gd-enhancing and non-enhancing lesions (T_2 lesions) at any time (Polman et al., 2011) (**Figure 1.2**). These revised McDonald criteria are only applicable to those that show a typical presentation of CIS (Polman et al., 2011). MRI plays an essential role in our ability to diagnose MS and to monitor disease progression non-invasively. As a result, MRI methods are constantly being developed to improve our ability to diagnose MS, to examine the efficacy of treatment regimens by monitoring MRI lesion load over time, and to learn more about MS pathophysiology.

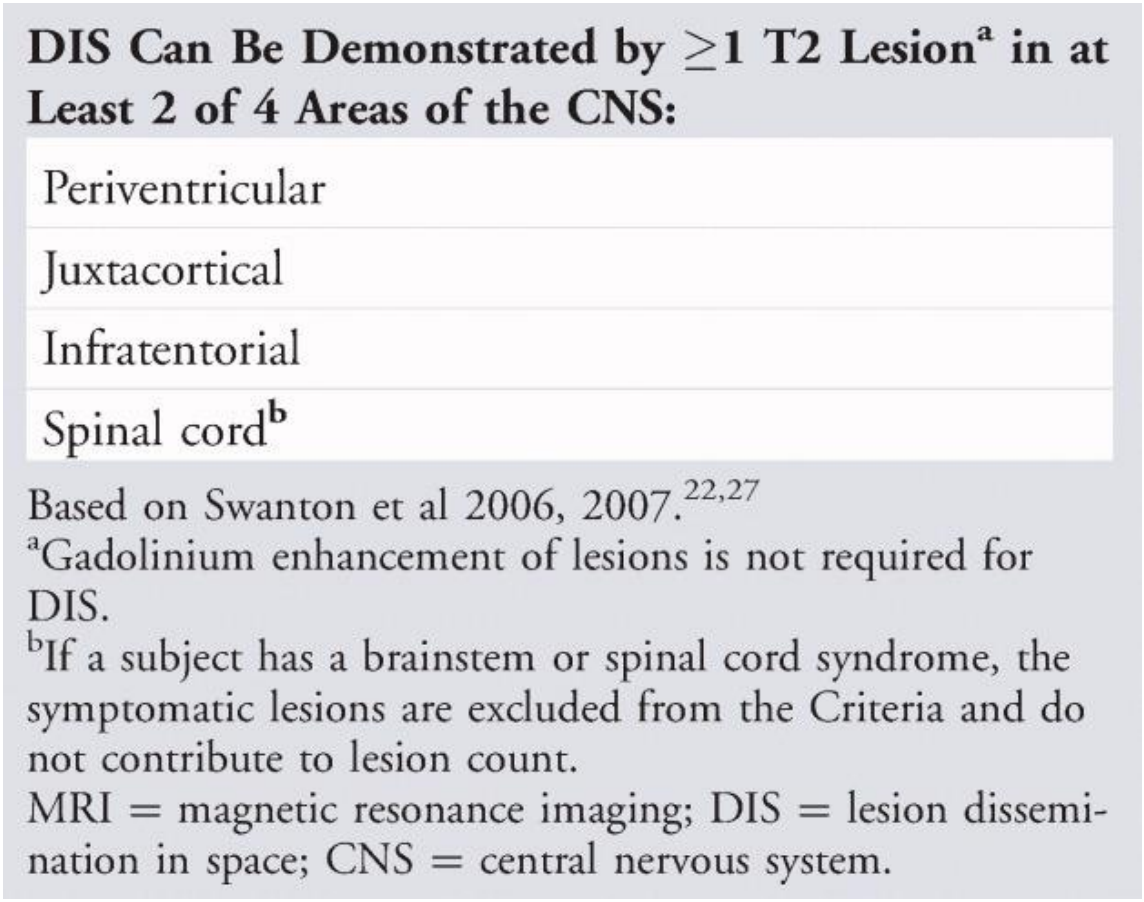

DIS Can Be Demonstrated by ≥1 T2 Lesion[a] in at Least 2 of 4 Areas of the CNS:
Periventricular
Juxtacortical
Infratentorial
Spinal cord[b]

Based on Swanton et al 2006, 2007.[22,27]
[a]Gadolinium enhancement of lesions is not required for DIS.
[b]If a subject has a brainstem or spinal cord syndrome, the symptomatic lesions are excluded from the Criteria and do not contribute to lesion count.
MRI = magnetic resonance imaging; DIS = lesion dissemination in space; CNS = central nervous system.

Figure 1.1 2010 McDonald criteria describing dissemination in space of lesions using MRI. Adapted from (Polman et al., 2011) which includes references to (Swanton et al., 2006; Swanton et al., 2007)

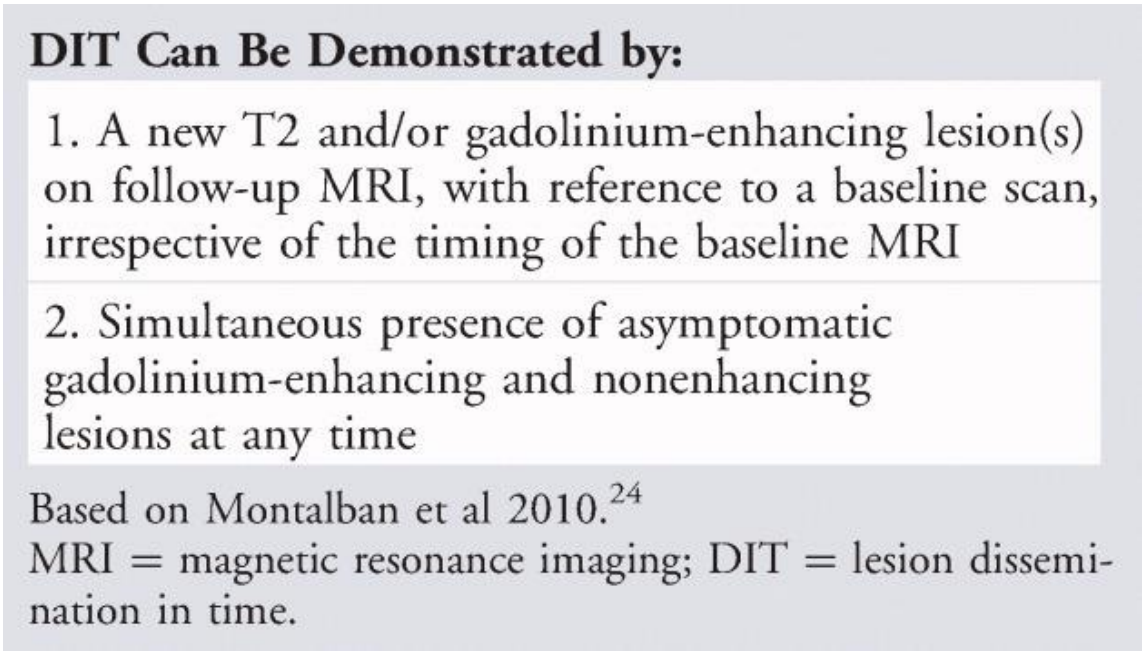

Figure 1.2 2010 McDonald criteria describing dissemination in time of lesions using MRI. Adapted from (Polman et al., 2011) which includes reference to (Montalban et al., 2010)

1.2 Experimental autoimmune encephalomyelitis (EAE) and other animal models used to study MS

There are five main animal models used to study MS: experimental autoimmune encephalomyelitis (EAE), Theiler's murine encephalomyelitis virus (TMEV), cuprizone, lysolecithin and ethidium bromide. Each of these animal models offers different potential routes to investigate MS disease processes. The EAE model provides the opportunity to study inflammation, demyelination and axonal loss initiated by an autoimmune response to central nervous system (CNS) components. Viral models, like those induced by TMEV, enable examination of an immune response to a viral infection leading to demyelination. Demyelinating models caused by toxins such as lysolecithin, cuprizone and ethidium bromide afford the opportunity to investigate a primary demyelinating insult.

TMEV is a member of the Picornaviridae family of RNA viruses. Administering TMEV intracerebrally in susceptible mouse strains (like SJL/J) leads to demyelination (Dal Canto et al., 1996; Denic et al., 2011). Typically the disease is either monophasic or biphasic – the biphasic condition shows chronic demyelination (presenting as chronic-progressive), leading to the development of spinal cord lesions, similar to those observed in EAE (Dal Canto et al., 1996; Denic et al., 2011).

The cuprizone model is often employed to study specific aspects of demyelinating and remyelinating events in MS. Cuprizone is a copper chelator which, when consumed in an animal's diet, produces demyelination in the corpus callosum and superior cerebellar peduncles (Blakemore, 1973; Matsushima and Morell, 2001); cortical demyelination has also been observed (Skripuletz et al., 2008). Acute demyelination involves ingestion of cuprizone for six weeks followed by a normal diet for six weeks. This paradigm leads to

demyelination followed by spontaneous remyelination (Matsushima and Morell, 2001). Chronic demyelination results if cuprizone ingestion takes place for 12 consecutive weeks (Matsushima and Morell, 2001).

The lysolecithin model produces a demyelinating lesion via injection of an activator of phospholipase A2, lysophosphatidylcholine, into a specific area in the CNS, including the dorsal and ventral columns of the spinal cord, corpus callosum and internal capsule (Denic et al., 2011). The lysolecithin model involves demyelination and remyelination following a known disease course that lasts roughly one month; demyelination peaks at around day 7 and remyelination can be seen by day 10 (Aldskogius and Fraher, 2002).

Ethidium bromide is a toxic agent that can be injected into the dorsal column of the spinal cord or in the caudal cerebellar peduncle (Merrill, 2009). Its mechanism of action involves intercalation with nucleic acids, effectively injuring any cells containing a nucleus (Waring, 1965; Merrill, 2009). Demyelination induced by ethidium bromide is at a maximum approximately two weeks after injection (Graca and Blakemore, 1986). Remyelination takes longer to manifest in this model compared to the lysolecithin model, with extensive remyelination not being seen until around 3.5 months after injection (Woodruff and Franklin, 1999).

EAE is a model of chronic inflammation, and is the animal model used most often to investigate MS. Many variants of the EAE model exist that can display monophasic, relapsing-remitting, chronic-progressive or chronic-relapsing disease courses depending on the animal strain and immunogen used. Taken together, the diverse types of EAE models present the spectrum of clinical phenotypes observed in MS (Kipp et al., 2012). However, no EAE model appears to represent PPMS accurately. EAE immunization uses

components of the CNS which stimulate the immune system via antigen presentation and autoimmunity. The antigen may be from CNS homogenate or purified myelin peptides, such as myelin basic protein (MBP), myelin oligodendrocyte glycoprotein (MOG), or proteolipid protein (PLP). This results in an autoimmune condition which targets myelin. EAE has been induced and examined across species with earlier studies focusing on non-human primates. Rodent models, particularly those using mice, are now more commonly used due to the affordability and availability of genetically modified murine strains (Ransohoff, 2012).

MS and EAE share several characteristics, including the destruction of myelin sheaths and axonal degeneration (Steinman and Zamvil, 2005). In addition, numerous CNS lesions are present which are distributed in space and time (Adams and Kubik, 1952; Baxter, 2007). MS and several variant models of EAE have evidence supporting a genetic susceptibility influenced by major histocompatibility complex class II haplotype (Steinman and Zamvil, 2005). Furthermore, CD4+ and CD8+ T-cells can be seen in lesions in both conditions, some of which are reactive to myelin proteins (Steinman and Zamvil, 2005). T helper cell subsets, particularly Th1 and Th17 cells, play roles in both EAE and in MS (Fletcher et al., 2010). At the molecular level, the process of leukocyte migration into the CNS appears to be similar in EAE to that in MS (Agrawal et al., 2011). For example, activated leukocytes roll and adhere onto endothelial cells via adhesion molecules, and then ultimately cross the glia limitans to enter the CNS parenchyma (Agrawal et al., 2006). The vast majority of MRI studies with animal models of MS have used the EAE model. Importantly, the EAE model shows the same clinico-radiological paradox seen in MS,

where MRI lesion load does not always correspond to the level of clinical disability (Wuerfel et al., 2007).

Histopathology in the EAE model varies depending on the immunogen used. A few studies have thoroughly investigated histopathology in the MOG EAE model to be used in this thesis, which will be described here – these studies have been carried out in the spinal cord only. Meningeal and parenchymal infiltration, as well as edema, are seen at peak disease in the spinal cord (Recks et al., 2011). In the chronic stage (3 months post-immunization in the cited study), inflammation is reduced, but myelin and axon pathologies are visible (Recks et al., 2011). By the long-term time point (defined as 6 months in the cited study), severe neurodegeneration can be seen after myelin and axonal debris have been removed and inflammatory infiltrates are no longer seen (Recks et al., 2011).

Another histopathology study of the MOG EAE model found that axonal loss can be detected as early as 7 days post-immunization in the dorsal column of the spinal cord, before any signs of motor disability (Jones et al., 2008). Axon numbers appear to be at a minimum 30 days post-immunization and remain at these values, even up to 1 year post-immunization (Jones et al., 2008). T lymphocytes can be seen infiltrating the dorsal column of the spinal cord as early as 7 days post-immunization, although their levels peak at the 12 day time point (Jones et al., 2008). Microglial activation is not significantly increased at the 7 day time point, but peaks at 12 days (Jones et al., 2008). Demyelinating lesions are seen around submeningeal veins and large vessels in the medial dorsal and ventral columns as well as the lateral columns (Jones et al., 2008). Infiltrating cells do not

seem to associate much with parenchymal vessels nor with grey matter (Jones et al., 2008). Significant myelin loss is seen at 30 days post-immunization (Jones et al., 2008).

The EAE model has proven to be remarkably valuable in MS research with respect to medications for the condition; three DMTs have been developed using this model: glatiramer acetate, mitoxantrone and natalizumab (Steinman and Zamvil, 2006). Most, if not all, therapeutic agents for MS are tested at a preclinical stage using EAE to determine if they are effective in the animal model before being applied to the patient population. Furthermore, EAE has been useful for identifying novel pathways in the pathogenesis of autoimmune disease *in vivo* (Steinman and Zamvil, 2005) and for characterizing inflammation and components of immune surveillance in the central nervous system (Baxter, 2007). Similarities between EAE and MS are summarized in the table below (**Table 1.1**).

There are, however, a number of pitfalls experienced with use of the EAE model. The clinical complications of some of the drugs developed using the EAE model (e.g. progressive multifocal leukoencephalopathy with natalizumab (Langer-Gould et al., 2005)) were not known until the drug was applied in humans – the results from animal studies did not uncover such potential risks (Baxter, 2007). In addition, some treatments that worked in EAE actually exacerbated MS, with the most prominent examples being interferon gamma (IFN-γ) and anti-tumour necrosis factor alpha (anti-TNF-α) (Steinman and Zamvil, 2005). Another significant limitation experienced using the EAE model is that studies using EAE are often conducted over a short time period; EAE experiments last weeks in the acute phase and only months in the chronic phase (Steinman and Zamvil, 2005). These short-lived experiments do not accurately portray the disease course of MS which is

chronic and evolves over many years. In addition, by not using an extended length of time for EAE studies, the problems that may arise after months or years of a potential therapy cannot be predicted (Steinman and Zamvil, 2005). Disadvantages of the EAE model are summarized in the table below (**Table 1.2**).

The specific EAE model used for this thesis project is the standard model using active immunization (with MOG_{35-55}), where the disease is monophasic (not relapsing-remitting) and is characterized by chronic inflammation and demyelination. This model results in paralysis originating from the tail moving up the spinal cord towards the head, thereby affecting potentially the tail, hind limbs and fore limbs, where paresis of the limbs takes place. In addition, this model was chosen as it is reliable (it has been used in the lab regularly), and it mimics important elements of MS, namely inflammation, demyelination and axonal degeneration.

Table 1.1 Similarities between MS and EAE

Adapted from (Steinman and Zamvil, 2005)

Characteristic	EAE	MS
Genetic susceptibility	Strong association with MHC II	Strong association with MHC II
	Females more susceptible in certain strains	Females more susceptible
Environmental triggers	Relapses with earlier infection; superantigens trigger relapses	Association with earlier infection
White matter	Th1 T cells, B cells, CD4 and CD8 T cells, B cells and antibodies to myelin in lesions	Th1 T cells, B cells, CD4 and CD8 T cells, B cells and antibodies to myelin in lesions
	Clonal CD4 and CD8 T cells reactive to myelin	Clonal CD4 and CD8 T cells reactive to myelin components
	Macrophages	Macrophages
	Microglia	Microglia
	α4β1 integrin	α4β1 integrin
	Complement	Complement
Grey matter pathology	Axonal degeneration	Axonal degeneration
Clinical presentation	Optic neuritis, myelitis, periventricular white matter inflammation	Optic neuritis, myelitis, periventricular white matter inflammation
Clinical forms	Relapsing remitting	Relapsing remitting
	Progressive	Progressive

Table 1.2 Disadvantages of the EAE model

Characteristic	Disadvantage(s) of EAE model
Translating drugs that work in EAE to MS	Some drugs that work in EAE do not work in MS Some drugs that work in EAE exacerbate MS (e.g. anti-TNF-α, IFN-γ)
Predicting possible complications of drugs in MS	Fatal complications may not be predicted by drugs when used in EAE model which may affect MS patients (e.g. progressive multifocal leukoencephalopathy with natalizumab)
Progression of disease with respect to motor disability in EAE	EAE always has ascending paralysis, which is not reflective of motor disability progression in MS
Duration of experiments in EAE	Studies using EAE model are short-lived, which does not accurately represent decades-long disease course in MS patients
T cell subsets in EAE	EAE is typically CD4+ T cell driven, while MS has a substantial contribution of CD8+ T cells in disease
Cause of disease	EAE uses an outside-in mechanism, whereas how MS is initiated is unknown (i.e. outside-in vs. inside-out)

1.3 MRI

Only a cursory overview of the technical aspects of MRI is presented using sources listed here (McRobbie et al., 2003; Brown and Semelka, 2010; Schröder and Faber, 2011).

1.3.1 Basics principles of MRI

MRI is based on the principles of nuclear magnetic resonance (NMR), whereby nuclei with an odd number of protons and neutrons can be examined due to their interaction with an external magnetic field. In most instances, the hydrogen nucleus, with one proton (^{1}H), is studied, due to its abundance in the body in the forms of water and fat. However, other nuclei may also be studied, including ^{13}C, ^{17}O, ^{19}F and ^{23}Na. These nuclei exhibit the property of spin, whereby the nucleus rotates on its axis at a constant rate (like a spinning top), a process which is called precession. Each spinning nucleus behaves like a tiny bar magnet. For the sake of simplicity, the term 'spin' will be used to denote the hydrogen nucleus from here on in. The precession frequency (the Larmor frequency, denoted by ω) depends only on a constant which is different depending on the nucleus being observed (called the gyromagnetic ratio, denoted by γ, which is 42.57MHz/T for hydrogen) and the external magnetic field (B_0). This relationship is shown using the Larmor equation:

$$\omega = \gamma B_0$$

In the absence of B_0, spins are randomly oriented, leading to a vector sum of zero (**Figure 1.3a**). However, in the presence of B_0, spins align either with the magnet (parallel) or against the magnet (antiparallel) (**Figure 1.3b**). Due to the parallel state being the lower energy state, a small excess of spins align with the magnet, leading to a net magnetization

(M_0) in the z direction – this small excess of spins in one energy state is what drives MRI. For example, at 1.5T, there will be an excess of 1 x 10^6 protons out of the 10^{25} protons present in the tissue. In order to visualize this excess of spins, the system must be perturbed. This is achieved using a radiofrequency (RF) pulse with the same frequency as the one at which protons are precessing (the Larmor frequency, ω). This tips M_0 into the xy plane, and protons that were in the lower energy state absorb energy and move into the higher energy state, while protons in the higher energy state emit energy and move to the lower energy state. However, due to the small excess of protons starting off in the lower energy state, the system ultimately absorbs energy. In addition to the net magnetization being tipped into the xy plane, the protons also precess in phase with each other. Once the RF pulse is switched off, protons emit energy at the Larmor frequency ω, which can be detected with a loop of wire (receiver) in which a voltage will have been induced – this is known as the free induction decay (FID). The process by which protons emit energy and return back to their original state is referred to as relaxation. Protons in different tissues experience relaxation at different rates which forms the basis of contrast in MR images.

In order to localize where the MRI signal is coming from, spatial encoding is carried out using gradient coils that vary the magnetic field linearly in each of the three orthogonal directions (x, y, z). In addition to the abovementioned sources, there is a good review that explains these concepts more in-depth (Plewes and Kucharczyk, 2012), and so they will not be expanded upon here.

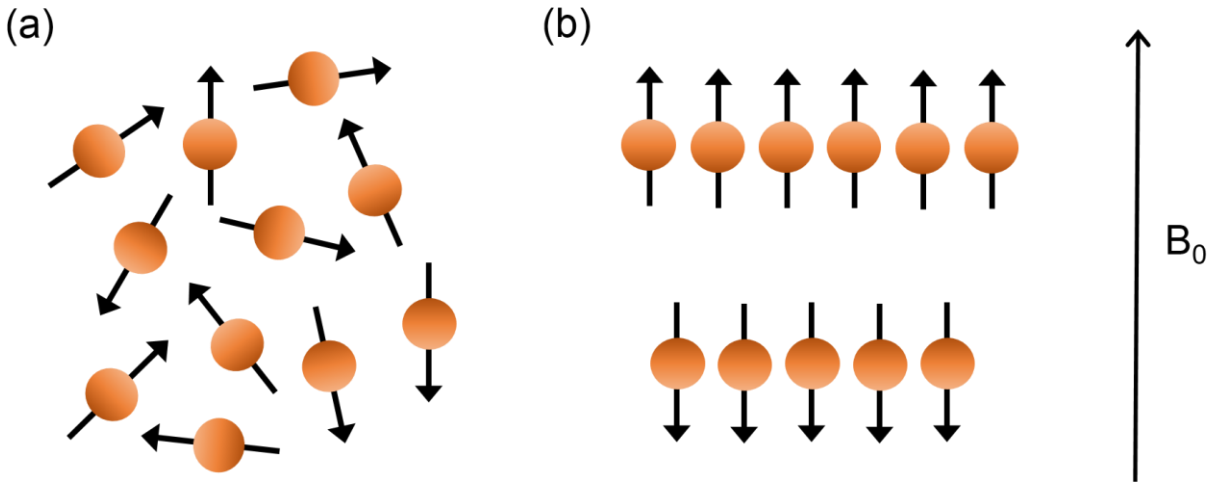

Figure 1.3 Spins in the absence and presence of an external magnetic field B_0. (a) Spins are randomly aligned in the absence of an external magnetic field. **(b)** Spins align parallel or antiparallel in the presence of an external magnetic field, with a small excess aligning with the field.

*1.3.2 T_1, T_2 and T_2**

As described, relaxation takes places after the RF pulse is switched off. This occurs by longitudinal or transverse mechanisms. One is called longitudinal relaxation, or spin-lattice relaxation and is referred to as T_1. This refers to the relaxation of protons from the xy plane back into the z direction to realign with B_0. The T_1 relaxation time is the time it takes for 63% of the net longitudinal magnetization (M_0) to be recovered. Tissues that transfer energy to their surroundings (lattice) efficiently (such as lipids) have a shorter T_1 relaxation time, whereas cerebrospinal fluid (CSF) has a longer T_1.

The second main relaxation mechanism is called transverse relaxation or spin-spin relaxation, and is referred to as T_2. Transverse relaxation refers to the dephasing of protons following the switching off of the RF pulse. The T_2 relaxation time is the time it takes for 63% of the transverse magnetization to be lost (decay). T_2 relaxation is always faster than T_1 relaxation, but the two relaxation processes occur independently of one another. Tissues that undergo efficient energy exchange with each other (such as lipids) have shorter T_2 relaxation times, while those that do not (like CSF) have longer T_2 relaxation times.

The third is associated with dephasing as well, similar to that in T_2, and is referred to as T_2*. T_2* is generally shorter than T_2 as it incorporates both the T_2 component as well as a dephasing component caused by static variations in the local magnetic field. These static variations are refocused when using spin echo, but not when using gradient echo (see section 1.3.3).

The terms T_1-weighted, T_2-weighted, and T_2*-weighted MRI refer to the manipulation of the pulse sequence to generate images that are sensitive to the specific type of relaxation of interest (T_1, T_2, T_2*).

1.3.3 Spin echo vs. gradient echo sequences

Spin echo and gradient echo sequences are two very common pulse sequences used to generate MR images. Spin echo sequences use at least two RF pulses – a 90° excitation pulse followed by a 180° refocusing pulse. Spin echo sequences are used for generating T_2-weighted images as the 180° refocusing pulse removes the effects of B_0 inhomogeneity and local susceptibility effects.

Gradient echo sequences, on the other hand, use an RF pulse<90° and instead use gradients to refocus the magnetization rather than a 180° refocusing pulse as is done in spin echo imaging. Because gradients are used to refocus the magnetization rather than the 180° refocusing pulse, the effects of B_0 inhomogeneity and susceptibility remain. However, the use of gradients for refocusing rather than 180° pulses and an RF pulse angle less than 90° allows for faster image acquisition in gradient echo sequences compared to spin echo sequences.

The effects of using a spin echo sequence versus a gradient echo sequence on spins is shown pictorially (**Figure 1.4**).

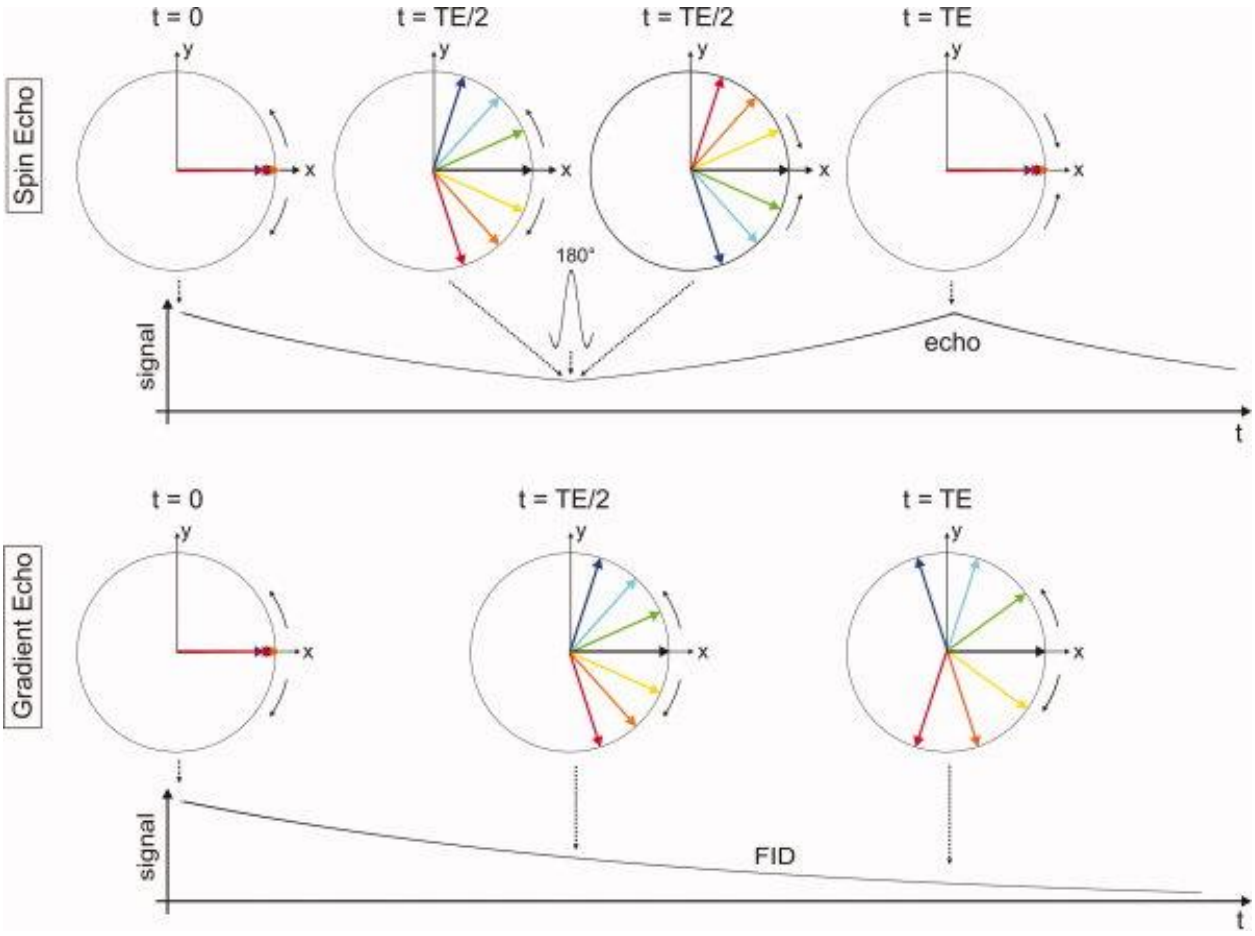

Figure 1.4 Effects of using a spin echo versus a gradient echo on signal formation. In the spin echo sequence (top), the 180° refocusing pulse enables for refocusing of the spins and magnetization due to removal of the effects of B_0 inhomogeneity and susceptibility. However, in the gradient echo sequence (bottom), the use of gradients does not remove effects of B_0 inhomogeneity and susceptibility, and so all of the spins do not necessarily realign for signal formation.

Adapted from (Markl and Leupold, 2012)

1.3.4 Parameters affecting MR signal

A number of parameters affect the signal obtained with MRI, including the field of view (FOV, given as length and width), matrix size (the number of partitions in the x and y directions), slice thickness and the number of averages. The FOV divided by the matrix in a given orthogonal direction provides the voxel size. For example, if the FOV_x is 256mm and the matrix in the x direction is 512, the voxel resolution in the x direction would be 256/512=0.5mm. The smaller the voxel size, the greater the spatial resolution obtained and so the easier it is to resolve structure; however, this comes at the price of signal, as the smaller the voxel, the less signal present. This can be offset by obtaining more averages, but that comes at the expense of scan time. As a rough rule of thumb, if you reduce the voxel volume by half (and so have half the number of protons), it will take four times longer in scan time to obtain the same signal-to-noise ratio (SNR). Thus, the factors that come into play for obtaining MRI are complicated, and trade-offs likely will take place, either when it comes to SNR or spatial resolution.

1.3.5 Field dependence of MRI

MRI of humans in the clinical setting is carried out at 1.5T or 3T, while 7T whole body systems are being used in some research centres. The highest field strength currently being used in humans in the research setting is 11.7T. Animal systems typically operate at higher field strength with the maximum currently being in excess of 20T. The push for higher field strengths comes from the notion that the higher the field strength, the greater the signal, by virtue of there being a greater excess of protons that align with the magnetic field strength that can be manipulated and detected with MRI. Overall, increasing magnetic

field strength increases the SNR. However, susceptibility effects also increase with increasing magnetic field strength which can be detrimental, particularly at air-tissue interfaces. For studies aiming to study local susceptibility effects though (e.g. due to iron accumulation in tissue), using higher field can be useful. It is worth noting that a higher magnetic field strength alone will not increase spatial resolution, as this is dependent on the strength of the gradients that carry out spatial encoding in the three orthogonal directions (x, y, z).

1.4 Overview of MRI methods that have been used in animal models of MS for studying MS disease processes and for assessing potential therapeutics for MS

Various MRI methods have been used in animal models of MS. Rodents have historically been used to test the sensitivity of MR methods to detect pathologies such as blood brain barrier (BBB) breakdown, inflammation, demyelination and white matter changes, and atrophy. Although detection thresholds may vary between patients and animals, in part due to the more variable pathologies in patients, imaging metrics that work in animals tend to work in patients.

BBB breakdown can be assessed using T_1-weighted MRI with Gd. In instances of BBB breakdown, Gd enters the brain parenchyma, leading to enhancement or hyperintensity (brightness) on T_1-weighted MRI. Gadofluorine M (Gf) can also be used to assess BBB breakdown, which has been shown to be more sensitive than Gd (Stoll et al., 2009). Gf gives bright contrast on T_1-weighted MRI and binds strongly to components of the extracellular matrix, including collagen and proteoglycans (Meding et al., 2007).

Inflammation can be studied at the cellular level with MRI using iron oxide-based nanoparticle contrast agents, such as ultrasmall superparamagnetic iron oxide (USPIO) particles, which range in size from 10-50nm. As iron is paramagnetic, accumulation of iron nanoparticles in tissue leads to hypointense (dark) signals on T_2 and T_2*-weighted MRI or hyperintense (bright) signals on T_1-weighted MRI. These nanoparticles can be used to label specific inflammatory cell populations. When delivered systemically, iron nanoparticles are taken up by monocytes circulating in the blood (Stoll and Bendszus, 2010). Iron nanoparticles are approved for human use and have been used in research studies with MS patients to track monocytes (Dousset et al., 2006; Vellinga et al., 2008), although these are currently being used off label. To the best of our knowledge, the only brand of iron nanoparticles approved by the US Food and Drug Administration is Ferumoxytol for iron therapy in chronic kidney disease (Lu et al., 2010).

Magnetization transfer imaging (MTI) is based on the ability of hydrogen protons in macromolecules (e.g. lipids, proteins), which are restricted in motion, to exchange with hydrogen protons in free water (Wolff and Balaban, 1989). In instances where membrane lipid content is reduced, magnetization transfer ratio (MTR) is decreased, as the number of bound hydrogen protons available to exchange magnetization with hydrogen in free water is reduced (Filippi and Rovaris, 2000).

Myelin water imaging, as the name suggests, is sensitive to myelin, and is based on the principle that the short component in T_2 is due to water trapped between the myelin lipid bilayer (MacKay et al., 1994; Laule et al., 2011). In instances where myelin is damaged or lost, myelin water content is reduced (MacKay et al., 1994).

Diffusion tensor imaging (DTI) uses the diffusion of water in tissue to relay information about tissue microstructure. The diffusion of water can be equal in all directions, which is termed isotropic diffusion (as would be seen in CSF), or it can be restricted in some directions due to the presence of barriers including axons and myelin, leading to anisotropic diffusion. Specific values, termed scalar measures, can be calculated from DTI datasets and have been shown to correlate with demyelination and axonal injury (Song et al., 2003).

Perfusion MRI can be used to provide measures of blood flow and blood volume. Dynamic contrast enhanced imaging is one type of perfusion imaging which tracks the movement of a bolus tracer passing through a capillary network by acquiring multiple images following injection of the bolus (Petrella and Provenzale, 2000).

Manganese-enhanced MRI (MEMRI) is used as a form of functional MRI where manganese contrast tracks along axons with functionally connected synapses (Aoki et al., 2004). MEMRI has not been used in humans due to the neurotoxicity of manganese (Silva and Bock, 2008).

Magnetic resonance spectroscopy (MRS) is useful for investigating metabolic alterations. In particular, it is frequently used for looking at n-acetylaspartate (NAA, a marker of neurons), choline (a marker of membrane integrity), creatine (a marker of energy metabolism) and myoinositol (a marker of glial cells) (Soares and Law, 2009).

1.5 MRI studies in animal models of MS for understanding MS disease processes

MRI studies in animal models of MS have been carried out for a number of purposes, including to assess pathology in models and to compare the imaging phenotypes

observed with what is seen in MS patients. The EAE model is the most extensively studied, which may be one of the reasons that such diverse pathology has been reported. A summary of pathologies and phenotypes seen in animal models of MS with MRI is shown below (Nathoo et al., 2014a) (**Table 1.3**).

MRI studies of models of MS have specific and obvious advantages. One advantage is the ability to image before and during disease progression in an individual animal. As a result, changes may be followed over time, ultimately reducing animal numbers and enabling one to compare within a single animal with statistics (Nathoo et al., 2014b).

A significant benefit of using MRI in animal model studies is that it allows for the development of methods that can be translated to clinical use. This includes the development of MRI sequences and new contrast agents. Examples of new contrast agents that are not yet approved in humans include Gf and contrast agents based on VCAM-1 and intercellular adhesion molecule-1. In EAE, Gf has shown areas of disrupted BBB (Bendszus et al., 2008; Wuerfel et al., 2010). Although Gd-enhanced MRI is currently the gold standard for assessing BBB breakdown with MRI in MS, Gf has been demonstrated to be more sensitive than Gd for this purpose (Stoll et al., 2009).

One of the contrast agents initially used in EAE that has been translated for use in MS patients is the iron-based USPIOs. Studies in EAE comparing BBB breakdown (using Gd or Gf) with infiltration of monocytes into the CNS (using USPIOs) have been particularly instructive, as they have commonly observed that there appears to be a mismatch between BBB breakdown and monocyte migration into the CNS (Rausch et al., 2003; Floris et al., 2004; Ladewig et al., 2009). Furthermore, some lesions are only

detected using USPIOs in EAE (Ladewig et al., 2009; Tysiak et al., 2009). In recent years, studies have been carried out in MS patients comparing Gd with USPIOs (Dousset et al., 2006; Vellinga et al., 2008; Tourdias et al., 2012). Remarkably, these human studies have come to the same conclusion as animal studies – USPIOs may be present in areas that appear to have an intact BBB as they do not show Gd-enhancement (Dousset et al., 2006; Vellinga et al., 2008; Tourdias et al., 2012).

Table 1.3 Summary of pathologies and MRI phenotypes in animal models of MS

Adapted from (Nathoo et al., 2014a)

Animal model	Pathology	MRI method(s) and phenotype	References
EAE	BBB breakdown	Enhancement with Gd	(Kuharik et al., 1988; Karlik et al., 1993; Hart et al., 1998; Cook et al., 2005; Blezer et al., 2007; Nessler et al., 2007; Smorodchenko et al., 2007; Wuerfel et al., 2007; Waiczies et al., 2012)
		Enhancement with Gf	(Bendszus et al., 2008; Wuerfel et al., 2010)
	Inflammation	Hypointensities with T_2- or T_2*-weighted MRI or hyperintensities in T_1-weighted MRI in combination with iron nanoparticles	(Xu et al., 1998; Dousset et al., 1999; Brochet et al., 2006; Oweida et al., 2007; Wuerfel et al., 2007; Chin et al., 2009; Tysiak et al., 2009; Engberink et al., 2010; Millward et al., 2013)
	White matter changes	Decrease in MTR	(Blezer et al., 2007; Rausch et al., 2009; Aharoni et al., 2013)
		Decrease in myelin water fraction	(Gareau et al., 2000)
	Axonal damage	Black holes on T_1-weighted MRI	(Nessler et al., 2007)
		Decrease in axial diffusivity with DTI	(Budde et al., 2008; Budde et al., 2009)
	Optic neuritis	Hyperintensity on T_2-weighted MRI	(Boretius et al., 2006)
		Enhancement with Gd or Gf	(Boretius et al., 2006; Wuerfel et al., 2007;

		Decrease in axial diffusivity and increase in radial diffusivity with DTI	Wuerfel et al., 2010) (Sun et al., 2007)
	Atrophy	Cerebellar cortical atrophy, cerebral cortical atrophy and whole brain atrophy with T_2-weighted MRI	(MacKenzie-Graham et al., 2006; MacKenzie-Graham et al., 2009; MacKenzie-Graham et al., 2012)
	Vascular changes	Hypointensities with T_2*-weighted MRI and susceptibility weighted MRI 2D time-of-flight angiography for altered branch positions of spinal arteries	(Xu et al., 1998; Waiczies et al., 2012; Nathoo et al., 2013) (Mori et al., 2014)
	Functional changes	Neuronal dysfunction with MEMRI	(Chen et al., 2008)
	Changes in metabolites	Reduction in NAA with ^{1}H-MRS	(Brenner et al., 1993; Preece et al., 1993; Richards et al., 1995; Chen et al., 2008)
TMEV	BBB breakdown and inflammation	Hyperintensities on T_2-weighted MRI and enhancement with Gd	(Pirko et al., 2004a)
	Atrophy	Ventricular enlargement with T_2-weighted MRI	(Pirko et al., 2011)
	Black holes	Hypointensities with T_1-weighted MRI that resolve during the disease course	(Pirko et al., 2004b)
	Changes in deep grey matter	Hypointensity on T_2-weighted MRI	(Pirko et al., 2009)
	Neuronal loss	Hyperintensities on T_2-weighted MRI and reduction in NAA with ^{1}H-MRS	(Buenz et al., 2009)
	White matter changes	Hyperintensities have been seen on T_2-weighted MRI, but have not been discussed	(Pirko et al., 2004a)

		with respect to demyelination specifically Histology shows demyelination in spinal cord lesions	(Dal Canto and Lipton, 1975)
Cuprizone	White matter changes	Increase in radial diffusivity, increase in axial diffusivity and decrease in fractional anisotropy with DTI with demyelination Decrease in MTR with demyelination Increase in T_2* and decrease in grey-white matter frequency contrast with demyelination	(Song et al., 2005; Sun et al., 2006; Xie et al., 2010; Thiessen et al., 2013) (Merkler et al., 2005; Zaaraoui et al., 2008; Thiessen et al., 2013) (Lee et al., 2012a)
	Axonal damage	Reduced parallel apparent diffusion coefficient with diffusion weighted imaging Decrease in axial diffusivity with DTI	(Wu et al., 2008) (Sun et al., 2006; Xie et al., 2010; Zhang et al., 2012)
	Changes in deep grey matter	Decrease in MTR	(Fjaer et al., 2013)
Lysolecithin	BBB breakdown	Enhancement with Gd	(Ford et al., 1990)
	White matter changes	Decrease in MTR with demyelination Decrease in axial diffusivity and fractional anisotropy, and increase in radial diffusivity with DTI with demyelination	(Dousset et al., 1995; Deloire-Grassin et al., 2000; McCreary et al., 2009) (DeBoy et al., 2007)

1.6 MRI studies in EAE for assessing current MS medications

Within the realm of evaluating potential therapies for MS, MRI plays a significant role, with MRI metrics frequently being used as outcome measures for clinical trials (Li et al., 2006). If a potential agent does not show benefit on MRI in phase II, it will not be pursued in a phase III trial. It seems logical, then, to use preclinical MRI studies as a screening tool for potential agents to determine if there is enough of a benefit provided by the agent to take it into clinical trials.

Some DMTs already being utilized as treatments for MS have been tested in EAE using MRI to assess the effectiveness of these agents. Glatiramer acetate is an anti-inflammatory therapy for MS. When applied in EAE, mice treated with glatiramer acetate had reduced ventricle volume, increased MTR and reduced apparent diffusion coefficient compared to untreated EAE mice; these results corresponded to immunohistochemistry of reduced cell infiltration, demyelination and axonal changes in glatiramer acetate-treated EAE mice compared to untreated EAE mice. These alterations in MRI metrics are indicative of the anti-inflammatory and neuroprotective properties of glatiramer acetate (Aharoni et al., 2013). However, it is unknown whether the neuroprotective benefits offered by glatiramer acetate are a secondary result of being anti-inflammatory, or if there is a separate mechanism of action conferring neuroprotection. Glatiramer acetate has been shown to promote repair through various mechanisms including increased expression of growth factors and an elevation in the number of oligodendrocyte precursor cells (Keough and Yong, 2013).

Interferon-β is another immunomodulatory treatment for MS. One of the mechanisms of action of interferon-β is to reduce leukocyte trafficking into the CNS at the

level of the BBB which has been seen as reduction in Gd enhancement in MRI (Yong, 2002). The effects of interferon-β have been tested in a focal EAE model (where the injection was made in the corpus callosum) to determine if it helps prevent damage associated with re-activation of a lesion following administration of interleukin-1β (IL-1β), which is produced during peripheral infections both in the brain and systemically (Zetterstrom et al., 1998). In this study, IL-1β was administered via an adenoviral vector, as the adenoviral vector would only be taken up by the liver, leading to IL-1β expression only in the periphery. Damage due to reactivation of the lesion following administration of the adenovirus containing IL-1β was reduced when interferon-β was administered. Specifically, BBB breakdown was reduced (as shown by reduced Gd enhancement in the ipsilateral meninges), apparent diffusion coefficient hyperintensity was reduced, and regional cerebral blood volume was reduced as measured using dynamic susceptibility contrast perfusion MRI (Serres et al., 2013). These MRI alterations were in agreement with reduced inflammation and demyelination as assessed using histology (Serres et al., 2013).

Natalizumab is a humanized monoclonal antibody against very late antigen-4 (VLA-4), an integrin (α4 integrin) expressed on leukocytes. Anti-VLA-4 attenuates EAE through preventing leukocyte adhesion onto the inflamed brain endothelium by blocking the interaction between VLA-4 and VCAM-1 (Yednock et al., 1992). In EAE, USPIOs were applied to track monocyte infiltration into the brains of animals treated with monoclonal anti-rat VLA-4 antibodies. Anti-VLA-4 did not completely prevent monocyte entry into the CNS, but it reduced USPIO-based T_1 lesion volumes on MRI compared to vehicle antibody-treated animals (Deloire et al., 2004). Furthermore, MRI volume changes correlated with histological staining for macrophages/microglia (Deloire et al., 2004). Anti-

α4 integrin has also been used in guinea pigs with acute EAE between 11 and 17 days post-immunization, where it was shown to reduce Gd enhancement in T_1 and edema in T_2-weighted MRI in treated EAE animals compared with untreated EAE animals (Piraino et al., 2005).

Fingolimod (previously known as FTY720) is the first licensed oral treatment for MS which acts as a sphingosine-1 phosphate receptor modulator, leading to immunomodulatory effects (Aktas et al., 2010). The first study using fingolimod in EAE with MRI (Rausch et al., 2004) took place approximately three years before results from phase II clinical trials were published, which makes this an interesting example of a preclinical MRI study that may have guided subsequent clinical trials. There were no Gd or USPIO lesions in rats that received fingolimod during the acute phase of EAE, whereas untreated EAE rats had Gd-enhancing lesions that also accumulated USPIOs. These results correlated well with scoring for disability and with histology for macrophages (Rausch et al., 2004). Fingolimod has also been assessed in EAE using DTI where it was observed that axial diffusivity was elevated and radial diffusivity was reduced in EAE mice treated with fingolimod compared to those treated with vehicle, regardless of whether treatment was administered at disease induction or at disease onset (Wang et al., 2013). These alterations in axial diffusivity and radial diffusivity are in agreement with histological findings, which showed greater preservation of axons and myelin in fingolimod-treated EAE mice compared to vehicle-treated EAE mice; these results suggest that fingolimod has a protective effect in EAE (Wang et al., 2013). So far, results gleaned from MRI studies in EAE using established MS therapies have corroborated human clinical data.

1.7 Susceptibility-based MRI and methods and susceptibility weighted imaging (SWI)

MRI has become a mainstay in MS for diagnosis and evaluation of the effectiveness of therapeutics on MS disease processes. The MRI signal is actually a rotating vector with a magnitude (size of vector) and a phase (angle of rotation). To date, the vast majority of MRI methods have used only the magnitude data from the MRI acquisition. The magnitude image is what we are used to seeing when we look at an MRI scan; it shows the anatomy of a structure and the associated abnormalities indicative of disease, and gives a measure of the size of the signal. The other set of data that is also acquired during an MRI scan, but usually discarded, is the phase data. Until recently, phase data was not commonly used because it was difficult to process and had no perceived value. Nonetheless, phase data can provide valuable information.

Phase is influenced by echo time (TE) and magnetic susceptibility effects. Magnetic susceptibility may be defined as a quantitative measure which reflects a material's tendency to interact with and to distort an external magnetic field (Schenck, 1996), or in other words, the effects compounds in tissue can have on the magnetic field in the z direction (z-axis); these compounds are either diamagnetic or paramagnetic. Diamagnetic elements, such as calcium, have a magnetic susceptibility value less than 0, reducing the effective magnetic field, whereas paramagnetic elements like iron have a magnetic susceptibility value greater than 0, increasing the effective magnetic field (Haacke et al., 2009b). The relationship between magnetic susceptibility and its effect on the local magnetic field can be expressed using the following equation (Hopkins and Wehrli, 1997):

$$\Delta B = \chi B_0$$

where ΔB refers to the difference between the uniform magnetic field B_0 and the local magnetic field and χ refers to the magnetic susceptibility in a given voxel. Phase shifts due to such paramagnetic or diamagnetic elements can be calculated using the following equation (Haacke and Reichenbach, 2011):

$$\varphi = -\gamma \Delta B TE$$

where φ refers to the phase value, γ refers to the gyromagnetic ratio, ΔB refers to the difference between the uniform magnetic field B_0 and the local magnetic field in a given voxel, and TE refers to the echo time. Therefore, as paramagnetic elements have magnetic susceptibility values above 0, they will add to the local magnetic field, causing the phase shift to be negative ($\varphi < 0$) while diamagnetic elements will reduce the local magnetic field, leading to a positive phase shift ($\varphi > 0$) (Haacke and Reichenbach, 2011).

Phase data has become of interest. In 2004, Haacke and colleagues introduced an MRI processing method called susceptibility-weighted imaging (SWI) (Haacke et al., 2004). SWI combines the magnitude and phase data in a unique way that preserves the anatomy of the structure of interest while incorporating the phase data to highlight either diamagnetic or paramagnetic element of interest. SWI uses high resolution 3D gradient echo with full flow-compensation. The flow-compensated acquisition prevents motion artefact (such as flowing blood) from appearing in the image. SWI is based on blood-oxygen-level-dependent imaging that has been in use for years (Haacke et al., 2004), but the post-processing methods and the combination of magnitude and phase data makes it unique compared to other MRI methods.

SWI is currently used to study numerous conditions because of its ability to enhance contrast for both diamagnetic and paramagnetic elements. The most common

diamagnetic element being studied using SWI is calcium, while the most common paramagnetic element being studied is iron. That being said, SWI has been used to study other paramagnetic elements like copper in the context of a condition such as Wilson's disease (Lee et al., 2012b). This is significant because it indicates that though SWI is sensitive to iron, it is not specific to iron. Thus, there is a need to differentiate SWI signals originating from iron from those originating from other paramagnetic elements; this is an avenue that has not been strongly pursued so far. However, iron is 30 times more abundant in the human body than the other paramagnetic elements combined (Schenck, 1992) and is implicated in a number of diseases. It is the element investigated most in SWI studies, and is assumed to be the element observed in SWI studies unless a condition specific to a different paramagnetic element (e.g. copper in Wilson's disease) is being investigated. SWI is sensitive to iron found in various forms including in deoxyhemoglobin, ferritin, and hemosiderin (Chavhan et al., 2009), making it particularly useful for studying venous structures. Currently, SWI is being used for studies in multiple sclerosis (see below), stroke (Gao et al., 2008; Baik et al., 2012), Parkinson's disease (Gupta et al., 2010; Zhang et al., 2010a) and Alzheimer's disease (Schrag et al., 2010; Yates et al., 2011), amongst others.

To clarify, for the rest of this thesis, the term SWI essentially refers to the post-processing method introduced by Haacke and colleagues where phase data is filtered and a negative phase mask is multiplied into the magnitude data to create an SWI image. Other MRI methods also exist, which, like SWI, exploit and highlight magnetic susceptibility effects of various compounds in tissue, including quantitative susceptibility mapping (QSM), and phase imaging.

Another tool that can be used is the relaxivity measure R_2^* ($1/T_2^*$); R_2' ($1/T_2^* - 1/T_2$). R_2^* maps are derived from multi-echo gradient echo T_2^* data. T_2^* is examined using gradient echo imaging and is used for SWI acquisitions because of its sensitivity to magnetic field inhomogeneities caused by paramagnetic compounds, as described. The use of a multi-echo sequence enables for quantification of T_2^* values and for mapping the T_2^* values of each pixel in an image with a T_2^* map. It has been shown that iron (both heme and non-heme) and myelin increase R_2^*, and conversely that the loss of iron and myelin reduce R_2^* (Yao et al., 2012). However, when measuring phase, myelin causes a positive phase shift while iron causes a negative phase shift. For the rest of this thesis proposal, we will classify R_2^*, R_2', QSM, phase imaging and SWI under the umbrella term susceptibility-based MRI.

1.8 Potential causes of changes in susceptibility MRI in MS

There are a number of potential causes of changes in signal in susceptibility MRI in MS; these primarily relate to iron and/or myelin. Iron is paramagnetic, leading to an increase in susceptibility which appears as darkening (or hypointensity) on susceptibility MR images. However, iron is in different quantum spin states depending on what it is bound to (Schenck, 1992). In transferrin, it is 5/2, in deoxyhemoglobin it is 4/2, and in ferritin it is 3/2. Therefore, iron in transferrin and in deoxyhemoglobin is more paramagnetic than iron bound to ferritin (Schenck, 1992). Of note, the first time the magnetic properties of hemoglobin was described was in 1936 (Pauling and Coryell, 1936).

The global assessment of iron with susceptibility MRI in MS is summarized (**Table 1.4**). Changes detected in the deep grey matter structures with susceptibility MRI methods (e.g. R_2*, phase, QSM), indicative of iron accumulation, have been correlated with iron content both in normal human brains using inductively coupled plasma mass spectrometry (Langkammer et al., 2010) and X-ray fluorescence (Hopp et al., 2010), and in MS brains using histopathology (Walsh et al., 2013), and X-ray fluorescence and inductively coupled plasma mass spectrometry (Zheng et al., 2013).

In the vicinity of lesions, susceptibility MRI changes suggestive of iron deposition have been observed – this microscopic assessment of iron in lesions is also summarized (**Table 1.5**). Studies correlating susceptibility MRI with histopathology using MS brains have shown that MRI changes may be due to focal iron deposits with myelin loss, or areas with loss of both myelin and iron (Bagnato et al., 2011; Yao et al., 2012). However, imaging studies alone cannot differentiate between iron deposits originating from hemoglobin breakdown or from degrading myelin.

Although there is ample evidence of iron accumulation in MS patients, a recent study showed that there is a lack of iron accumulation, both globally and in the vicinity of lesions, in multiple EAE models and other animal models used to study MS, like cuprizone (Schuh et al., 2014). In the chronic C57BL/6 model induced by active immunization with MOG_{35-55} (the EAE model selected to be used in this thesis), iron accumulation was only seen in single macrophages within individual lesions (Schuh et al., 2014). However, this study looked later in the disease course (days 21, 27, 35 days post-immunization), not at peak disease. Furthermore, staining was only carried out for ferrous iron, not ferric iron.

Thus, more studies need to be carried out to determine conclusively that iron accumulation is not a significant phenomenon in these models, as it is in MS.

Myelin is diamagnetic, leading to a decrease in susceptibility. Conditions in which white matter is lost, particularly demyelination or hypomyelination, lead to an increase in susceptibility. A study using susceptibility-based MRI in the cuprizone model found that demyelination led to significantly increased T_2* in white matter and substantially reduced grey/white matter contrast, and thereby concluded that myelin is the main source of grey-white matter susceptibility contrast in the brain (Lee et al., 2012a). Another study used quantitative mapping of susceptibility in the shiverer mouse (which has little to no myelin in the CNS due to a lack of MBP), where it was found that susceptibility contrast was reduced by 96% between grey and white matter in shiverer mice compared to controls (Liu et al., 2011).

Another possible explanation for changes in susceptibility MRI in MS is deoxyhemoglobin. This has been explored in the realm of studying the presence of a central vein in white matter lesions in MS patients (Kau et al., 2013; Mistry et al., 2013). Other studies have used susceptibility MRI to look at the visibility of the venous vasculature in MS patients, with two studies finding that it is reduced, particularly in the periventricular white matter (Ge et al., 2009; Zivadinov et al., 2011). However, compared to the number of studies that have used susceptibility MRI for investigating iron accumulation in MS, the area of deoxyhemoglobin in MS is currently underexplored.

Table 1.4 Global assessment of iron in MS with susceptibility MRI

Adapted from (Stephenson et al., 2014)

Observation	Methods	Evidence
Iron is elevated in deep grey matter structures of MS patients and in patients with CIS	Susceptibility MRI (R_2*, phase, SWI, QSM)	Changes in MRI suggestive of iron deposition were seen in the caudate (Hammond et al., 2008; Khalil et al., 2011; Al-Radaideh et al., 2013; Walsh et al., 2014), putamen (Hammond et al., 2008; Khalil et al., 2011; Al-Radaideh et al., 2013), globus pallidus (Hammond et al., 2008; Khalil et al., 2011; Lebel et al., 2012; Al-Radaideh et al., 2013; Walsh et al., 2014), pulvinar nucleus of the thalamus (Lebel et al., 2012; Al-Radaideh et al., 2013; Walsh et al., 2014), thalamus (Walsh et al., 2014) and substantia nigra (Lebel et al., 2012; Walsh et al., 2014) in MS and CIS
Iron deposition is associated with MS disease progression; iron deposition appears lower in CIS than in RRMS and SPMS	Susceptibility MRI (R_2*, SWI)	R_2* values were significantly higher in the basal ganglia in RRMS than in CIS, suggestive of greater iron deposition in RRMS (Khalil et al., 2009) Abnormal phase changes in the subcortical deep grey matter, suggestive of iron accumulation, were greater in SPMS compared to RRMS (Zivadinov et al., 2012)
Iron accumulation shows strong correlation with disability progression	MRI (T_2-weighted, R_2*, phase), EDSS	Changes in MRI suggestive of iron deposition were associated with disability progression (assessed using EDSS) in the caudate (Neema et al., 2009), putamen (Neema et al., 2009), thalamus (Neema et al., 2009; Lebel et al., 2012), pulvinar nucleus of the thalamus (Lebel et al., 2012; Walsh et al., 2014), red nucleus (Lebel et al., 2012; Walsh et al., 2014), substantia nigra (Walsh et al., 2014) and globus pallidus (Walsh et al., 2014)
Iron accumulation correlates with grey matter atrophy	Susceptibility MRI (R_2*, SWI)	Increases in R_2* in the putamen, globus pallidus and caudate of MS patients were significantly correlated with whole grey

		matter atrophy (Khalil et al., 2009) Changes in phase in MS patients were significantly correlated with atrophy in the caudate, pulvinar nucleus of the thalamus, caudate and putamen (Zivadinov et al., 2012)
Tissue iron and/or deoxyhemoglobin or myelin, or any combination of these, are reduced in MS normal-appearing white matter (NAWM)	Susceptibility MRI (R_2')	R_2' values were reduced in the NAWM in MS compared to controls (Paling et al., 2012)

Table 1.5 Microscopic assessment of iron associated with MS lesions with susceptibility MRI

Adapted from (Stephenson et al., 2014)

Observation	Methods	Evidence
MS brains show iron staining in macrophages and microglia, around sites of inflammation and near demyelinated plaques	Susceptibility MRI (R_2*, phase), histopathology	High R_2* and low phase were seen in lesion rims which correlated with elevated ferritin and iron that was colocalized with macrophages/microglia (Bagnato et al., 2011)
Chronic MS lesions have dramatic loss of iron and myelin	Susceptibility MRI (R_2*, phase), histopathology	Reductions in R_2* corresponded with dramatic losses of iron and myelin; negative phase values corresponded to focal iron deposition with myelin loss (Hametner et al., 2013)
Iron deposition is present in CNS of animals with EAE, specifically around vessels and in areas of inflammation	EAE, MRI (SWI, T_2-weighted), histopathology	Iron deposition was seen in the brains (Forge et al., 1998; Williams et al., 2011) and lumbar spinal cords (Forge et al., 1998; Nathoo et al., 2013) of EAE animals with MRI (as areas with dark or hypointense signal) and/or histopathology; with histopathology, iron deposits were found to colocalize with macrophages/microglia (Forge et al., 1998; Williams et al., 2011) and with astrocytes (Forge et al., 1998)

1.9 Iron and the pathophysiology of MS

Iron is an essential element for proper functioning of the central nervous system, playing an integral role in myelinogenesis (Connor and Menzies, 1996) and in neurotransmitter metabolism by acting as a co-factor for enzymes involved in the process (Crichton et al., 2011). Iron is also important for proper functioning of the immune system, as the immune system gets depressed with iron deficiency (Kuvibidila et al., 1990). T-cell proliferation and the release of certain cytokines also depend on iron (Brock and Stevenson, 1987).

Although iron is a vital component of many biological processes, excessive levels of iron in tissue can be detrimental, though this is not always the case. For example, in a bacterial infection, excess iron can promote the inflammatory states of microglia and macrophages, enabling the body to fight off the infection (Williams et al., 2012). However, free (unbound) iron can also lead to increased oxidative stress by reacting with hydrogen peroxide via the Fenton reaction to produce reactive oxygen species (ROS). ROS are key players in perpetuating biological damage by inducing mitochondrial dysfunction, lipid peroxidation and oxidation of proteins (Williams et al., 2012). Iron also enhances the toxicity of pro-inflammatory cytokines such as IFN-γ and TNF-α on oligodendrocytes in a dose-dependent manner (Zhang et al., 2005).

Iron has been linked to MS for many years, both by its actions on neurons leading to neuronal toxicity and death, as well as by its presence in the vicinity of MS plaques and in the deep grey matter of the brain. Thus, iron appears to play a role both in the inflammation and neurodegeneration present in MS. In addition to increasing oxidative stress, iron promotes neuronal toxicity and death through other mechanisms: it enhances

glutamate release by neurons (McGahan et al., 2005). Application of an iron chelator was shown to protect against glutamate-mediated excitotoxicity in a model of motor neuron degeneration (Yu et al., 2009). Glutamate excitotoxicity is especially important in MS, as glutamate plays a role in oligodendrocyte cell death (Matute, 2011).

Iron has also been reported to surround MS plaques using histological methods (Craelius et al., 1982; Adams, 1988), where it is often found in the perivascular region (Adams, 1988). These iron deposits in the white matter localize to reactive microglia, macrophages, and transected axons (Craelius et al., 1982; Adams, 1988; LeVine, 1997). Interestingly, iron deposits have revealed haemorrhages in MS patients, linking venous damage with MS (Adams, 1988). Elevated levels of iron in the deep grey matter of the brains of MS patients have also been demonstrated using various MRI methods aside from those already described earlier, including T_2 relaxometry (Burgetova et al., 2010), T_2-weighted imaging (Drayer et al., 1987; Zhang et al., 2010b; Ceccarelli et al., 2011), and magnetic field correction (Ge et al., 2007).

Iron deposits have also been shown in the EAE model using histochemistry (Forge et al., 1998); these deposits localize to vessels, reactive microglia, and macrophages, though they have also been observed as granular deposits and in extravasated red blood cells (Forge et al., 1998; Pedchenko and LeVine, 1998). Administration of the iron chelator deferoxamine has been shown to suppress EAE severity and disease duration (Bowern et al., 1984; Pedchenko and LeVine, 1998), as does the iron chelator deferiprone (Mitchell et al., 2007). Furthermore, feeding mice an iron-deficient diet resulted in 0% incidence of developing EAE compared to mice fed a normal diet (71% incidence) and mice fed a diet

containing excess iron (62%) (Grant et al., 2003). Taken together, these studies indicate that the role of iron in EAE requires further investigation.

1.10 Thesis rationale and aims

With the promising work carried out using susceptibility-based MRI methods like SWI in MS patients – particularly its use for lesion detection, visualization of venous vessels and for studying iron deposition in deep grey matter structures – it would be logical to determine whether the EAE model shows similar phenotypes with SWI as is seen in MS patients. As little to no work has been done using susceptibility-based MRI methods in animal models of MS, this thesis is exploratory in nature. At the time of starting this work, no studies had been published using SWI in the EAE model. The overarching goal was to characterize SWI in the EAE model as a means to learn more about the potential of SWI in MS, as well as to gain knowledge about EAE pathophysiology to complement the MS literature. Our specific aims were as follows:

Aim 1: To determine if SWI can detect lesions in the CNS of EAE mice, and if so, what those lesions correspond to (iron deposition vs. deoxyhemoglobin vs. demyelination).

Aim 2: To develop a method that can be used to *in vivo* to differentiate between types of lesions detected with SWI.

Aim 3: To determine when SWI lesions appear during EAE and how they change over the EAE disease course.

Aim 4: To determine if SWI lesion load can be used as a marker of treatment response with an anti-inflammatory treatment.

Chapter Two: Materials and Methods

2.1 Animals

2.1.1 Mice

Female C57BL/6 mice (either 6-8 weeks old or 8-10 weeks old, depending on the experiment) were acquired from Charles River (Montreal, Canada).

2.1.2 Induction of EAE and scoring for motor disability

EAE was induced with methods previously described and used in the Yong lab (Agrawal et al., 2011). For EAE induction, 50 μg of myelin oligodendrocyte glycoprotein (MOG_{35-55}) was emulsified in complete Freund's adjuvant (CFA) containing 10 mg/mL of heat inactivated *Mycobacterium tuberculosis*. The emulsion was injected subcutaneously into the right and left hind flanks of mice. Following this, mice were administered 300 ng of pertussis toxin (PTX) via intraperitoneal (i.p.) injection on day 0 and day 2 following immunization with MOG. Starting from day 7 post-MOG immunization, mice were weighed and scored daily for motor function to gauge their level of disability using a 15-point grading scale which has been used by the Yong lab previously; in this method, each limb and the tail were scored separately (Weaver et al., 2005). On the grading scale, the tail received a maximum score of two when completely paralyzed or a score of one when paretic. Each limb received a maximum score of up to three if fully paralyzed, a score of two if there was paresis, or a score of one if there was weakness or altered gait. A mouse that is fully paralyzed received a score of 14, and a score of 15 represented death. EAE mice were classified to be at peak disease between days 15-20 after immunization, and were classified to have long-term disease day 30 onwards after immunization.

2.1.3 Control mice

Control mice were either naive or were immunized with CFA and PTX (hereby referred to as CFA/PTX controls). Control mice were imaged at similar time points as EAE mice.

2.2 Histology

2.2.1 Animal perfusion and tissue preparation for histology

Animals were anaesthetized using an overdose of i.p. administration of ketamine/xylazine in PBS (1:2). Mice were bled by aortic puncture while the heart was still pumping (Goncalves DaSilva and Yong, 2009) using 10 mL of 1xPBS followed by 10 mL of 10% formalin. The lumbar spinal cord and cerebellum were stored in 10% formalin until they were embedded in paraffin. Lumbar spinal cords were sliced into 10μm axial sections and cerebella were sliced into 8μm axial sections where adjacent sections were placed on separate glass slides for 8 slides to make a series of 8 slides with 3-4 sections on each slide. This enabled for comparing adjacent sections with different stains.

2.2.2 Hematoxylin & eosin staining for general histopathology and inflammation

For hematoxylin & eosin staining, sections were deparaffinized through an ethanol series ending in distilled water. Sections were incubated in Harris Hematoxylin solution for eight minutes, then washed in tap water 2-3 times. Sections were dipped in 1% acid alcohol for 6-10 seconds, washed in tap water for one minute, dipped in ammonia water for 6-10 seconds then washed in tap water again for one minute. Sections were dipped 6-10 times in

70% alcohol, then 95% alcohol. Sections were dipped 2-3 times in alcoholic eosin, drained then passed through 100% alcohol and xylene. Sections were mounted with Acrytol.

2.3 MRI acquisitions

2.3.1 MRI console and coil

For all MRI acquisitions, a 9.4T Bruker Avance II console was used with a 20 mm diameter curved surface coil (**Figure 2.1**).

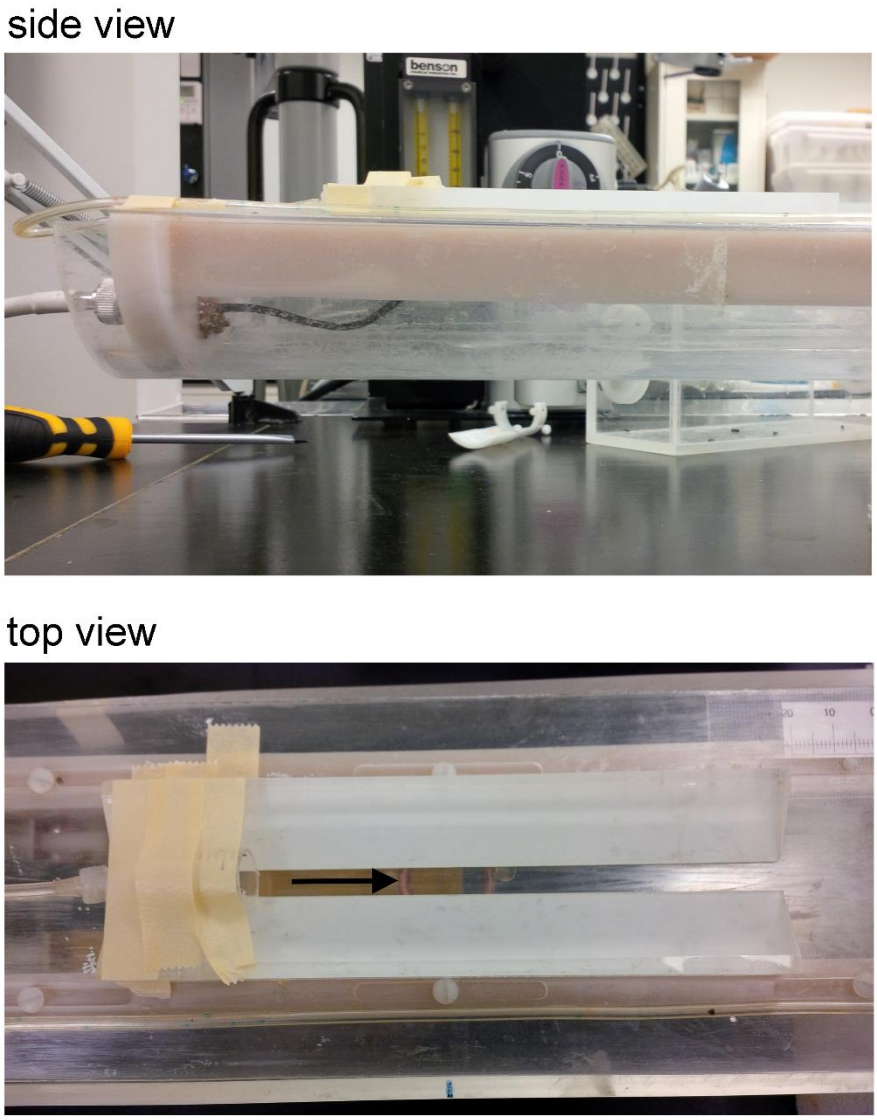

Figure 2.1 Surface coil and apparatus used for all MRI acquisitions. Images show the apparatus from a side view and from a top view. The surface coil itself is circular and is pointed out with the black arrow.

2.3.2 Selection of CNS regions for MRI

The lumbar spinal cord and cerebellum were studied as lesions are more prevalent in these areas in rodents with EAE (Tonra, 2002; Schellenberg et al., 2007).

2.3.3 Scout acquisitions of lumbar spinal cord and cerebellum

Scout images were obtained in three planes for the lumbar spinal cord and cerebellum to provide localization of the area of interest. A 2D fast low angle shot (FLASH) sequence was used for all scouts.

For the lumbar spinal cord, scouts were obtained in three orientations (axial, sagittal, coronal) using the following parameters: matrix=256 x 256, TE=4ms, TR=100ms, flip angle=30°, averages=3, slice thickness=1000μm, acquisition time=1 min, 17 sec. Additional parameters for axial scouts included the following: FOV=2cm x 2cm, voxel size=78μm x 78μm, slices=5 (**Figure 2.2**). Additional parameters for sagittal scouts included the following: FOV=2.5cm x 1.5cm, voxel size=98μm x 59μm, slices=3 (**Figure 2.3**). Additional parameters for coronal scouts included: FOV=2.5cm x 1.5cm, voxel size=98μm x 59μm, slices=3 (**Figure 2.2**).

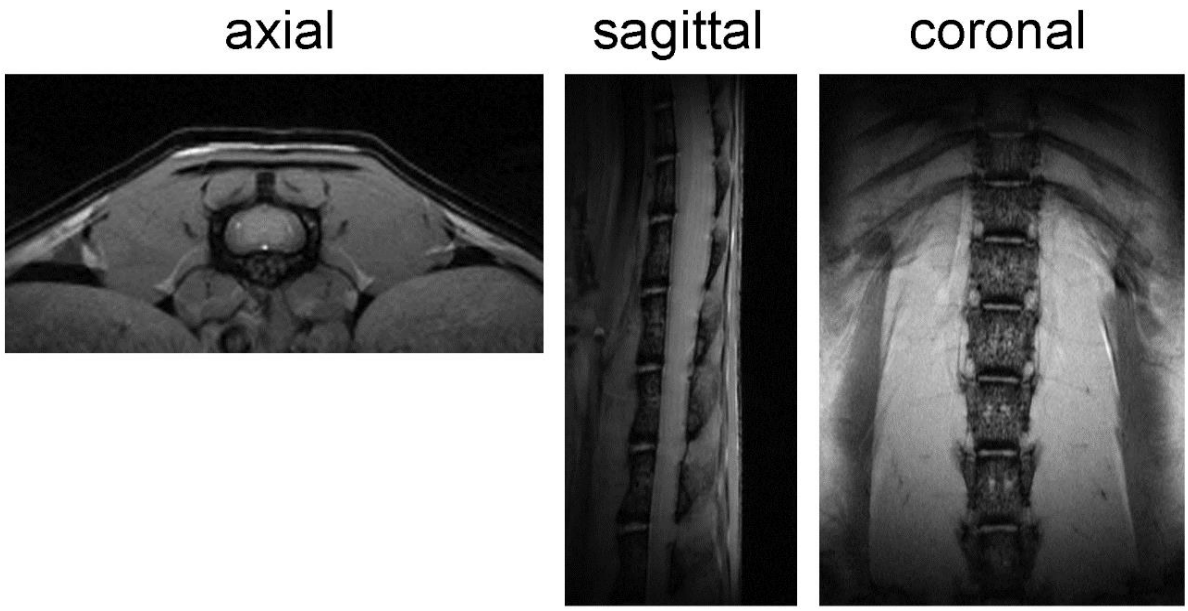

Figure 2.2 Lumbar spinal cord scouts in the axial, sagittal and coronal orientations acquired using a 2D FLASH sequence.

For the cerebellum, scouts were acquired using the same parameters as those for the lumbar spinal cord. Images of axial scouts (**Figure 2.3**), sagittal scouts (**Figure 2.4**) and coronal scouts (**Figure 2.3**) are shown.

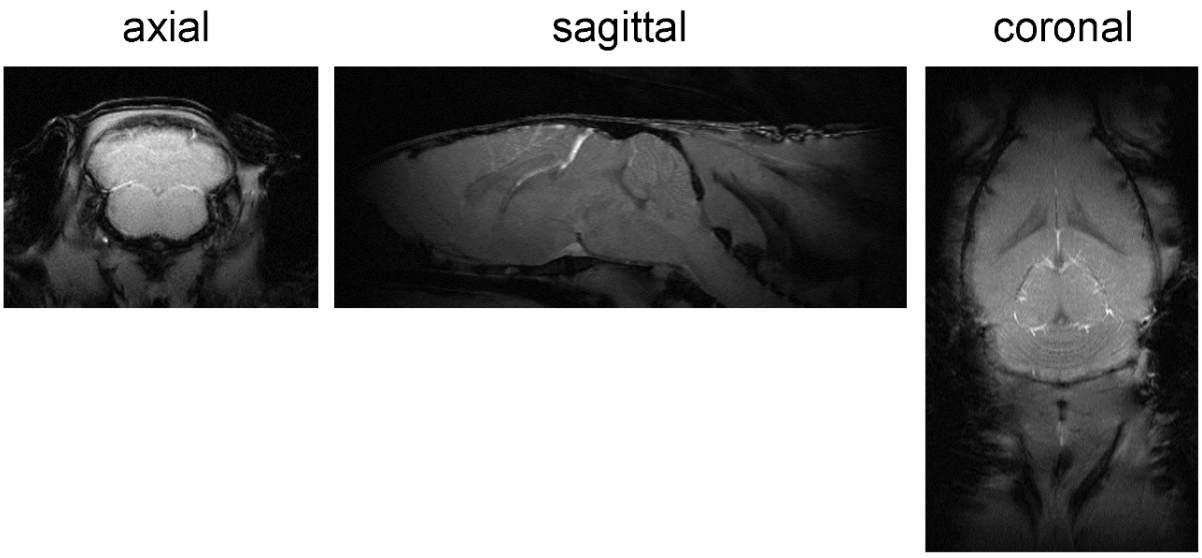

Figure 2.3 Cerebellum scouts in the axial, sagittal and coronal orientations acquired using a 2D FLASH sequence.

2.3.4 In vivo MRI acquisition for SWI of lumbar spinal cord and cerebellum

A 3D gradient echo sequence with flow compensation (GEFC) was used (**Figure 2.4**). Imaging parameters for the lumbar spinal cord and cerebellum were as follows: matrix=192 x 128 x 32 (zero-filled to 256 x 128 x 32), FOV=0.92cm x 1.28cm x 1.28cm, TE=4ms, TR=50ms, flip angle=15°, averages=17, acquired voxel size=48μm x 100μm x 400μm (displayed voxel size=36μm x 100μm x 400μm), acquisition time=58 min, 2 sec. For the lumbar spinal cord, imaging was conducted halfway through T13 down to the early part of L5 of the spinal cord, covering the majority of the lumbar spinal cord. For imaging, mice were initially anaesthetized using 2.5-3% isoflurane along with 30% O_2/70% N_2 and were kept anaesthetized throughout imaging using 1.7-2.2% isoflurane via a nose cone. Images of both the lumbar spinal cord and cerebellum were acquired in the axial orientation.

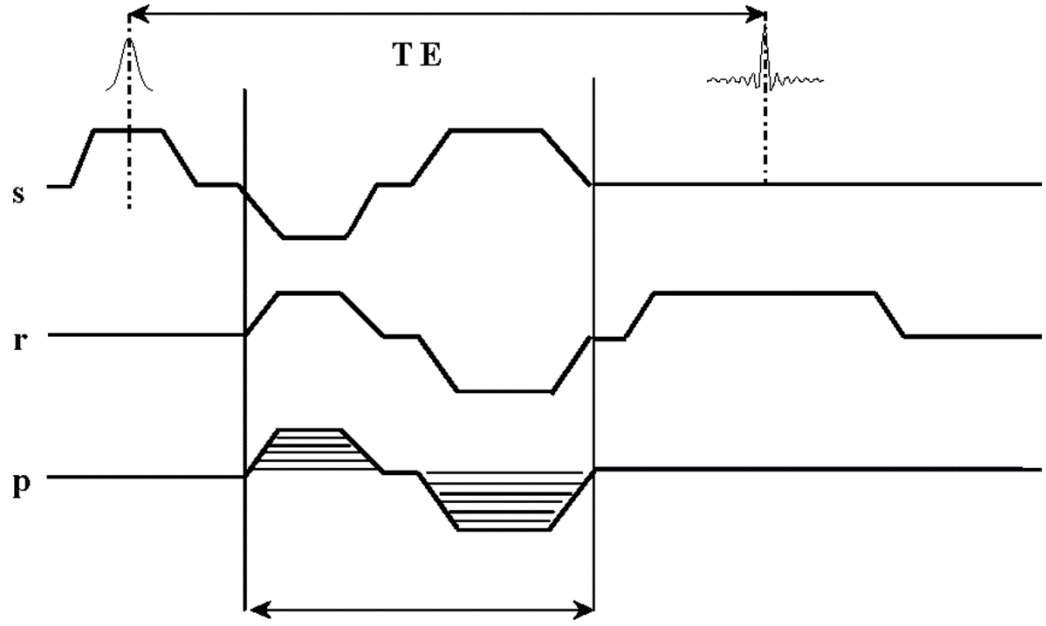

Figure 2.4 GEFC pulse sequence diagram obtained from the Bruker manual. On the diagram, s denotes slice selection, r denotes frequency encoding, p denotes phase encoding and TE denotes echo time. The vertical lines contain the two gradient pulses needed for flow compensation.

2.3.5 Pre- and post-perfusion MRI acquisitions

This protocol has been described previously (Nathoo et al., 2013). MRI acquisitions pre-perfusion (*in vivo*) followed the same protocol as described above until the point when imaging was completed. Upon completion of *in vivo* MRI, animals were anaesthetized using ketamine/xylazine in phosphate buffered saline (PBS) (1:2). Mice were perfused and sacrificed using 10 mL of 1x PBS followed by 10 mL of 10% formalin as described in section 2.2.1. The chest cavity was cleaned, covered with gauze and taped using surgical tape. The mouse was returned to the MRI console with the same 20 mm surface coil that had been used for *in vivo* MRI. The MRI acquisition carried out post-perfusion was identical to the acquisition carried out *in vivo* (as described above). Following post-perfusion MRI, the mouse's brain and spinal cord were removed and processed as described in section 2.4.1.

2.4 MRI data processing and analysis

2.4.1 Raw MRI data processing to create SWI images

Signal Processing in NMR (SPIN) software (MRI Institute; Detroit, MI) was used to process raw magnitude and phase MR images. SWI images were created using methods described previously (Haacke et al., 2004). Phase images were processed using a 32 x 32 Hanning filter, removing low frequency components and creating filtered phase images. Filtered phase data were used to create a negative phase mask which was multiplied into the original magnitude data four times to create SWI images. The images used to create SWI images and the images output by SWI processing are shown (**Figure 2.5**). The negative phase mask is usually multiplied into magnitude data three to five times to

provide good contrast to noise ratio (CNR) (Haacke et al., 2004). For the purposes of our work using SWI in mice, we also tested different numbers of phase multiplications, settling with four multiplications as providing sufficient phase information while not appearing too noisy **(Figure 2.6**). We assessed the effects of various numbers of phase multiplications visually only.

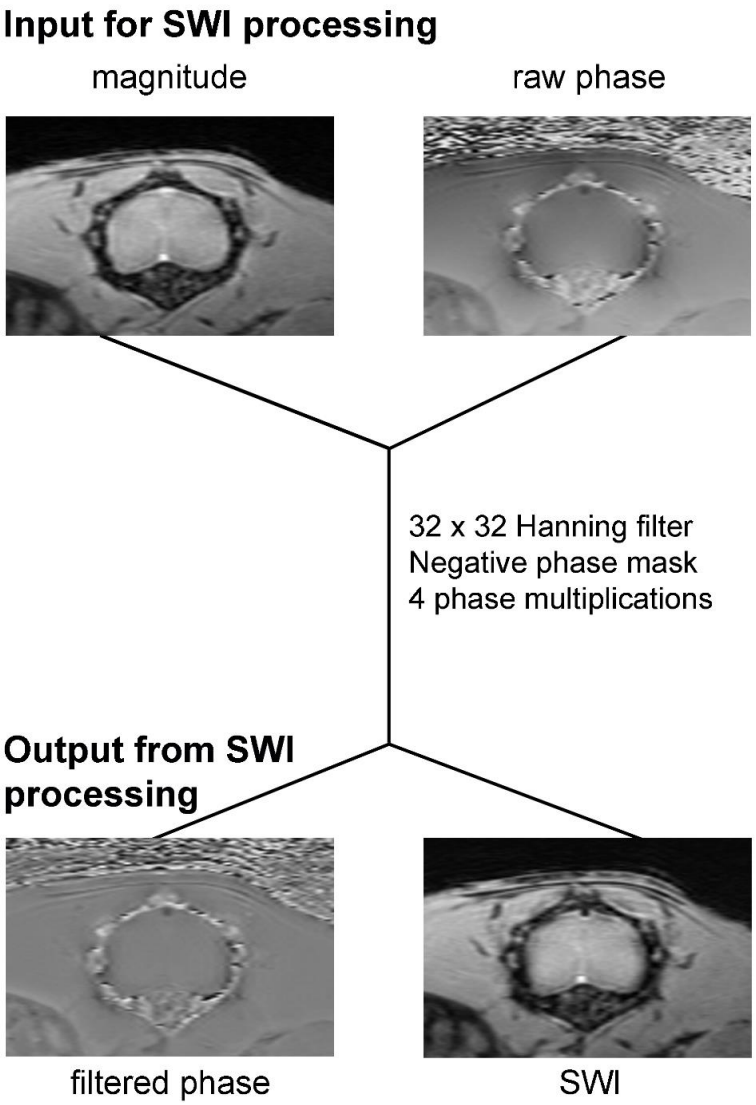

Figure 2.5 Images input for SWI processing (magnitude, raw phase) and images output upon carrying out SWI processing (filtered phase, SWI). Phase data was filtered using a 32x32 Hanning filter, a negative phase mask was created which was multiplied into the magnitude data four times to create SWI images.

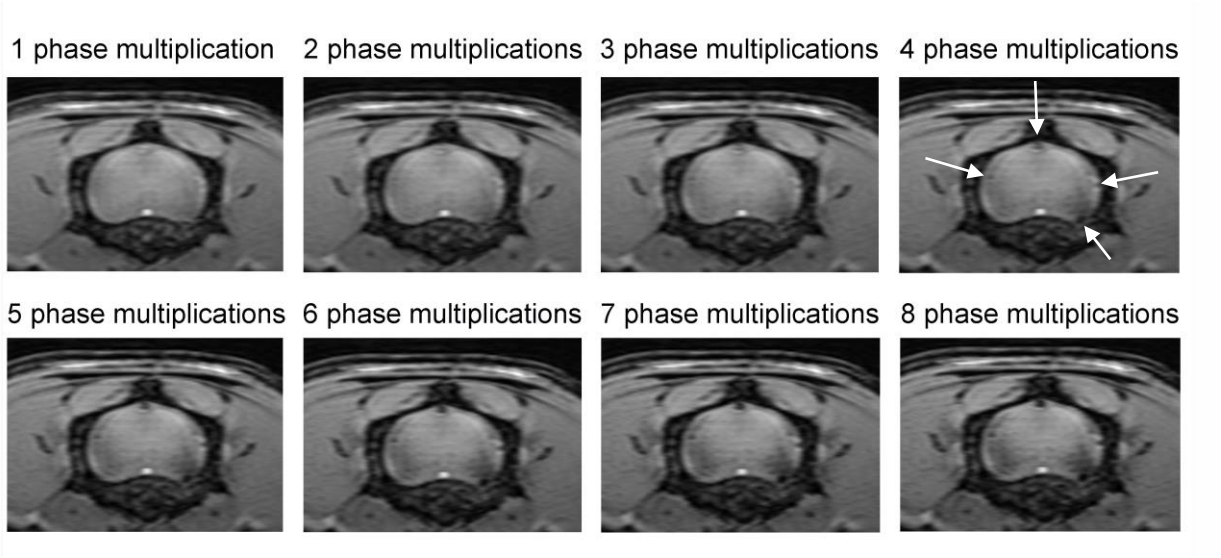

Figure 2.6 SWI MRIs of mouse lumbar spinal cord processed using different numbers of phase multiplications. Hypointensities are visible with four and higher phase multiplications with SWI (white arrows). However, images obtained with seven or eight phase multiplications appear quite noisy. A value of four phase multiplications was selected, enabling for visualization of hypointensities while images did not appear too noisy.

2.4.2 Counting of SWI hypointensities

Two researchers performed blinded hypointensity counting using SWI images for the lumbar spinal cord and cerebellum. For the lumbar spinal cord, every fifth slice was selected for each animal with a total of five slices being counted for each animal. The first 9 slices were excluded from counting as there was typically aliasing present in these images. For the cerebellum, two consecutive slices that clearly showed white matter tracts were selected from each animal's image set for counting. To compare counting of hypointensities between pre- and post-perfusion, different inspired oxygen levels or between time points, MRI slices were aligned using visual boundaries, such as the change in the butterfly shape of the lumbar spinal cord.

2.5 Other methods

Only methods used for multiple aims are described in this chapter. Other methods used which are specific to individual aims will be described in their respective chapters (Chapters 3-6).

Chapter Three: Susceptibility weighted imaging detects lesions in the central nervous system of mice with experimental autoimmune encephalomyelitis

3.1 Introduction

SWI and phase imaging show hypointense lesions in the brains of MS patients that are not detected using conventional MRI methods (Eissa et al., 2009; Haacke et al., 2009a). The sources of such focal hypointensities may be due to iron deposits, myelin loss, normal iron in oligodendrocytes or the combination of myelin loss and iron accumulation (Bagnato et al., 2011; Yao et al., 2012). However, these studies did not characterize the contribution that deoxyhemoglobin had in their results which is important because deoxyhemoglobin would also appear hypointense in susceptibility MRI (Haacke et al., 2005; Bagnato et al., 2011).

Such an elevation in deoxyhemoglobin could be due to hypoxia, which has been shown to be present in MS and in EAE through various means. Virtual hypoxia has been argued to be present in MS, where there is an impairment in the capacity of mitochondria to utilize oxygen (Trapp and Stys, 2009). An increase in hypoxia-inducible factor 1 alpha (HIF-1α, a marker of hypoxia) has been shown to be present in MS (Aboul-Enein et al., 2003; Stadelmann et al., 2005). There may also be relative reductions in the oxygen levels in blood vessels. Positron emission tomography (PET) studies have shown a decrease in the cerebral metabolic rate of oxygen, both in the grey and white matter of MS patients (Brooks et al., 1984; Sun et al., 1998). A reduction in metabolic rate could result in a decrease in hemoglobin saturation and an increase in deoxyhemoglobin levels (Ogawa et al., 1993; Dunn et al., 2009), resulting in reduced venous oxygenation or venous hypoxia.

Our aim was to determine if SWI lesions exist in the EAE model, and if so, to determine what the sources of such lesions were. In particular, we wanted to differentiate those caused by deoxyhemoglobin in the blood from those due to parenchymal iron deposition and demyelination.

3.2 Specific methods

3.2.1 Luxol fast blue staining for myelin

Luxol fast blue staining was carried out using methods previously described and used in the Yong lab (Larsen et al., 2003). Briefly, sections were deparrafinized and then incubated in Luxol fast blue solution for three hours at 60°C. Sections were rinsed in 95% alcohol followed by distilled water. Sections were destained with 0.05% lithium carbonate, differentiated in 70% alcohol and rinsed with distilled water. Sections were they dehydrated, cleared in xylene, and mounted with Acrytol.

3.2.2 Perls' staining for non-heme iron

Perls' staining was carried out as described previously (Nathoo et al., 2013). Sections were deparaffinized and hydrated in a diluted ethanol series ending in distilled water. Sections were incubated in equal parts of 20% aqueous hydrochloric acid and 10% potassium ferrocyanide for 25 minutes, washed in distilled water three times and then counterstained with nuclear fast red solution for 3.5 minutes. Sections were rinsed in distilled water, dehydrated through 95% and 100% alcohol, cleared twice in xylene and coverslipped using Permount.

3.2.3 DAB-enhanced Perls' staining for non-heme iron

DAB-enhanced Perls' staining was carried out using methods described previously (Dragatsis et al., 1998; Huang et al., 2005; Nathoo et al., 2013). Sections were deparaffinized and hydrated to distilled water, then incubated in equal parts of 1% potassium ferrocyanide and 0.12N hydrochloric acid for 30 minutes. Sections were kept in 0.3% hydrogen peroxide (H_2O_2) in methanol for 20 minutes to quench any endogenous peroxide activity. After rinsing in PBS, sections were incubated with 3,3-diaminobenzidine (DAB)/H_2O_2 (Sigma FAST-DAB tablets) for six minutes. Sections were then rinsed in distilled water, dehydrated, cleared in xylene, and mounted with Acrytol.

3.2.4 Fluorescent staining of blood vessels

Fluorescent imaging of blood vessels was conducted using methods described previously (Dunn et al., 2004). Briefly, 1 mL of fluorescein isothiocyanate (FITC) conjugated to dextran was injected into the tail vein of rodents anaesthetized with isoflurane. After 5 minutes, their spinal cords were removed and fixed in a solution of 4% paraformaldehyde and 0.2% glutaraldehyde. The lumbar spinal cord was sliced into 50µm axial sections and imaged using fluorescence microscopy.

3.2.5 Statistical analysis

To compare the number of SWI hypointensities in the lumbar spinal cord in controls, peak EAE and long-term EAE mice, a one-way analysis of variance (ANOVA) was used with Tukey's test post-hoc to enable for multiple comparisons. The same analysis was carried out for the cerebellum. To compare the number of hypointensities seen before

and after perfusion, a paired *t*-test was used. In instances where assumptions for normality or equal variance were violated, the non-parametric equivalent of the parametric test was used. For all statistical tests used, $p \leq 0.05$ was considered significant.

3.3 Results

3.3.1 Assessment of motor disability

Scores for motor disability were obtained for all mice on the day of imaging. Naïve mice (n=4) and CFA/PTX control mice all had scores of 0 (n=4). Peak EAE mice (n=12) had scores ranging from 6-11 and an average score of 9.2 ± 0.5 (mean ± SEM) and long-term EAE mice (n=5) had scores ranging from 6-10 (8.3 ± 0.7) (**Figure 3.1**).

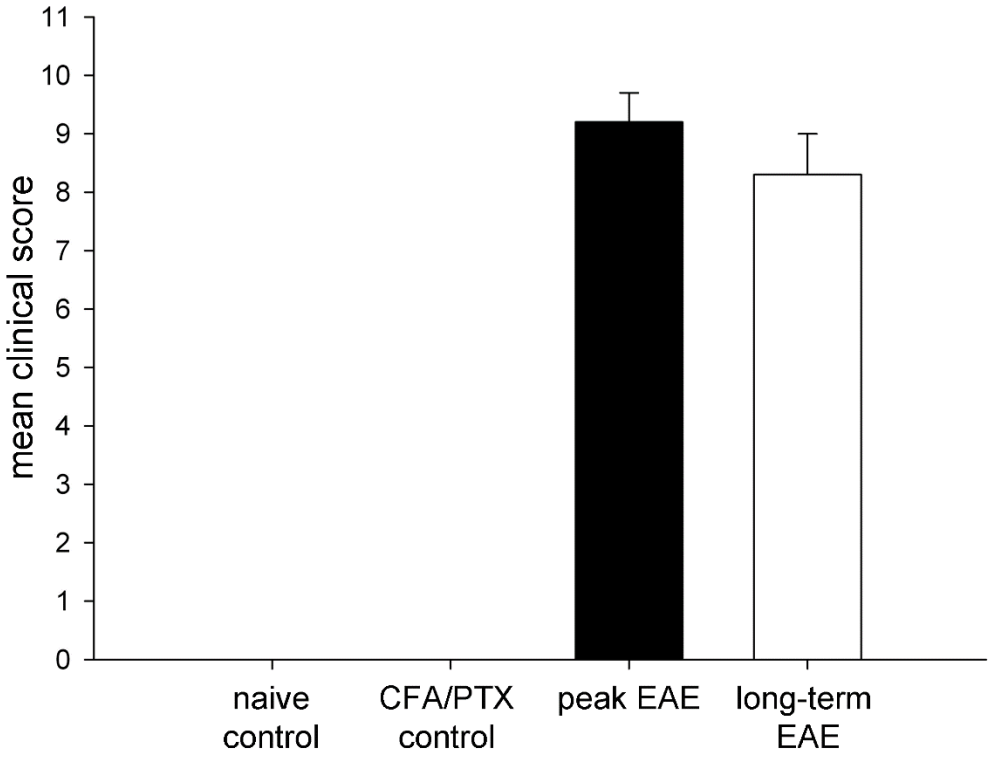
mean clinical score
11
10
9
8
7
6
5
4
3
2
1
0
naive control
CFA/PTX control
peak EAE
long-term EAE

Figure 3.1 Average scores for motor disability for naïve controls, CFA/PTX controls, peak EAE and long-term EAE mice obtained on the day of imaging. Naïve (*n*=4) and CFA/PTX controls (*n*=4) had scores of 0 while peak EAE mice (*n*=12) had scores of 9.2 ± 0.5 (mean ± SEM) and long-term EAE mice (*n*=5) had scores of 8.3 ± 0.7.

3.3.2 SWI detects hypointensities (lesions) in the lumbar spinal cord of EAE mice

The magnitude image (showing structure) and the phase image (highly sensitive to paramagnetic compounds), are combined to create the SWI image. Examples of magnitude, raw phase, SWI, and filtered phase images of the lumbar spinal cord of a naïve control, a CFA/PTX control and a long-term EAE mouse are shown (**Figure 3.2**). Hypointensities (or dark spots, or lesions) were observed in SWI images, but not in magnitude images alone (**Figure 3.2**). These hypointensities correspond to paramagnetic compounds in SWI. Many hypointensities seen with SWI in EAE mice were present at the grey/white matter boundary of the spinal cord as well as where pial vessels are present (**Figure 3.3a**) (Nathoo et al., 2013). These regions coincide with the location of draining veins in the lumbar spinal cord as visualized with FTIC dextran staining in rodent spinal cord (**Figure 3.3b**)

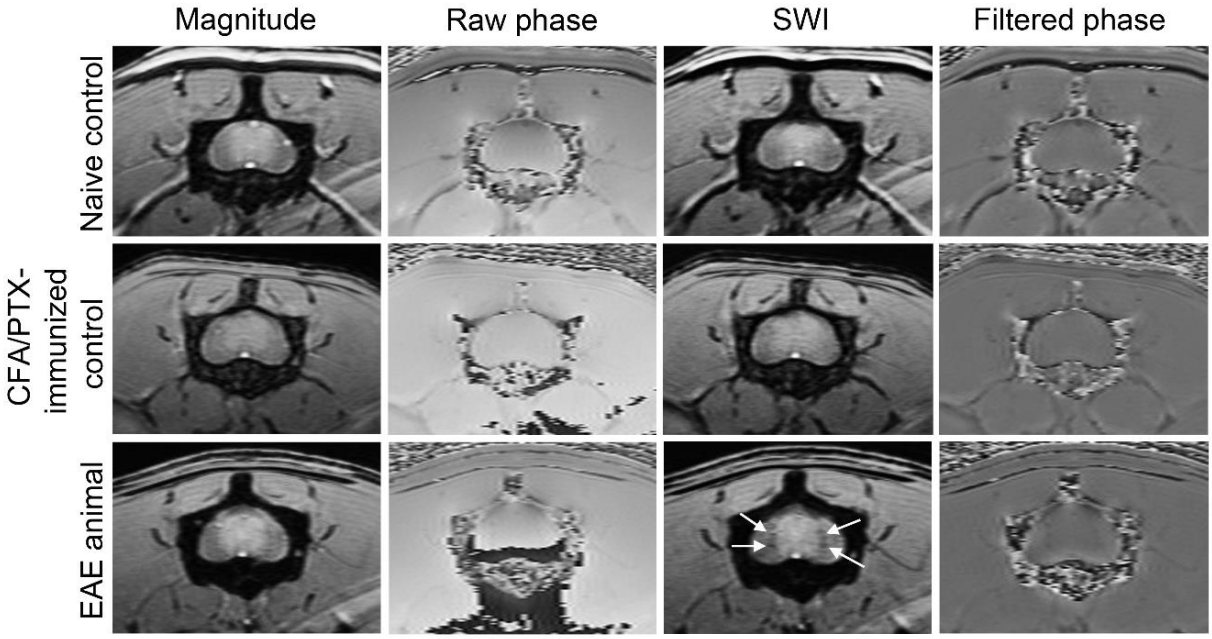

Figure 3.2 Representative *in vivo* magnitude, raw phase, SWI and filtered phase images of the lumbar spinal cord of a naïve control, CFA/PTX control and an EAE mouse at chronic disease (6 months post-immunization) with motor disability. Focal hypointensities are seen in the EAE mouse spinal cord in the SWI image (white arrows) that are not seen in the magnitude image.

Adapted from (Nathoo et al., 2013)

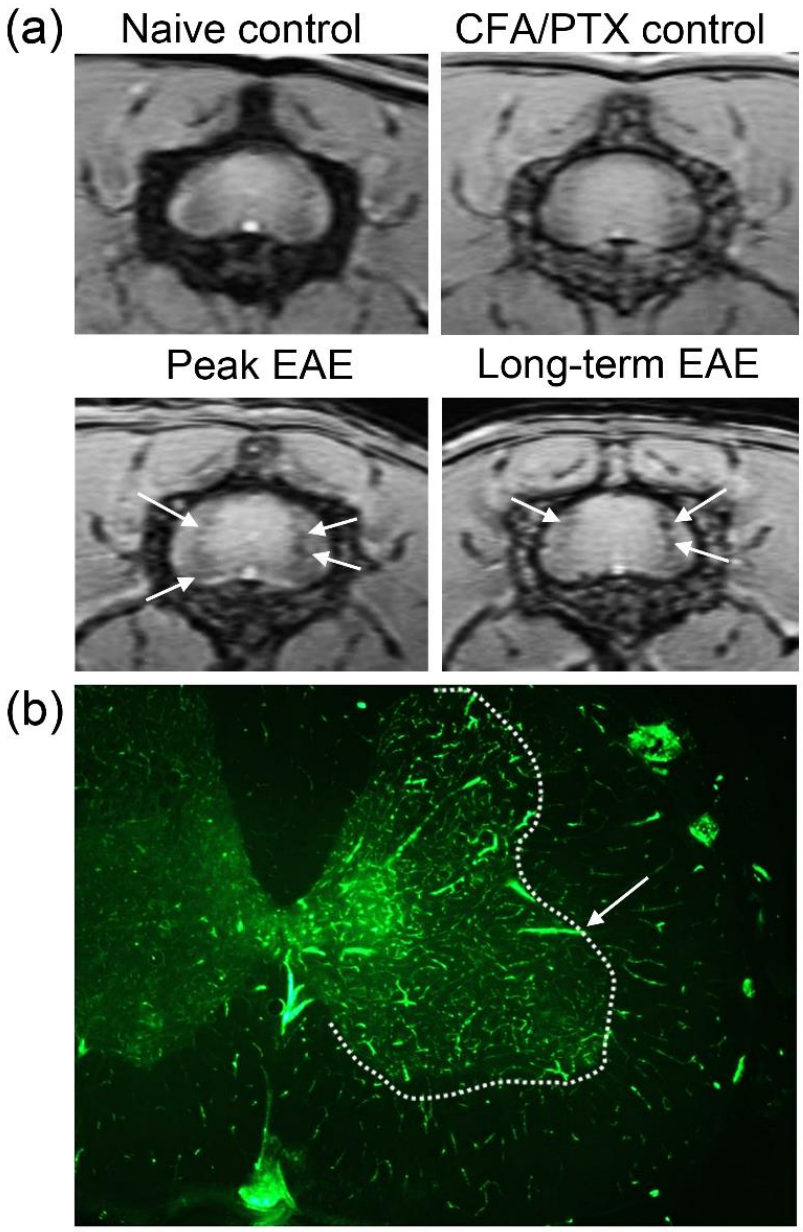
(a)
Naive control
CFA/PTX control
Peak EAE
Long-term EAE
(b)

Figure 3.3 SWI hypointensities concentrate at the grey/white matter boundary and in the pia mater of the lumbar spinal cord in EAE mice. (a) Representative SWI MRIs of a naïve control, CFA/PTX control, peak EAE mouse and chronic EAE mouse. Focal hypointensities are visible in the peak EAE and chronic EAE mice (white arrows). **(b)** Representative FTIC-dextran staining of blood vessels in rodent spinal cord. Vessels appear to extend from the grey matter to the white matter (white arrow). Numerous vessels also appear in the pia mater. The location of focal hypointensities detected with SWI appears to coincide with vessels seen with FITC, indicating that these regions are vascular. This suggests that SWI hypointensities are due to intravascular deoxyhemoglobin.

Adapted from (Nathoo et al., 2013)

3.3.3 SWI detects hypointensities (lesions) in the cerebellum of EAE mice

Example magnitude, filtered phase and SWI images of the cerebellum of a naïve control, a CFA/PTX control, a peak EAE mouse and a long-term EAE mouse are shown (**Figure 3.4**). In the cerebellum of both peak EAE and long-term EAE mice, hypointensities were observed in white matter tracts with SWI (**Figure 3.4**), which is where inflammatory perivascular cuffs have been reported in EAE (Gareau et al., 2002) and in MS (Tanaka et al., 1975). A perivascular cuff is an inflamed post-capillary venule in which mononuclear cells have accumulated around endothelial cells, prior to entering CNS parenchyma (Agrawal et al., 2013).

Hypointensities observed with SWI in cerebellar white matter tracts were associated with demyelination and inflammation in such perivascular cuffs (**Figure 3.5**). Some of these SWI MRI-visible hypointensities that were associated with perivascular cuffs also corresponded to iron deposition, but others did not (**Figure 3.5**) (Nathoo et al., 2013).

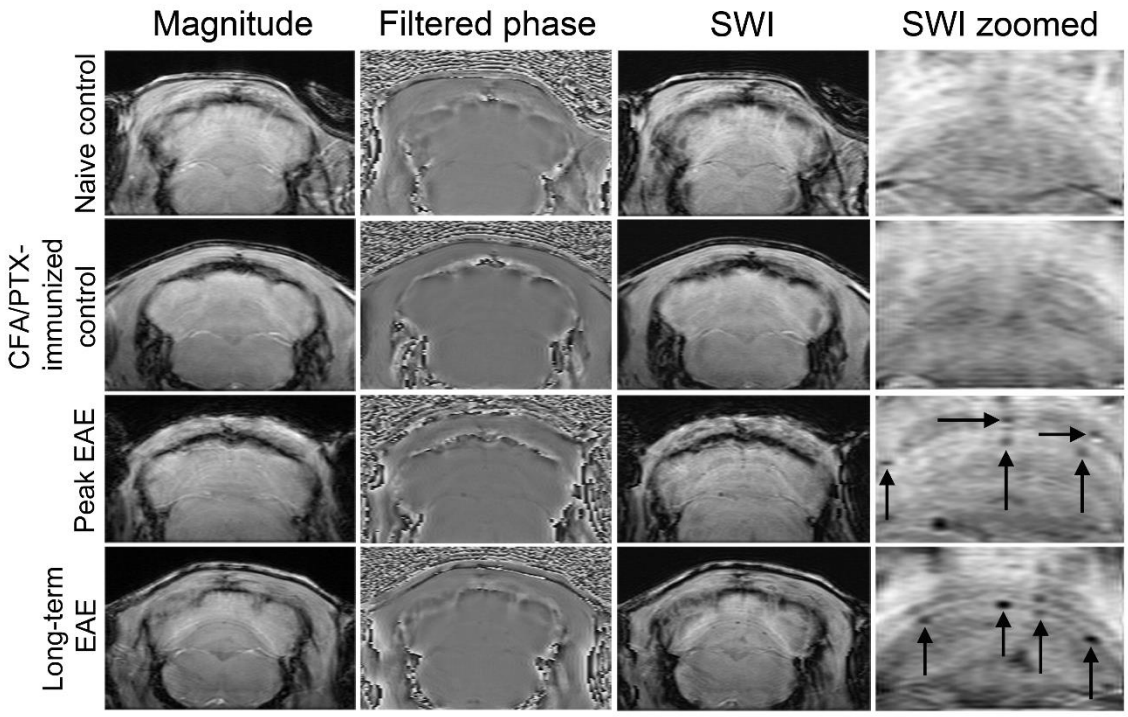

Figure 3.4 Representative *in vivo* magnitude, filtered phase and SWI images of the cerebellum of a naïve control, CFA/PTX-immunized control, peak EAE mouse and long-term EAE mouse with motor disability. Focal hypointensities are seen the white matter of the cerebella of EAE mice with SWI (black arrows).

Adapted from (Nathoo et al., 2013)

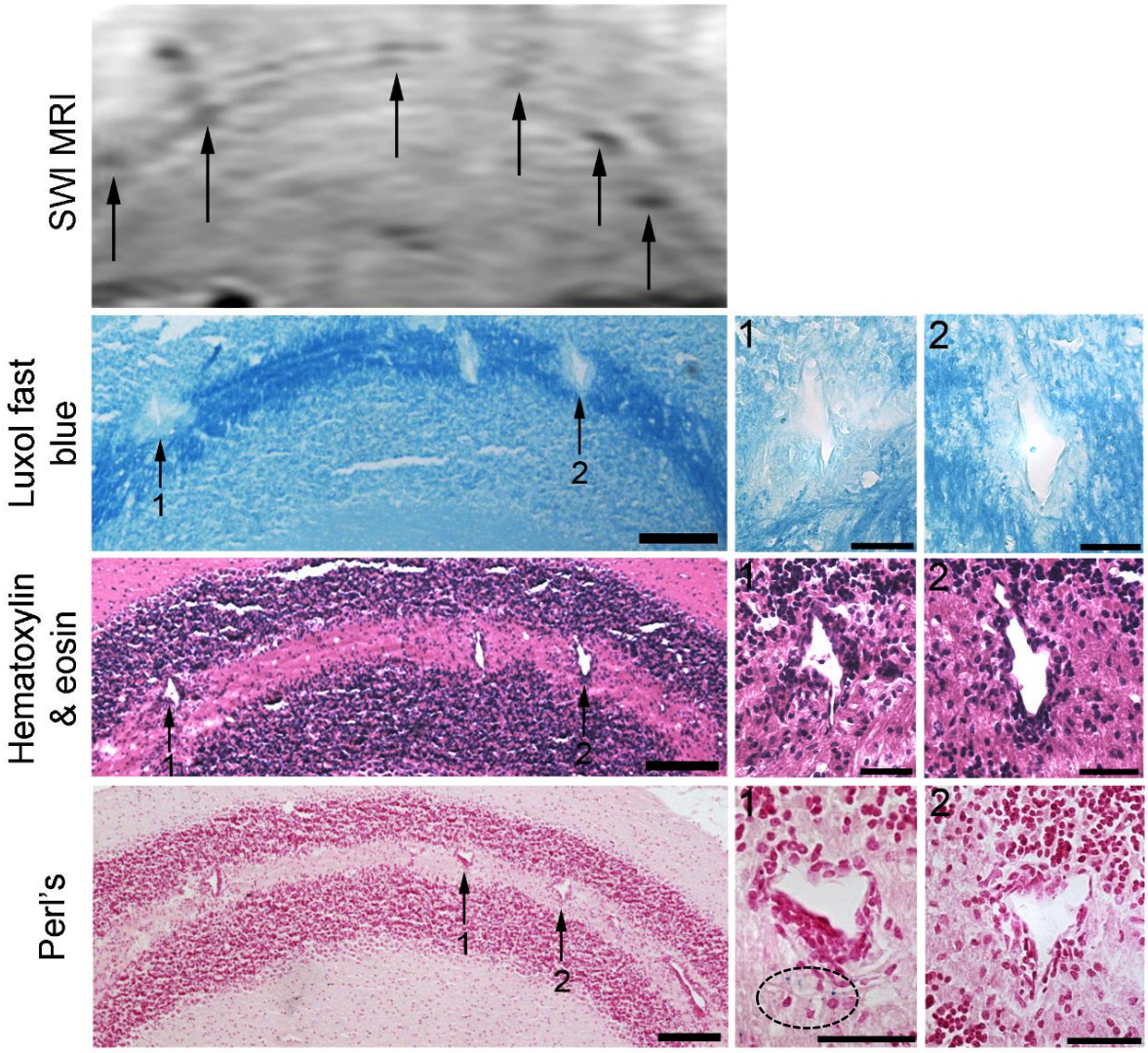
SWI MRI
Luxol fast blue
Hematoxylin & eosin
Perl's
1
2

Figure 3.5 Some SWI hypointensities in the cerebellar white matter tracts corresponded with areas histologically-confirmed to have demyelination, inflammation and iron deposition. Luxol fast blue staining, hematoxylin & eosin staining and Perl's staining were carried out using histological sections corresponding to the MRI slice for a peak EAE mouse which is shown in the top row (hypointensities are pointed out with black arrows). Demyelination was seen as a loss of Luxol fast blue (black arrows). These regions contained inflammatory perivascular cuffs as visualized with hematoxylin & eosin staining (black arrows). Perl's staining showed that some of these perivascular cuffs were associated with iron deposition as shown by the blue granules (numbered arrow 1, black dotted circle), while others were not (numbered arrow 2).

Scale bars for all three rows: 200μm (left images), 50μm (middle and right images).

Adapted from (Nathoo et al., 2013)

3.3.4 EAE mice have significantly more SWI hypointensities than control mice

Upon observing that hypointensities may also be seen in control mice, counting of hypointensities seen in SWI images was undertaken by two blinded researchers. First, the number of hypointensities was compared between naive controls and CFA/PTX-controls, where it was observed that there was no significant difference between the two types of controls in the lumbar spinal cord (p=0.343, independent t-test) nor in the cerebellum (p=0.445, independent t-test). Thus, for future statistics, data was combined from the two types of controls into one group to compare with peak EAE and long-term EAE mice.

For the number of hypointensities seen in the lumbar spinal cord, a significant difference was found between the three groups (combined controls, peak EAE, long-term EAE) (p=0.005, one-way ANOVA) (**Figure 3.6a**). Long-term EAE mice had significantly more hypointensities (22.7 ± 2.6; mean ± SEM) than control mice (11.1 ± 1.8) (p=0.005), but not significantly more than peak EAE mice (16.5 ± 1.7) (p=0.117).

For the number of hypointensities seen in the cerebellum, a significant difference was found between the three groups (combined controls, peak EAE, long-term EAE) (p=0.006, one-way ANOVA) (**Figure 3.6b**). Peak EAE mice had significantly more hypointensities (12.5 ± 1.5) than control mice (3.9 ± 1.5) (p=0.006), but not significantly more than long-term EAE mice (12.0 ± 3.3) (p=0.984). Long-term EAE mice had significantly more hypointensities than control mice (p=0.041) (Nathoo et al., 2013).

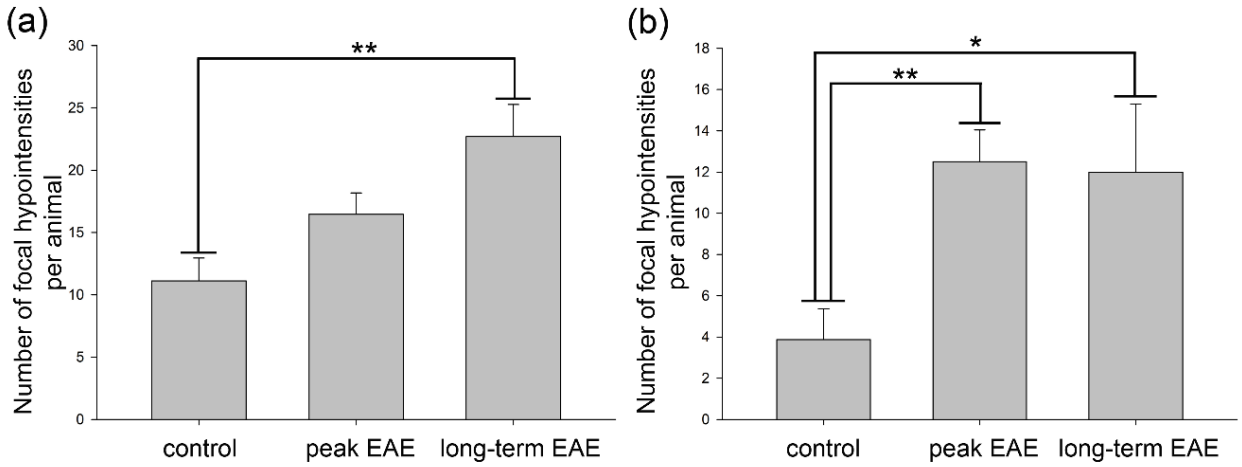

Figure 3.6 More focal hypointensities were observed with SWI in EAE mice as compared to controls. (a) Average number of focal hypointensities per mouse in the lumbar spinal cord of control (*n*=8), peak EAE (*n*=11) and long-term EAE mice (*n*=5). Long-term EAE mice had significantly more focal hypointensities per animal than controls. Every fifth slice was used for hypointensity counting, where a total of five slices were counted for each animal. **(b)** Average number of focal hypointensities per animal in the cerebellum of control (*n*=8), peak EAE (*n*=12) and long-term EAE mice (*n*=5). Both peak EAE and long-term EAE mice had significantly more focal hypointensities than control mice. Two consecutive slices were used for each mouse for hypointensity counting. Slices selected were those where the white matter tracts were clearly visible.

**p*<0.05 and ***p*<0.01 by one-way ANOVA with Tukey's test post-hoc.

Adapted from (Nathoo et al., 2013)

3.3.5 Many SWI hypointensities are likely due to intravascular deoxyhemoglobin

To test whether hypointensities seen with SWI were related to intravascular deoxyhemoglobin (deoxyhemoglobin in the blood), a subset of mice were imaged, perfused (to remove blood), then immediately re-imaged (4 controls, 9 EAE mice). In the lumbar spinal cord (**Figure 3.7a**) and cerebellum (**Figure 3.7b**), many hypointensities seen *in vivo* (before perfusion) disappeared after perfusion. That hypointensities disappeared when only blood was removed suggests that these hypointensities were due to deoxyhemoglobin in the blood.

To further investigate the contribution of deoxyhemoglobin to hypointensities seen with SWI, the number of hypointensities seen with SWI before and after perfusion was compared for EAE mice. The number of SWI hypointensities that remained after perfusion was significantly lower than the number present before perfusion in the lumbar spinal cord (p=0.004, paired t-test) and cerebellum (p=0.049, paired t-test) of EAE mice (**Figure 3.8a**). In the spinal cord, 60.1% of the hypointensities seen before perfusion remained after perfusion, while in the cerebellum, 46.4% of the hypointensities remained after perfusion. In addition, the number of hypointensities that disappeared after perfusion in the lumbar spinal cord of EAE mice was significantly greater (8.2 ± 1.3; mean ± SEM) than the number that disappeared in control mice (2.5 ± 0.8) (p=0.031, independent t-test) (**Figure 3.8b**). That EAE mice had more hypointensities disappear after perfusion is suggestive of hypoxia, as hypointensities which disappear are likely due to intravascular deoxyhemoglobin. However, such an elevation in the number of hypointensities which disappear after perfusion was not seen when comparing the cerebellum of EAE and control mice (p=0.921, Mann-Whitney U test) (data not shown).

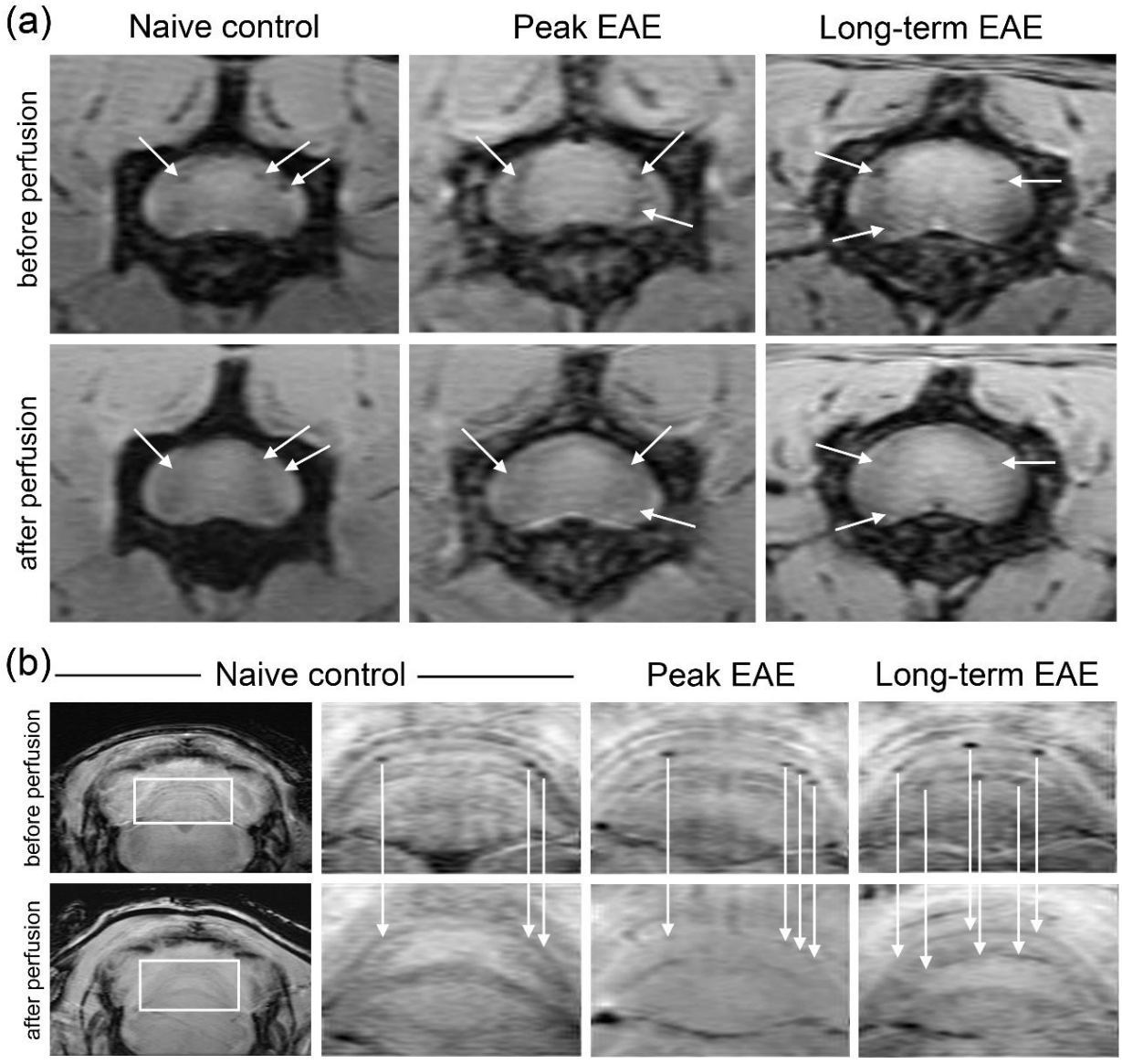
(a)
Naive control
Peak EAE
Long-term EAE
before perfusion
after perfusion
(b)
Naive control
Peak EAE
Long-term EAE
before perfusion
after perfusion

Figure 3.7 Many SWI hypointensities that were present *in vivo* before perfusion disappeared after perfusion. (a) Representative SWI MRIs of the lumbar spinal cord of naïve control, peak EAE and long-term EAE mice, where many focal hypointensities that were observed at the grey/white matter boundary of the spinal cord and in the pia mater before perfusion were not seen after perfusion (white arrows). **(b)** Representative SWI MRIs of the cerebella of naïve control, peak EAE and long-term EAE mice, where focal hypointensities seen in white matter tracts (outlined by white boxes in left column and zoomed in on for the three columns to the right) before perfusion were absent after perfusion (white arrows point from focal hypointensities visible before perfusion to the same areas after perfusion, where focal hypointensities are no longer seen). That many focal hypointensities are not seen after perfusion supports that these SWI hypointensities were associated with iron present in deoxyhemoglobin in the vasculature, and were not due to parenchymal iron deposition.

Adapted from (Nathoo et al., 2013)

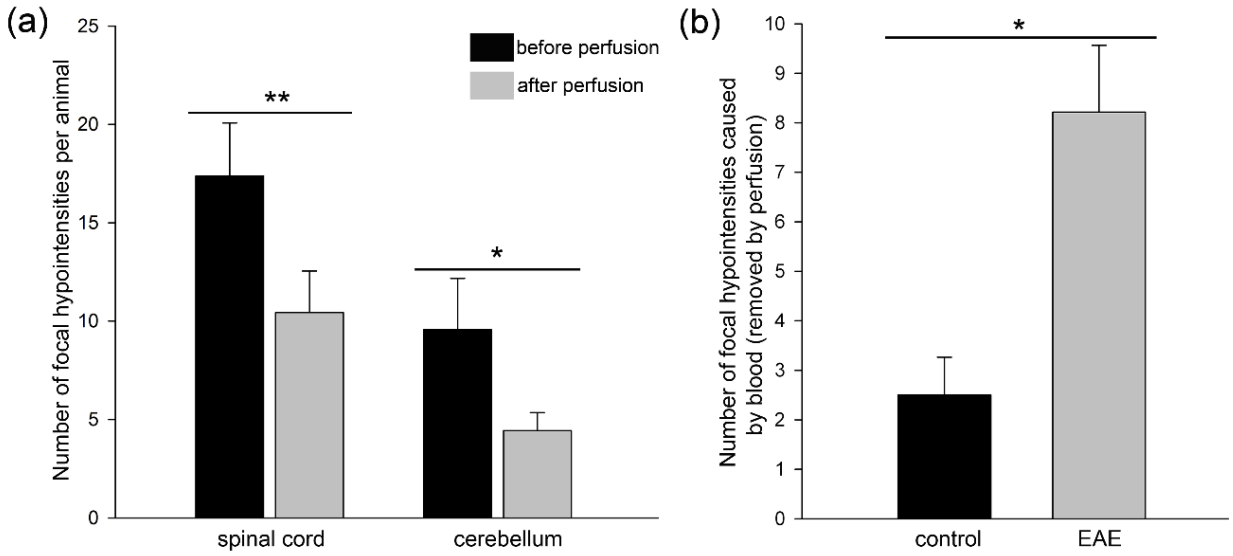

Figure 3.8 The number of focal hypointensities seen before perfusion is much higher than the number seen after perfusion in EAE mice, and EAE mice have many more hypointensities disappear than control mice. (a) Average number of focal hypointensities per animal in EAE mice (*n*=8) before and after perfusion for the lumbar spinal cord and cerebellum. There were significantly more focal hypointensities before perfusion, in both the lumbar spinal cord and cerebellum, than were present after perfusion. Hypointensities were counted the same way as described in Figure 3.6. **(b)** In the lumbar spinal cord, the number of focal hypointensities removed by perfusion was significantly greater in EAE mice (*n*=7) than in controls (*n*=3).

*p<0.05 and **p<0.01 by paired *t*-test in (a), *p<0.05 by independent *t*-test in (b)

Part (a) was adapted from (Nathoo et al., 2013)

3.3.6 SWI hypointensities (lesions) that remain after perfusion in the ventral white matter of the lumbar spinal cord are areas with iron deposition, demyelination and inflammation

There were hypointensities observed in the white matter of the lumbar spinal cord of EAE mice with SWI which did not disappear after perfusion. However, only three such lesions were observed, all of which were located in the ventral white matter (**Figure 3.9a**). Although not an exhaustive study, all of these lesions in the ventral white matter seen with SWI corresponded to an area with iron deposition, demyelination and inflammation (**Figure 3.9b**). Hypointensities seen with SWI at the grey/white matter boundary or in the pia mater of the lumbar spinal cord that disappeared after perfusion were not observed to correspond with areas of iron deposition, demyelination or inflammation (**Figure 3.9c**).

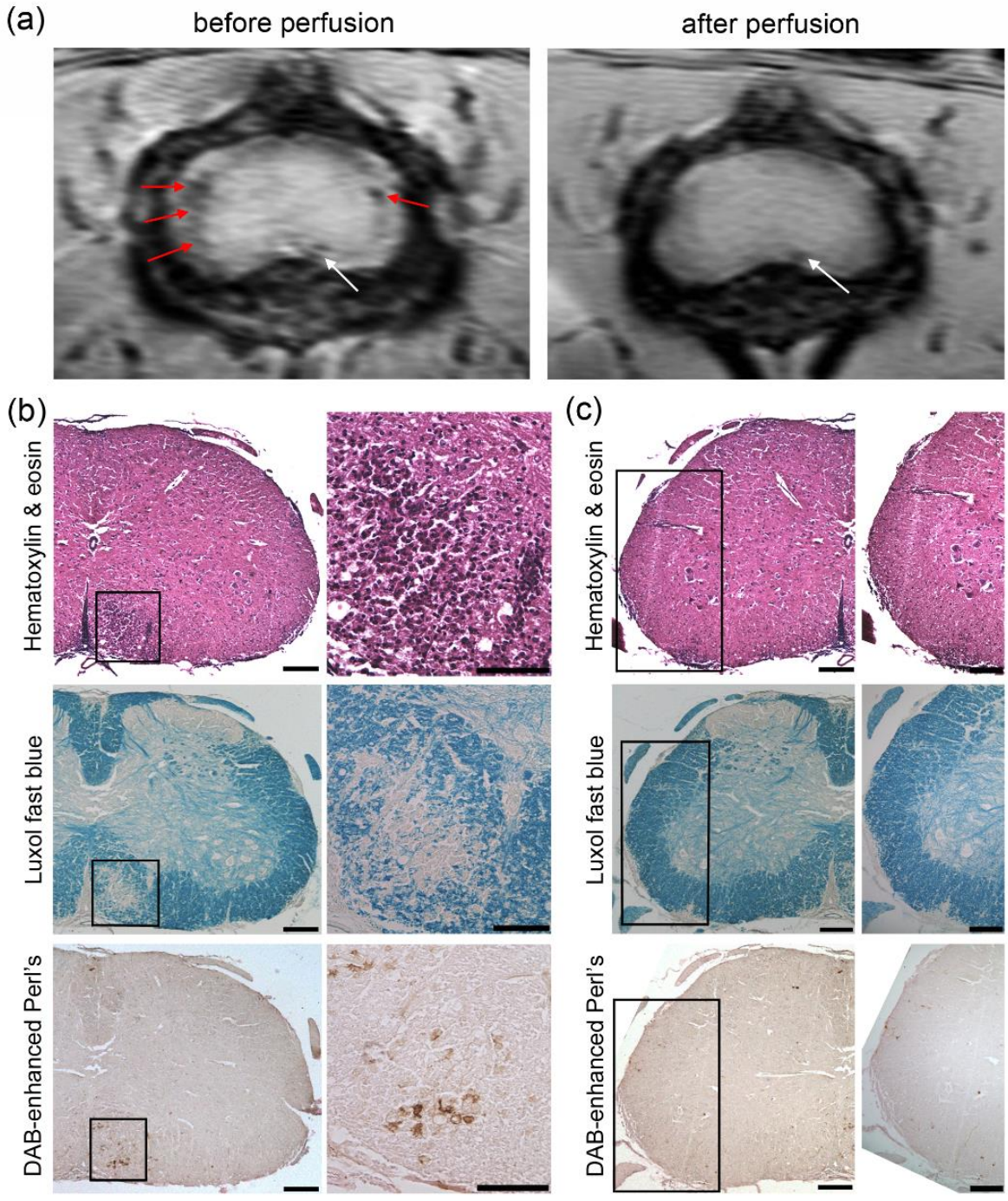
(a)
before perfusion
after perfusion
(b)
(c)
Hematoxylin & eosin
Luxol fast blue
DAB-enhanced Perl's
Hematoxylin & eosin
Luxol fast blue
DAB-enhanced Perl's

Figure 3.9 SWI hypointensities at the grey/white matter boundary and in the pia matter of the lumbar spinal cord disappeared after perfusion, but ventral white matter lesions remained and corresponded to areas of inflammation, demyelination and iron deposition. (a) SWI MRIs before and after perfusion for an EAE mouse at peak disease with motor disability, 19 days post-MOG immunization. Many hypointensities observed before perfusion disappeared after perfusion (red arrows). One hypointensity that was present in the ventral white matter before perfusion remained after perfusion (white arrows in both MR images). **(b)** Histology of the white matter lesion that was shown in the SWI MRI slices in (a), which remained after perfusion, corresponded to an area of inflammation, demyelination and iron deposition. **(c)** Histology for the grey/white matter boundary hypointensities that were observed to disappear after perfusion in the SWI MRI slices seen in (a). The areas containing grey/white matter boundary and pia mater hypointensities did not correspond to areas of inflammation, demyelination or iron deposition, which supports the observation that grey/white matter boundary and pia mater hypointensities are related to deoxyhemoglobin in blood.

Scale bars in (b): 200μm (left images), 100μm (right images); scale bars in (c): 200μm (left images), 150μm (right images)

Adapted from (Nathoo et al., 2013)

3.4 Discussion

In this study, SWI was shown to detect lesions (hypointensities) in the lumbar spinal cord and cerebellum of EAE mice; these lesions are similar in appearance (appearing as focal hypointensities) to those reported in patients with MS. Although the term lesion is often used to denote an abnormality, these localized hypointense spots can also occur in control mice. Indeed, such hypointense spots were observed in control mice and correspond to veins. For the sake of simplicity, the terms lesions or focal hypointensities are both used, interchangeably. On average, there were more SWI lesions in the different EAE groups (peak EAE, long-term EAE), indicating that there was a relationship of lesions with EAE pathology.

SWI lesions appeared to be regionally specific. In the spinal cord, some SWI lesions were in the ventral white matter while most were located at the grey/white matter boundary or in the pia mater. SWI lesions in the ventral white matter of the lumbar spinal cord correlated not only to iron deposition, but also to demyelination and inflammation. At this time, the relative contributions of each factor to the final signal loss in SWI cannot be differentiated.

Of note, a statistically significant difference was not observed for the number of focal hypointensities in control mice compared to peak EAE mice for the lumbar spinal cord. Grouping peak EAE and long-term EAE data resulted in a significant elevation in the EAE group. Thus, it is likely that peak EAE mice had an abnormal variance which reduced the chance of finding significance when comparing controls to peak EAE.

In the cerebellum, SWI lesions were located largely in the white matter tracts. SWI lesions were observed in areas where perivascular cuffs are present, and we found that they

corresponded histologically with inflammation, demyelination and iron deposition in a manner similar to that observed in the ventral white matter of the lumbar spinal cord. A previous histological study of EAE mice showed that there is iron deposition in the cerebrum and hindbrain, as well as in the cervical, thoracic and lumbar spinal cord (Forge et al., 1998).

In MS patients, SWI has shown lesions that are suggested to relate to iron deposition (Haacke et al., 2009a). Using phase MRI and iron histochemistry, it was shown that periventricular white matter lesions with low phase, suggestive of iron, contain a central vessel surrounded by perivascular iron deposition (Bagnato et al., 2011). The distribution in patients definitely includes the deep grey matter, but detailed examination of regional variation has not been made to date, especially one comparing the spinal cord with the brain.

Although lesions similar to those seen in MS patients were observed in EAE mice, it is clear that not all of these lesions in EAE mice are associated with iron. By subjecting mice to MRI before and after perfusion, it was evident that many focal hypointensities observable with SWI *in vivo* were no longer present after removal of blood from the vasculature. Thus, our data suggests that a number of SWI lesions in EAE mice were related to deoxyhemoglobin, not to parenchymal iron deposits, as human MS studies with SWI have implied to date (Haacke et al., 2009a; Zivadinov et al., 2010).

It should be noted that some SWI lesions remained after perfusion, even in control animals. It is possible that some or all post-perfusion SWI lesions are caused by a vascular bed that is not totally cleared of hemoglobin. As a result, the number of SWI lesions that relate to changes in the parenchyma may be overestimated.

There are multiple possibilities as to why there would be elevated deoxyhemoglobin content in the EAE model. Deoxyhemoglobin increases in areas of hypoxia or ischemia – this has recently become of interest, and was covered by a review article which emphasized the existence of ischemia in MS patients (D'Haeseleer et al., 2011). There is evidence that MS patients have increased risk of ischemic stroke (Allen et al., 2008; Christiansen et al., 2010), possibly resulting from endothelial dysfunction as a consequence of inflammation (D'Haeseleer et al., 2011). Cerebral blood flow has been reported to be reduced in MS patients, in both grey and white matter, leading to global hypoperfusion in the brain (Lycke et al., 1993; Adhya et al., 2006). Reduced blood flow with a constant metabolic rate would result in an increased oxygen extraction fraction and an increase in deoxyhemoglobin. Deoxyhemoglobin content also increases when the lumen diameter of a blood vessel increases, as blood volume will increase even if the hemoglobin oxygen saturation remains constant. Vascular SWI lesions may be caused by enlargement of inflamed veins, as described previously by others (Ahrens et al., 1998). Greater investigation of the venous anatomy is required, because if the vessels are not enlarged, then this supports the hypothesis that the hemoglobin oxygen saturation in these vessels would be lower than in controls – this would be an indication of localized hypoxia.

Overall, this study shows that many of the SWI lesions are likely due to deoxyhemoglobin in the vasculature, while a smaller number of demyelinating lesions were also observed which corresponded to iron deposition. Thus, there is a need for more imaging studies to differentiate between lesions caused by iron deposition and an increase in deoxyhemoglobin. Distinguishing between these is of great importance in the context of MS, as all of these factors are implicated in the pathophysiology of the disease. In

particular, the role of hypoxia in the generation of SWI lesions, the progression of MS pathophysiology, and as a biomarker of disease progression and treatment will all need further attention.

Chapter Four: Hyperoxygenation combined with susceptibility weighted imaging identifies deoxyhemoglobin-based vascular hypointensities

4.1 Introduction

Previously in the EAE model, we showed that SWI detects hypointensities in the cerebellum and lumbar spinal cord of EAE mice, many of which were due to deoxyhemoglobin in the vasculature (Nathoo et al., 2013). However, in that study, MRI was conducted in animals that had been sacrificed (perfused) to identify deoxyhemoglobin-based hypointensities. This would not be practical in a clinical setting. Therefore, in order to identify hypointensities due to intravascular deoxyhemoglobin, an *in vivo* method is required. Such a method could be applied in MS patients to discern the contribution of deoxyhemoglobin to signal changes seen with susceptibility MRI, as deoxyhemoglobin is a significant contributor to hypointense signals seen with susceptibility MRI (Haacke et al., 2005; Bagnato et al., 2011).

In this study, we proposed a method where deoxyhemoglobin-based hypointensities could be identified *in vivo*. The visibility of the venous vasculature is highly dependent on the partial pressure of oxygen. Therefore, increasing the partial pressure of oxygen, or increasing the inspired oxygen concentration, reduces the visibility of the venous vasculature. The aim of this study was to identify deoxyhemoglobin-based hypointensities by imaging naïve control and EAE mice using two different oxygen concentrations: a standard inspired oxygen concentration (30%) and a high inspired oxygen concentration (100%). Our hypothesis was that vascular hypointensities visible with 30% O_2 would disappear upon administration of 100% O_2. If our hypothesis was correct, we would have a

means to identify hypointensities due to intravascular deoxyhemoglobin in vivo, providing an avenue for investigating the proportion of hypointensities due to deoxyhemoglobin in the context of EAE and MS.

4.2 Specific methods

4.2.1 MRI acquisition for different concentrations of oxygen in inhalation gas

Naïve control mice (*n*=9), peak EAE mice (*n*=9) and long-term EAE mice (*n*=5) were imaged first using a mixture of 30% O_2/70% N_2, as described in section 2.2.4. At the end of this MRI acquisition, the gas was switched to 100% O_2. To ensure the gas line contained only 100% O_2, ~10 minutes were allotted before starting the second MRI acquisition. The same MRI acquisition was carried out with 100% O_2 as was performed using the 30% O_2/70% N_2 mixture before. As the mouse did not have to be moved during imaging, the images acquired using the two different percent oxygen concentrations could be directly compared. Isoflurane was adjusted as needed to ensure the mouse's respiration rate remained consistent. The mouse's temperature was monitored throughout imaging.

4.2.2 Counting of hypointensities and classification of changes in appearance of hypointensities with 100% O_2

Blinded data was used by two researchers for counting of hypointensities using 30% O_2 and 100% O_2 data obtained from naive mice (*n*=9) and EAE mice at peak disease that had a behavior score above 6 during the disease course with an additional animal being excluded as it did not respond to oxygen at all (*n*=6). Every fifth slice was used for counting for each spinal cord, and a total of five slices were counted per animal.

Hypointensities were counted using the 30% O_2 data first, and then 100% O_2 data was used to classify those hypointensities seen with 30% O_2. Hypointensities that had been observed with 30% O_2 data were classified using 100% O_2 data into one of the following categories: 1) hypointensity seen with 30% O_2 disappeared with 100% O_2; 2) hypointensity appeared less dark (hypointense) with 100% O_2 than was seen with 30% O_2, but did not disappear completely; or 3) hypointensity seen with 30% O_2 became hyperintense (bright) with 100% O_2. Hypointensities observed that did not fall into one of these categories were assumed to remain the same in appearance with 30% O_2 and 100% O_2.

4.2.3 Statistical analysis

A two factor univariate repeated measures ANOVA was carried out to compare if there was a significant difference in the number of hypointensities using the animal type (control vs. peak EAE) and oxygen level (30% O_2 vs. 100% O_2) as the two factors, with the animal type as the repeated factor. If these factors were found to significantly affect the number of hypointensities, then individual comparisons were carried out as described below.

The number of hypointensities seen with 30% O_2 between naive and peak EAE mice was compared using an independent *t*-test. To compare the number of hypointensities seen with 30% O_2 with the number that remained unchanged upon administration of 100% O_2, paired *t*-tests were used for naive control and peak EAE data. To compare the different response types observed with 100% O_2 between control and EAE mice, independent *t*-tests were used for each response type. In instances where assumptions for normality or equal

variance were violated, the non-parametric equivalent of the parametric test was used. For all statistical tests used, $p \leq 0.05$ was considered significant.

4.2.4 SWI hypointensity counting is correlated between two blinded researchers for both 30% O_2 and 100% O_2 data

To determine how consistent hypointensity counting was between the two blinded researchers, Pearson's correlation was used for the number of hypointensities seen with 30% O_2 and the number of hypointensities that changed with 100% O_2. There was a strong positive correlation for hypointensity counting between the two researchers for data acquired with 30% O_2 ($r=0.773$, $p<0.001$, Pearson's correlation), indicating that counting was consistent between individuals. For the number of hypointensities that changed with 100% O_2, there was a moderate positive correlation between the two researchers ($r=0.574$, $p=0.025$, Pearson's correlation). Taken together, these data indicate that counting between researchers was consistent.

4.3 Results

4.3.1 Assessment of motor disability

All mice were scored on the day of imaging except for one long-term EAE mouse. Naïve control mice ($n=9$) all had scores of 0. Peak EAE mice ($n=9$) had scores ranging from 1-10 and an average score of 5.1 ± 1.1 (mean ± SEM). Long-term EAE mice ($n=4$) had scores ranging from 4-9 and an average score of 6.5 ± 1.2 (**Figure 4.1**).

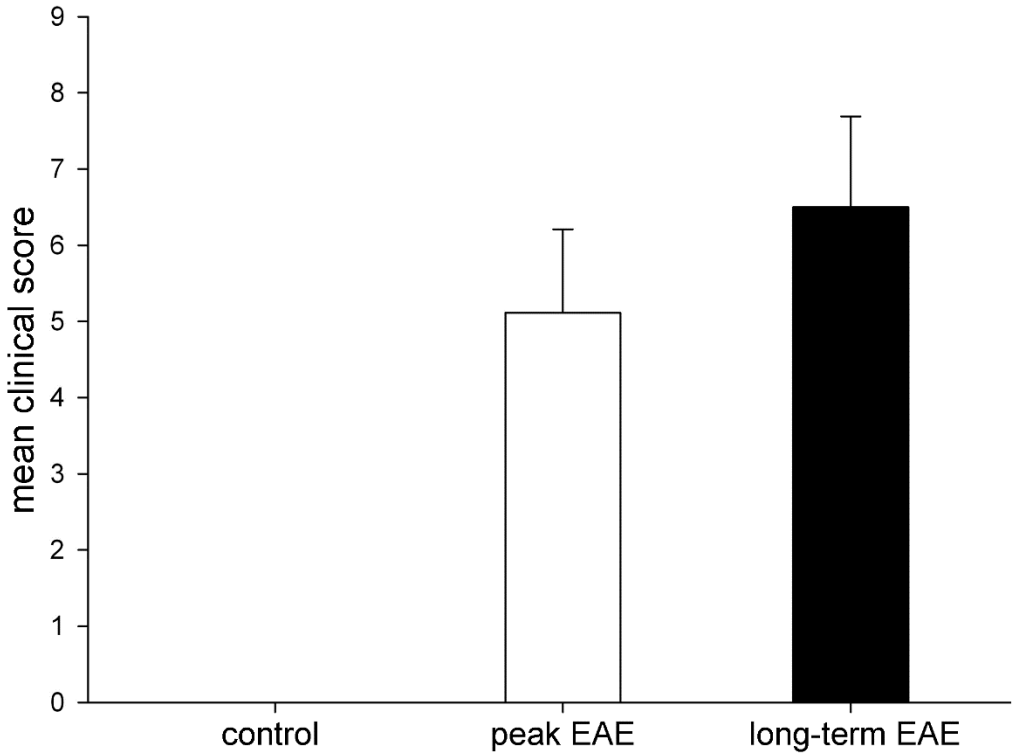

Figure 4.1 Average scores for motor disability for naïve control, peak EAE and long-term EAE mice on the day of imaging. All naïve controls (*n*=9) had scores of 0 while peak EAE mice (*n*=9) had scores of 5.1 ± 1.1 (mean ± SEM) and long-term EAE mice (*n*=4) had scores of 6.5 ± 1.2.

4.3.2 Responses of vascular hypointensities to hyperoxygenation

As shown previously, SWI shows hypointensities that likely relate to intravascular deoxyhemoglobin in the lumbar spinal cords of EAE mice. These hypointensities have been observed at the grey/white matter boundary of the spinal cord and in the spinal pia mater (Nathoo et al., 2013). With hyperoxygenation, it would be expected that deoxyhemoglobin concentration in the veins would decrease, and that hypointensities would become less dark. In fact, with hyperoxygenation, three different types of responses were observed. In the presence of 100% O_2, hypointensities either: disappeared completely (**Figure 4.2a**); became less dark, but did not disappear completely (**Figure 4.2b**); or became hyperintense (bright) (**Figure 4.2c**).

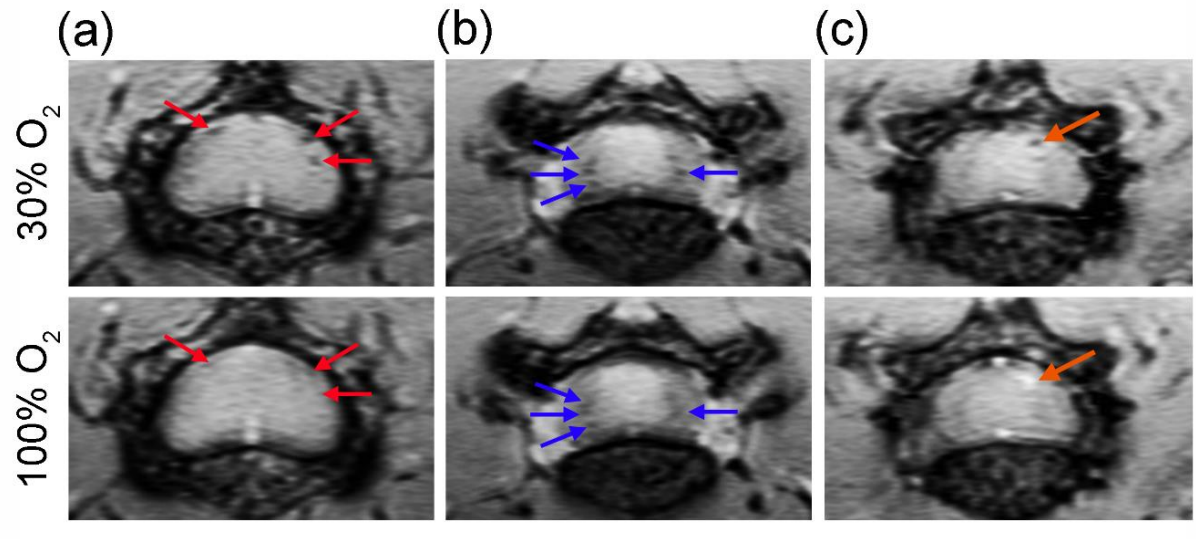

Figure 4.2 Deoxyhemoglobin-based SWI hypointensities in the lumbar spinal cords of EAE mice that appear hypointense with 30% O_2 show various responses upon administration of 100% O_2. (a) shows that some hypointensities seen with 30% O_2 disappear with 100% O_2 (red arrows). **(b)** shows that some hypointensities seen with 30% O_2 become less dark with 100% O_2, but do not disappear completely (blue arrows). **(c)** shows that some hypointensities seen with 30% O_2 become hyperintense with 100% O_2 (orange arrow).

4.3.3 Vascular hypointensities that alter in appearance with hyperoxygenation disappear after perfusion

A subset of naïve control mice (*n*=4) and long-term EAE mice (*n*=4) were imaged with 30% O_2, 100% O_2 and after perfusion, as the perfusion method had provided good visualization of hypointensities disappearing after perfusion, indicative of those hypointensities being due to deoxyhemoglobin (Nathoo et al., 2013). With these mice for which three imaging acquisitions were carried out, hypointensities seen with 30% O_2 which changed in appearance with 100% O_2 (any of the response types listed above), disappeared after perfusion (**Figure 4.3**). This phenomenon was observed in both naïve control and EAE mice, and did not depend on what type of response was seen with 100% O_2, so long as the appearance with 100% O_2 was different from that seen with 30% O_2. Taken together, these data support the notion that hypointensities which changed with hyperoxygenation were due to deoxyhemoglobin.

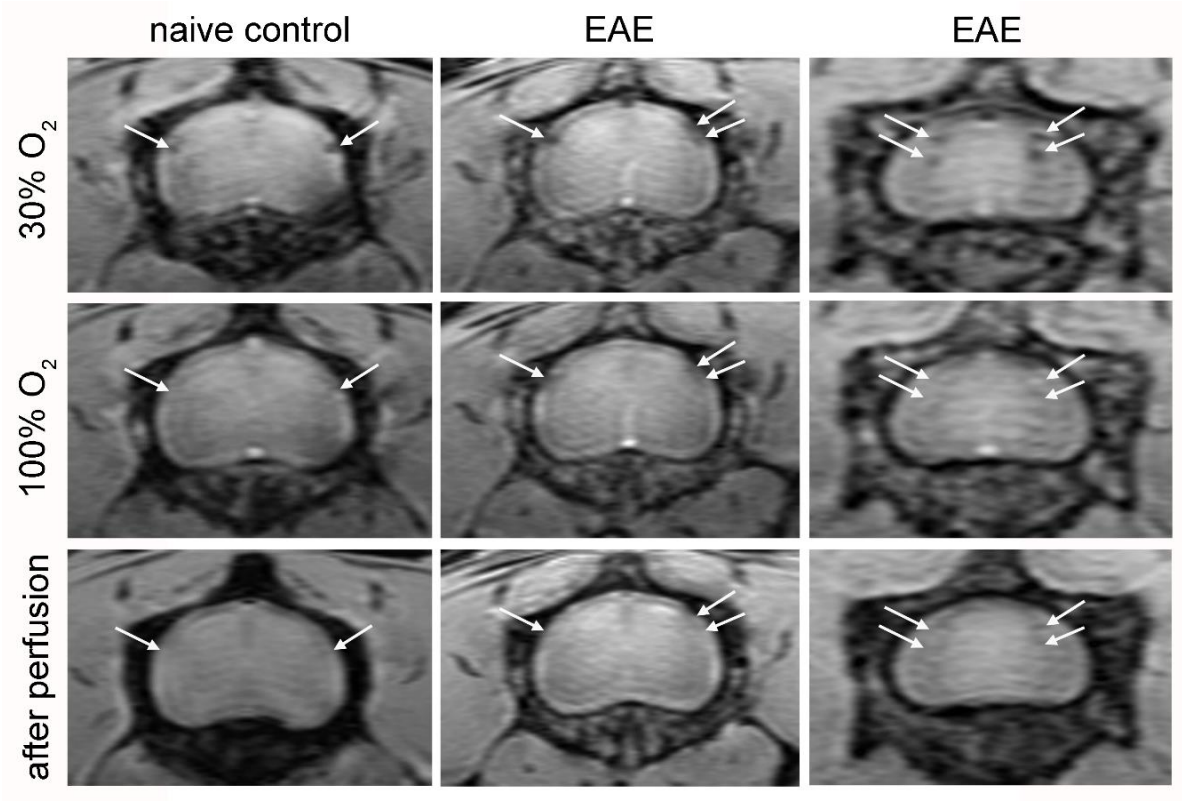

Figure 4.3 Hypointensities observed with 30% O_2 that change in appearance with 100% O_2 disappear after perfusion, supporting that they are due to deoxyhemoglobin. The left column shows SWI MR images obtained in a naive control mouse where hypointensities visible with 30% O_2 disappear with 100% O_2 and are not present after perfusion (white arrows). In the EAE mice shown in the middle and right columns, hypointensities seen with 30% O_2 show different responses with 100% O_2; some disappear after perfusion (white arrows). Hypointensities seen with 30% O_2 that alter in appearance or disappear with 100% O_2 are likely due to intravascular deoxyhemoglobin.

4.3.4 Most hypointensities seen with 30% O_2 change in appearance with 100% O_2

For hypointensity counting, only peak EAE mice that had a behavior score of 6 or above during the disease course were included. An additional animal was excluded as it did not respond to high oxygen at all. For peak EAE mice included for counting (n=6) and naïve control mice (n=9), analysis was first carried out to determine the effects of two factors on the number of hypointensities: animal type (control vs. peak EAE) and oxygen concentration (30% vs. 100%). It was found that both factors were significant (p<0.001 for each factor, two-factor univariate repeated measures ANOVA). This enabled for carrying out individual comparisons.

There was a significant difference in the number of hypointensities seen with 30% O_2 between naïve control mice (8.3 ± 0.9; mean ± SEM) and peak EAE mice (15.1 ± 1.7) (p=0.002, independent t-test). The number of hypointensities seen with 30% O_2 that did not change in appearance with 100% O_2 (the three response types listed in section 4.2.2) was significantly lower than the total number of hypointensities seen with 30% O_2 in both naïve controls (p<0.001, paired t-test) and peak EAE mice (p=0.009, paired t-test). Furthermore, the number of hypointensities that did not change in appearance with 100% O_2 was significantly greater in peak EAE mice (6.5 ± 1.6) than in naïve controls (1.2 ± 0.5) (p=0.003, independent t-test) (**Figure 4.4a**).

The breakdown of response types was also compared between controls and peak EAE mice. It was observed that 2 of 6 peak EAE mice had hypointensities that became hyperintense, whereas all naïve controls (9 of 9) had hypointensities that became hyperintense with 100% O_2. The average number of hypointensities that disappeared in naïve controls (3.1 ± 0.5; mean ± SEM) and peak EAE mice (3.2 ± 0.9) was not

significantly different between the two groups (p=0.911, independent t-test). The average number of hypointensities that became less dark but did not disappear completely was not significantly different between naïve controls (2.6 ± 0.7) and peak EAE mice (5.3 ± 1.5) (p=0.095, independent t-test). However, the average number of hypointensities that became hyperintense was significantly different between naïve controls (1.4 ± 0.5) and peak EAE mice (0.2 ± 0.1) (p=0.006, Mann Whitney U-test) (**Figure 4.4b**).

Of the total number of hypointensities seen with 30% O_2 in all naïve control mice combined, 85.2% altered in appearance when 100% O_2 was administered. Within the percentage of hypointensities that did change, 43.3% disappeared completely, 36.2% became less dark but did not disappear completely and 20.5% became hyperintense (**Table 4.1**). In all peak EAE mice combined, of the total number of hypointensities seen with 30% O_2, 56.9% altered in appearance when 100% O_2 was administered. Within the percentage of hypointensities that did change, 36.9% disappeared completely, 61.2% became less dark but did not disappear completely and 1.9% became hyperintense (**Table 4.1**).

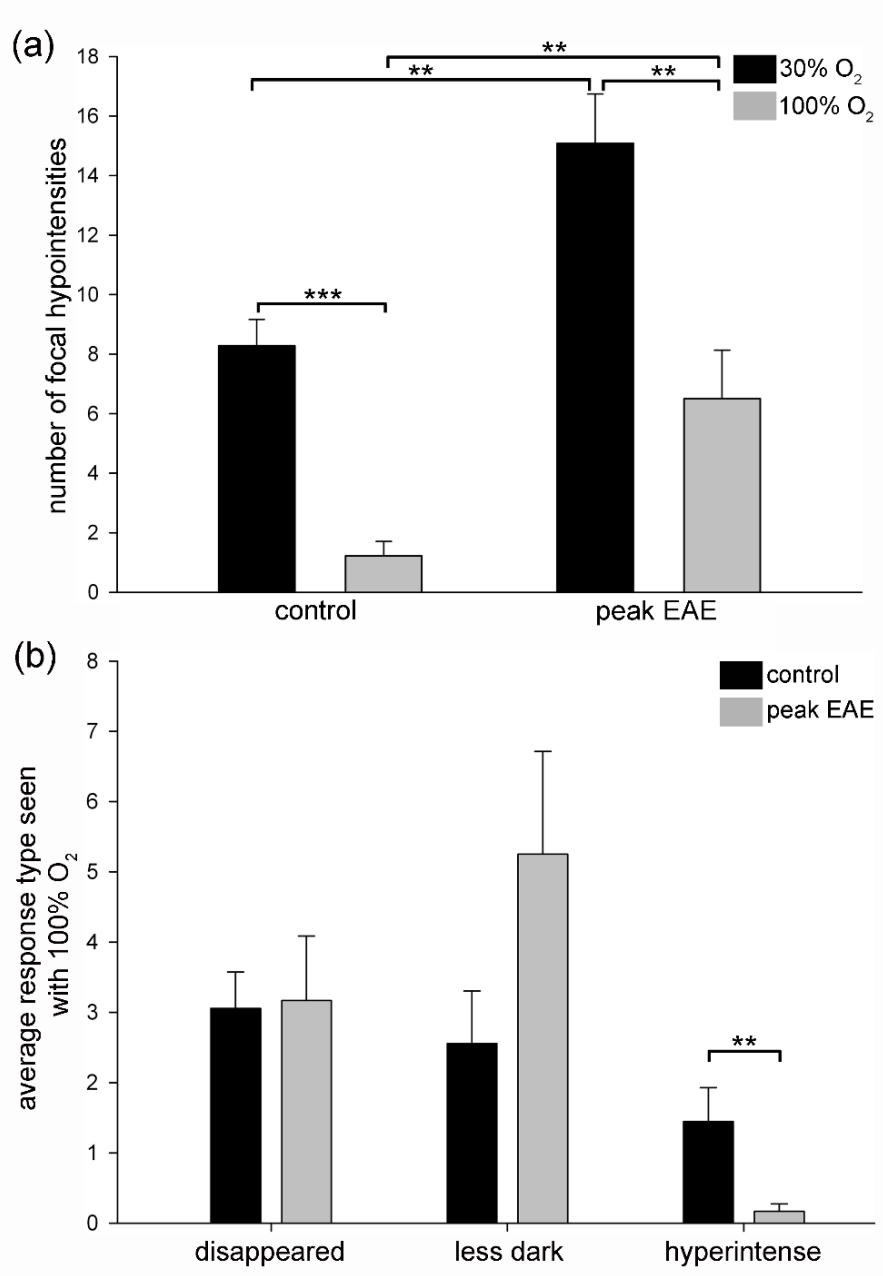
(a)
number of focal hypointensities
18
16
14
12
10
8
6
4
2
0
**
**
**
***
30% O2
100% O2
control
peak EAE
(b)
average response type seen with 100% O2
8
7
6
5
4
3
2
1
0
control
peak EAE
**
disappeared
less dark
hyperintense

Figure 4.4 The majority of hypointensities seen with 30% O_2 alter in appearance with 100% O_2 and the proportion of the various responses seen with 100% O_2. (a) shows the number of hypointensities seen with 30% O_2 and the number of hypointensities that do not change in appearance with 100% O_2. In both controls and peak EAE mice, the number of focal hypointensities that do not change in appearance with 100% O_2 is significantly lower than the total number of hypointensities seen with 30% O_2. **(b)** shows the average response type seen with 100% O_2, namely hypointensities disappearing, hypointensities becoming less dark but not disappearing completely and hypointensities becoming hyperintense. The number of hypointensities that became hyperintense upon administration of 100% O_2 was significantly greater in control mice than in peak EAE mice.

$^{**}p<0.01$ and $^{***}p<0.001$ by paired *t*-test in (a), $^{**}p<0.01$ by Mann-Whitney U test in (b).

Table 4.1 Proportion of response types to 100% O_2 for all animals combined

		Response type (%)	
Animal type	Disappear	Less dark	Hyperintense
Control	43.3	36.2	20.5
Peak EAE	36.9	61.2	1.9

4.4 Discussion

In this study, we have shown that altering the inspired oxygen concentration in combination with *in vivo* SWI provides a means to identify hypointensities due to intravascular deoxyhemoglobin. This method could be translated to the clinic, where 100% O_2 could be used to identify hypointensities due to deoxyhemoglobin with SWI. In MS patients, 100% O_2 has been used safely in the form of hyperbaric oxygen therapy (Fischer et al., 1983; Ansari et al., 1986).

In EAE studies, 100% O_2 has been used as part of the inhalation gas in EAE to differentiate microglia/macrophages containing iron nanoparticles from venous blood vessels (Wuerfel et al., 2007; Engberink et al., 2010), supporting use of this method for future studies in the EAE model. In our study, no animals died during imaging even though they were under anaesthetic for nearly three hours and underwent a drastic change in O_2 concentration, suggesting that this is a safe method to use.

In our study, most hypointensities were vascular and changed in the presence of 100% O_2. Specifically, three different responses were observed: 1) hypointensities disappeared, 2) hypointensities became less dark but did not completely disappear, or 3) hypointensities became hyperintense. The most common response in EAE mice was that hypointensities became less dark, but did not disappear completely whereas the most common response in controls was that hypointensities disappeared. Furthermore, only one third of peak EAE animals had hypointensities become hyperintense while all controls had hypointensities become hyperintense with 100% O_2. One possible reason for these varying responses is that the vessels had different oxygen saturations to begin with. Lower oxygen

saturation in spinal cord vessels of EAE mice would be suggestive of venous hypoxia in EAE.

It should be noted that in this study, we did not see any obvious parenchymal lesions. That is, no lesions appeared in the white matter that could be attributed to a lesion using histopathology. However, we had observed hypointensities in the white matter that remained after perfusion in our previous study, but this was present very infrequently (Nathoo et al., 2013).

It is worth noting that, when switching from 30% O_2 to 100% O_2, the animal must be monitored closely as there is a chance for a significant change in respiration which may cause a shift in the position of the spinal cord. This may lead to imperfect co-localization between images obtained at 30% O_2 and 100% O_2 even if the animal has not been moved and the only alteration is the inspired oxygen concentration.

An alternative to 100% O_2 for altering the appearance of the venous vasculature is carbogen, (95% O_2/5% CO_2), which acts to increase blood flow (Ashkanian et al., 2009). Carbogen has been used to reduce the contrast provided by veins visualized with SWI in healthy humans and in subjects with glioblastoma (Rauscher et al., 2005). However, hypercapnia can lead to increased intracranial pressure (Vigue et al., 2000) and carbogen is not always well tolerated; thus, it was not used in our study, although it is expected that it would have reduced visibility of the venous vasculature.

Here, we have shown that altering the inspired oxygen concentration is a viable method to identify deoxyhemoglobin-based SWI hypointensities in the EAE mouse spinal cord, and could be implemented in the clinic. That is, MS patients could be imaged with SWI first breathing air followed by breathing 100% O_2 and images obtained could be

compared for changes in hypointensities. This method can be used to determine the relative contribution of deoxyhemoglobin to SWI hypointensities *in vivo* in studies imaging at multiple time points, both in EAE and in MS.

Chapter Five: Susceptibility weighted imaging detects early venous changes in the lumbar spinal cord of mice with experimental autoimmune encephalomyelitis

5.1 Introduction

SWI has been used to study the venous vasculature in MS patients and in the EAE model. SWI has been used to detect lesions centered on veins in MS (Grabner et al., 2011; Kau et al., 2013) and in EAE (Gaitan et al., 2014). SWI has also shown reduced visibility of the venous vasculature in some brain regions in MS patients (Ge et al., 2009; Zivadinov et al., 2011). This phenomenon is proposed to be due to a combination of both reduced metabolism (Ge et al., 2009; Zivadinov et al., 2011) and alterations in venous morphology (Zivadinov et al., 2011).

Differing visibility of vessels using SWI will relate to the changing content of deoxyhemoglobin in the voxel. Vessel alterations could reflect changes in metabolism as inflammatory cells in the vicinity of a lesion require energy for cellular processes. This increased metabolism could also lead to an increase in oxygen extraction fraction (OEF) which would also increase levels of deoxyhemoglobin. Elevated deoxyhemoglobin content would be suggestive of hypoxia, which has been shown in the cerebellum and lumbar spinal cord of EAE mice at peak and chronic disease using SWI (Nathoo et al., 2013). In that study, the majority of SWI lesions were attributed to deoxyhemoglobin. This was assessed by imaging animals before and after perfusion under the premise that SWI lesions due to deoxyhemoglobin would be seen before perfusion, but would disappear after perfusion (Nathoo et al., 2013). Hypoxia has been shown to be present during peak disease and relapse in the lumbar spinal cord of a rat model of EAE (Davies et al., 2013), and

mRNA levels of HIF-1α are elevated in mice with relapsing-remitting EAE and chronic EAE (Mengozzi et al., 2008). HIF-1α content is also elevated in the brain tissue of MS patients, in lesions (Aboul-Enein et al., 2003) and in NAWM (Zeis et al., 2008).

Vascular changes have been shown to precede clinical signs in the EAE model. In particular, there is an early loss in vascular integrity with a breakdown in the BBB before EAE mice become show signs of motor dysfunction (Boroujerdi et al., 2013). Interestingly, later in the disease course, the loss of vascular integrity was observed primarily in venules (Boroujerdi et al., 2013). Another study observed venous abnormalities in cortical veins of EAE mice prior to them showing signs of motor dysfunction using MRI (Waiczies et al., 2012), but this observation was not expanded on, and these animals were not followed throughout the EAE disease course. Enlargement of blood vessels in the lumbar spinal cord has been documented in EAE rats with behavioral deficits (Davies et al., 2013). Angiogenesis leading to increased vascular density (and therefore increased deoxyhemoglobin) has been shown to take place in both MS (Ludwin et al., 2001) and in the EAE model (Seabrook et al., 2010; Macmillan et al., 2011). In EAE, new blood vessels appear in both grey and white matter and are not necessarily related to demyelinating lesions (Seabrook et al., 2010; Macmillan et al., 2011). Taken together, it is appears that dynamic changes are taking place in the venous vasculature throughout the EAE disease course, even prior to the appearance of motor dysfunction.

To date, studies using SWI in MS have not looked at changes to the venous vasculature over time. As EAE is used as an inflammatory model of MS and it shows SWI based lesions similar to MS patients, the model provides the opportunity to investigate the relationship between SWI lesions of venous origin and disease progression. The aim of this

study was to investigate what are suspected to be lumbar spinal cord venous changes over the EAE disease course non-invasively using serial SWI MRI. The use of SWI in animal models of MS may complement knowledge being gleaned in MS patients with SWI, thereby augmenting our understanding of venous changes taking place in both conditions.

5.2 Specific methods

5.2.1 Imaging time points

Naïve control (*n*=3) and EAE mice (*n*=9) were imaged serially a minimum of four times: 1) baseline, 2) 7 days, 3) 12 days and 4) 16-18 days post-immunization. For EAE mice, baseline imaging was done one day prior to EAE immunization in order to minimize the amount of anaesthetic mice were exposed to in one day. The 7 day time point is prior to clinical signs of motor dysfunction, while the 12 and 16-18 day time points are the expected periods for onset and peak clinical signs, respectively. Naïve control mice were matched with EAE mice for imaging time points, and naïve mice were always imaged alongside EAE mice. A subset of EAE mice (*n*=4) was also imaged at a time point of long-term or chronic disease, 40-41 days post-immunization. These mice were imaged both live (pre-perfusion) and after perfusion (post-perfusion).

5.2.2 Analysis of SWI hypointensity counting

In order to compare the changes in the number of SWI hypointensities seen at the different time points, and to take into account the variability in the number of SWI hypointensities seen at baseline between the different animals, the ratio was taken for the

number of SWI hypointensities at a given time point to the number of SWI hypointensities seen at baseline:

ratio = number of SWI hypointensities at time point (e.g. day 7)/
number of SWI hypointensities at baseline

This enabled the comparison of the number of hypointensities at each time point (7 days, 12 days, 16-18 days) to baseline values. One EAE animal (which had been kept until long-term disease) was excluded from the calculation of ratios as the baseline data acquisition had too much artefact to enable counting of hypointensities for that time point.

5.2.3 Pre- and post-perfusion MRI acquisitions for mice destined for pimonidazole staining

Pimonidazole is a 2-nitroimidazole (**Figure 5.1**) which binds to cells in the presence of low oxygen concentrations (hypoxia). More specifically, pimonidazole is oxidized in the presence of adequate oxygen, but is reduced in hypoxic conditions (pO_2 <10 mmHg). Under low oxygen conditions, electrons bind to the nitro-aromatic compounds rather than to oxygen (Arteel et al., 1995). Reduced pimonidazole binds to thiols like glutathione and proteins containing thiols and subsequently accumulates in tissue (Arteel et al., 1998).

A different set of EAE mice at different time points were used for this part of the study (*n*=3; 2 used at 7 days, 1 used at 20 days which was showing significant signs of

motor disability). EAE mice were administered pimonidazole HCl (Hypoxyprobe Inc, Burlington, USA) i.p. 15 minutes prior to pre-perfusion (*in vivo*) MRI at a dose of 60 mg/kg body weight. The powder was dissolved in sterile saline and injected at a final volume of 150 µL. This method of administering pimonidazole enabled for direct comparison of SWI lesions with pimonidazole staining as both were carried out under the presence of anaesthesia. Upon completion of *in vivo* MRI (approximately one and a half hours later), mice were perfused and sacrificed using PBS and 10% formalin as described above, and then were immediately re-imaged post-perfusion.

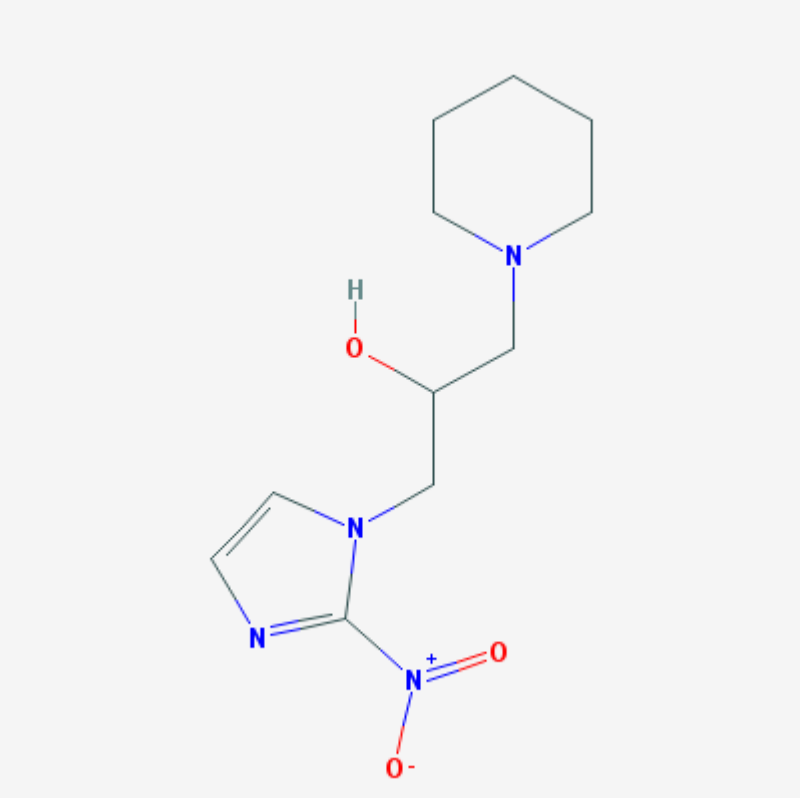

Figure 5.1 Structure of pimonidazole.

5.2.4 Pimonidazole staining for hypoxia

Sections were deparaffinized with xylene and hydrated using a graded alcohol series ending in PBS. Antigen retrieval was carried out using sodium citrate buffer at 80°C for 30 minutes. Sections were cooled to room temperature, washed in PBS for 10 minutes, then tissue peroxidase was quenched using 3% hydrogen peroxide for 30 minutes. Sections were washed in PBS for 10 minutes, and then blocked using 10% goat serum for 1 hour. Following this, primary antibody was diluted in PBS (1:50 FITC conjugated to mouse IgG_1 monoclonal antibody) and incubated in tissue at 4°C overnight. Sections were then washed in PBS for 10 minutes and secondary antibody (horseradish peroxidase linked to rabbit anti-FITC) was diluted in PBS (1:100) and applied for 1 hour at room temperature. Sections were washed in PBS twice for 5 minutes each time and then incubated in DAB for 5 minutes. Sections were washed with distilled water for 10 minutes, counterstained with hematoxylin, washed in distilled water for another 10 minutes, dehydrated, and coverslipped using the mounting medium Permount.

5.2.5 Statistical analysis

Spearman's rank correlation was used to compare EAE clinical score with the ratio of SWI hypointensities, as the data was not normally distributed and did not have equal variance. An independent *t*-test was used to compare the number of SWI hypointensities at baseline between naïve mice and mice destined to be induced with EAE. A $p \leq 0.05$ was considered significant for all statistical tests.

5.2.6 SWI hypointensity counting is correlated between two blinded researchers

To determine how consistent counting of hypointensities was between the two blinded researchers, correlation analysis was carried out for data acquired at each time point for each animal. There was a significant moderate to strong positive correlation for counting of hypointensities between the two researchers for the time course data ($r=0.673$, $p<0.001$, Pearson's correlation), indicating that counting was consistent between individuals.

5.3 Results

5.3.1 SWI hypointensities are darker and larger in EAE mice and are present before onset of motor disability

SWI hypointensities in EAE mice during the disease course are darker and larger (assessed by eye, not measured) than those seen in naïve controls or at baseline (pre-induction). In EAE mice, substantial changes in the presence and appearance of hypointensities were already visible at the 7 day time point (**Figure 5.2**). Changes in SWI hypointensities were observed in 5 of 8 EAE mice by day 7. Based on our scoring system, no motor disability was detected at day 7 even though SWI based hypointensities were, indicating that SWI hypointensities can precede motor dysfunction.

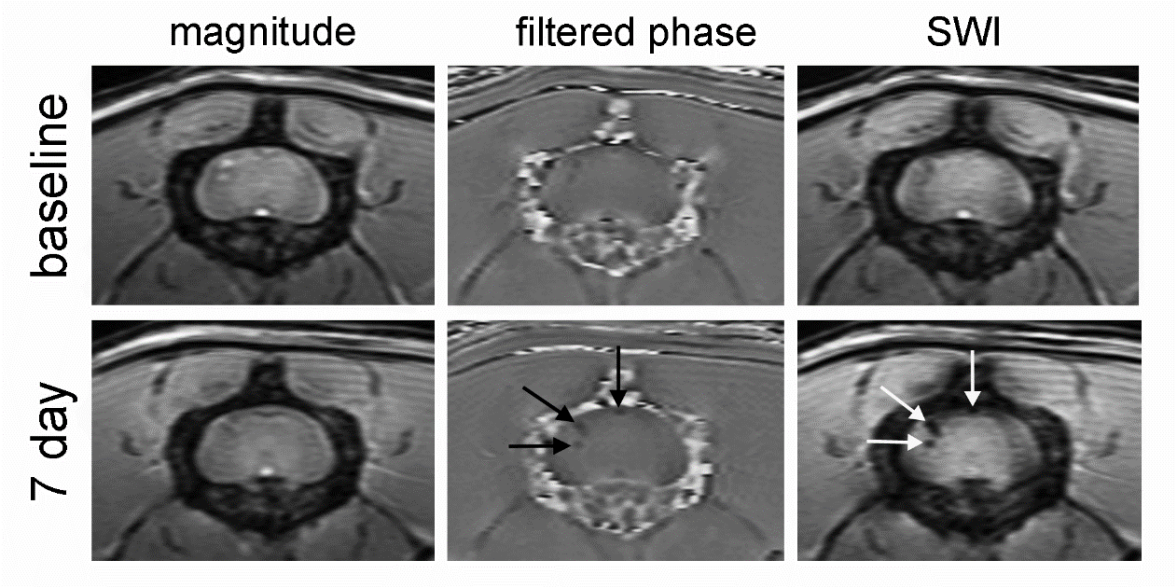

Figure 5.2 SWI hypointensities darken and enlarge, and are prominent before onset of motor dysfunction in the lumbar spinal cords of EAE mice. Representative MR images of EAE mouse lumbar spinal cord are shown at baseline (pre-induction) and 7 days later, before onset of motor dysfunction. Magnitude images (left column) do not show any hypointensities. Filtered phase images (middle column) and SWI images (right column) are created upon carrying out SWI processing. These two image types show hypointensities at the 7 day time point (black and white arrows). Hypointensities in EAE mice (day 7 onwards) are larger and appear darker and larger than hypointensities in naïve controls or pre-induction (baseline).

5.3.2 SWI hypointensities evolve over the EAE disease course

The appearance of SWI hypointensities did not change in terms of numbers or size amongst naïve controls over the imaging time points (**Figure 5.3a**). However, there was great heterogeneity amongst EAE mice with respect to the appearance and evolution of SWI hypointensities. In some EAE mice, hypointensities appeared prominently at the 7 day time point (**Figure 5.3b**), after which hypointensities appeared less dark at the 12 day and 17 day time points. In other EAE mice, hypointensities were not seen or not prominent until the 12 day time point (**Figure 5.3c**). In the example shown (**Figure 5.3c**), hypointensities became less prominent by peak disease (16 days) as compared to the 12 day time point, but were still visible. Other EAE mice had hypointensities appear prominently at peak disease (16 days), but not before that time point (**Figure 5.3d**).

The evolution of SWI hypointensities over the disease course was compared with EAE clinical scores. Examples of EAE clinical scores are shown for three mice in Figs. 5.2e-g. The EAE mouse in Fig 5.2b showed disability beginning at day 11 with a maximum at day 17, while SWI hypointensities were already most prominent by day 7 (**Figure 5.3e**). The clinical score for the EAE mouse shown in Fig. 5.2c was at a maximum at 12 days post-immunization, which corresponds to the time point at which SWI hypointensities appeared most prominently (**Figure 5.3f**). The clinical score for the EAE mouse shown in Fig. 5.2d was at maximum at 16 days post-immunization, which also corresponded to the time point at which SWI hypointensities appeared most prominently (**Figure 5.3g**). However, not all animals showed increased SWI lesions. Compared to the range in controls, 3 of 8 EAE animals did not show an increase in SWI lesions even though motor disability was high in one of the animals which had a behaviour score of 9; the other

two animals had maximum behaviour scores of 1 and 4, representing little motor deficit. Altogether, these data suggest that there is variation between animals in the time of onset of SWI lesions and the time relative to the onset of motor dysfunction.

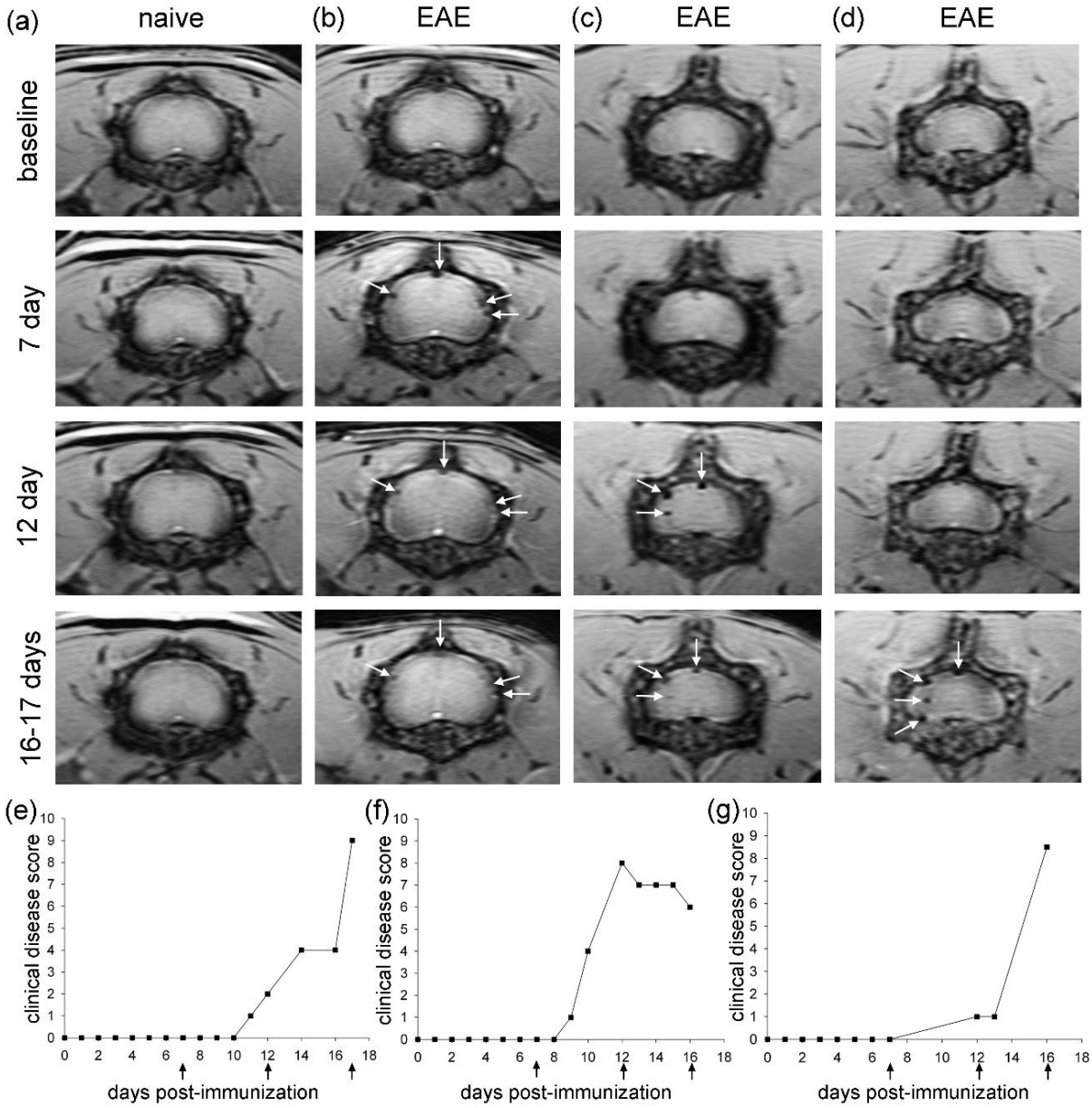
(a)
naive
(b)
EAE
(c)
EAE
(d)
EAE
baseline
7 day
12 day
16-17 days
(e)
(f)
(g)
clinical disease score
days post-immunization

Figure 5.3 The appearance of SWI hypointensities changes over time in the lumbar spinal cords of EAE mice, but not in naïve controls. (a) SWI MRIs of a naïve control mouse over the time points imaged. No differences are seen between images acquired at different time points. **(b) to (d)** show SWI MRIs of three different EAE mice over the time points imaged. Time points at which SWI hypointensities appeared prominently are shown (white arrows). It is evident that the time points at which SWI hypointensities appear most prominently are variable between different EAE mice (7 days in (b), 12 days in (c) and 16 days in (d). **(e) to (g)** show EAE clinical score graphs for the EAE mice shown in (b) to (d). In (e), the clinical score for the EAE mouse in (b) was at maximum at the 17 day time point (peak disease), while SWI hypointensities were already prominent at the 7 day time point before any motor disability was present. In (f) and (g), EAE clinical scores were highest at the time point when SWI hypointensities appeared most prominently, 12 days and 16 days respectively. SWI MRI are shown in (f) to (g) (black arrows), with baseline imaging taking place the day before day 0 (not shown on graphs).

5.3.3 SWI hypointensities disappeared after perfusion, indicating that these hypointensities are due to intravascular deoxyhemoglobin

With the subset of EAE mice (*n*=4) kept until long-term disease (40-41 days post-immunization), the contribution of deoxyhemoglobin to the hypointense signals seen with SWI was assessed by imaging *in vivo* and after perfusion. Hypointensities seen in EAE mice over the disease course were no longer detectible after perfusion, supporting the premise they are due to intravascular deoxyhemoglobin (**Figure 5.4**). This is in agreement with data published previously (Nathoo et al., 2013).

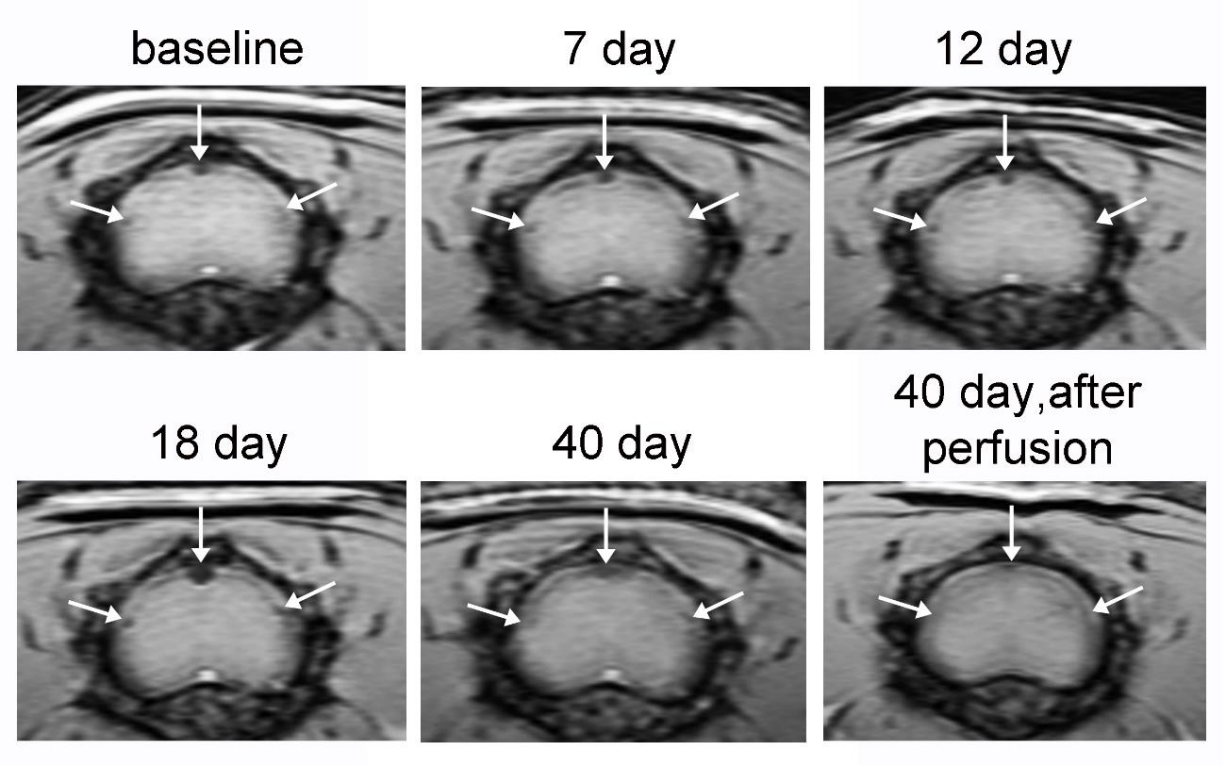

Figure 5.4 SWI hypointensities seen in the lumbar spinal cords of EAE mice over the EAE disease course disappeared after perfusion, supporting that they are vascular in origin. SWI MRIs are shown for an EAE mouse kept until long-term disease (40 days post-immunization). The areas where SWI hypointensities were seen are shown (white arrows in all images). It is apparent that after perfusion, all of these hypointensities disappear, supporting that they are due to intravascular deoxyhemoglobin.

5.3.4 The ratio of SWI hypointensities to baseline is highly variable in EAE mice, but not in naïve controls

To assess the changes in SWI hypointensity profile over time in naïve controls and over the EAE disease course, the ratio of the number of hypointensities to baseline was calculated for each time point. The range of ratios seen for naïve controls was 0.80 to 1.31 (**Figure 5.5a**). Naïve mice had ratios clustered around 1 (which is equal to the baseline value). Conversely, EAE mice had a wide range of ratios which was from 0.45 to 6.75 (excluding post-perfusion data) (**Figure 5.5b**). The majority of EAE mice (5/8) had ratios higher than the maximum ratio value (1.31) seen in naïve controls at some point during the EAE disease course. Of the EAE mice kept until long-term disease for which ratios could be obtained (n=3), one had a ratio of 2.83 and the other two had ratios below 1 (0.47 and 0.63) at the day 40-41 time point.

It should be noted that not all EAE mice showed an elevation in ratios. Overall, the EAE group showed heterogeneity in the number of hypointensities as compared to baseline, while such heterogeneity was not present in naïve control mice. Within individual EAE mice, variability was present in ratios over the disease course – the maximum difference between ratios in an individual EAE mouse was 2.85. Such variability was not seen in naïve controls, as the maximum difference between ratios for an individual naïve mouse was 0.50. Also, half of the EAE mice (4/8) showed recovery of ratios towards baseline after reaching maximum value. Taken together, these data suggest that dynamic changes take place in the venous vasculature in the lumbar spinal cords of EAE mice which can be detected with SWI.

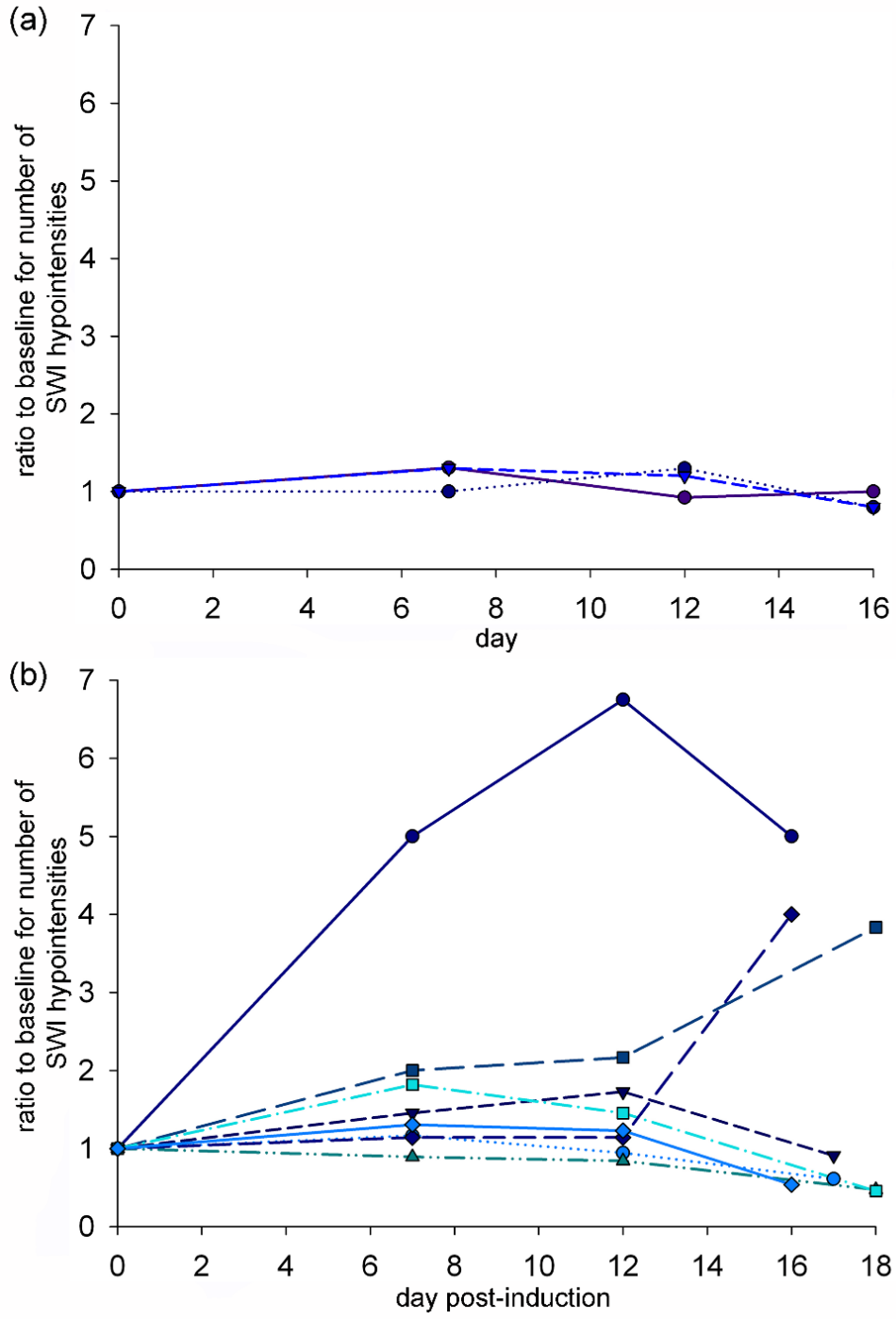
(a)
ratio to baseline for number of SWI hypointensities
day
(b)
ratio to baseline for number of SWI hypointensities
day post-induction

Figure 5.5 The ratio of the number of SWI hypointensities to baseline is highly variable for EAE mice, but not naïve controls. (a) Ratios of the number of hypointensities to baseline for each naïve control mouse (*n*=3). Ratios for naïve controls were clustered around 1 (range of 0.8-1.31). **(b)** Ratio of the number of hypointensities to baseline for each EAE mouse (*n*=8). Ratios for EAE mice varied widely (range of 0.45-6.75). These changes are suggestive of dynamic vascular alterations in EAE mice that can be detected with SWI.

5.3.5 The ratio of SWI hypointensities to baseline is not correlated with motor disability in EAE mice

The ratios of the number of hypointensities at a given time to that pre-induction were compared to EAE clinical scores. There was no correlation between the EAE clinical score and the ratio of SWI hypointensities in EAE mice (ρ= -0.013, p=0.950, Spearman's rank correlation) (**Figure 5.6**). However, there may be a threshold effect, as above a score of 3, much higher SWI lesion ratios were seen in over half the mice.

When comparing EAE clinical score with the ratio of the number of hypointensities for each individual EAE mouse, it was observed that only 2 of 8 EAE mice showed the greatest motor disability (highest EAE clinical score) on the same day as they had the maximum number of SWI hypointensities (**Table 5.1**). In the remainder of cases (6/8), the time point with the maximum number of SWI hypointensities preceded the time point of maximum motor disability. Thus, in no instance was the maximum number of SWI hypointensities observed after maximum motor disability. Furthermore, 3 of 8 EAE mice showed the maximum number of SWI hypointensities at the 7 day time point, suggesting that this is a phenomenon that takes place early in the EAE disease course.

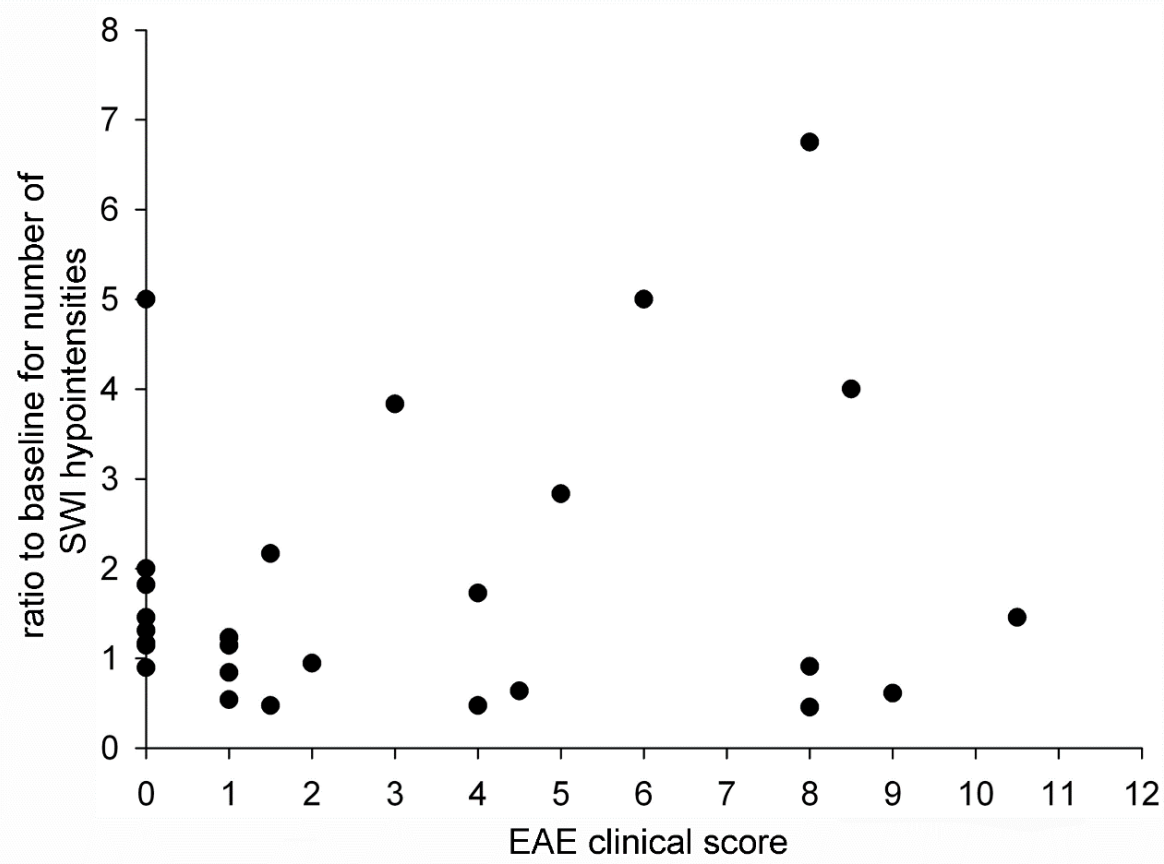

Figure 5.6 Comparison of EAE clinical scores and the ratio of SWI hypointensities to baseline. EAE clinical scores for all EAE mice for which ratios to baseline could be obtained (n=8) were plotted (for each time point) against the ratio of SWI hypointensities to baseline. It is apparent that there is no correlation between the two measures (ρ= -0.013, p=0.950, Spearman's rank correlation). However, at a score above 3, much higher ratios are seen in about half of the mice, suggestive of a threshold effect.

Table 5.1 Comparison of EAE clinical score with ratio of SWI hypointensities (to baseline) for individual animals

Animal	Day(s) post-immunization with maximum EAE clinical score	Maximum EAE clinical score (/15)	Day post-immunization with maximum ratio of SWI hypointensities	Maximum ratio of SWI hypointensities
EAE-1	12	8	12	6.75
EAE-2	18	9	7	1.17
EAE-3	18	8	12	1.72
EAE-4	40	4	Baseline	1.00
EAE-5	22	8.5	18	3.83
EAE-6	12-15	10.5	7	1.82
EAE-7	16	8.5	16	4.00
EAE-8	12, 13, 16	1	7	1.31

5.3.6 SWI hypointensities for EAE mice imaged at a single-time point and pimonidazole staining

With the set of EAE mice imaged at a single time point before and after perfusion (n=3, 2 at 7 days and 1 at 20 days) and which were stained with pimonidazole, the SWI hypointensity profile was compared with tissue staining for hypoxia. The mice at 7 days did not show signs of motor disability while the mouse at 20 days had an EAE clinical score of 10, indicative of significant motor disability. Example SWI MRIs before and after perfusion are shown for the two time points investigated (**Fig. 5.7a**). The EAE mouse at 7 days (shown in Fig. 5.7a) had 12 SWI hypointensities before perfusion and 1.5 after perfusion while the EAE mouse at 20 days had 6.5 SWI hypointensities before perfusion and 0.5 after perfusion (**Fig. 5.7b**).

As these EAE mice were only imaged once (with no baseline MRI), the number of SWI hypointensities at baseline across all animals imaged through the time course (naïve and EAE, n=11) were averaged and ratios were calculated using this average value (5.54) as there was no significant difference between naïve and EAE-induced mice for the number of SWI hypointensities at baseline (p=0.975, independent t-test). The ratio of SWI hypointensities to baseline for the EAE mouse shown at 7 days post-immunization before perfusion was 2.25, while the EAE mouse at 20 days post-immunization pre-perfusion had a ratio of 1.17. The ratio of SWI hypointensities to baseline after perfusion for the EAE mouse shown at 7 days was 0.27 while the EAE mouse at 20 days had a ratio of 0.09 after perfusion. Thus, the ratio of SWI hypointensities to baseline before perfusion for the EAE mouse at 7 days exceeds the range seen in naïve mice while the EAE mouse at 20 days falls within the range seen in naïve mice.

Histology was carried out for hypoxia and general histology/inflammation for the EAE mice imaged at a single time point (**Fig. 5.7c**). Pimonidazole staining was present at the 7 day time point, before any signs of motor disability. Furthermore, there were no obvious signs of inflammation as shown with hematoxylin & eosin staining. Pimonidazole staining was also seen in the dorsal column of the spinal cord in the EAE mouse at the 20 day time point; however, inflammation was visible with hematoxylin & eosin staining. Thus, venous changes suggestive of venous hypoxia and tissue hypoxia are present before the onset of motor disability and prior to any obvious signs of inflammation (specifically cellular infiltration) in the lumbar spinal cord of EAE mice.

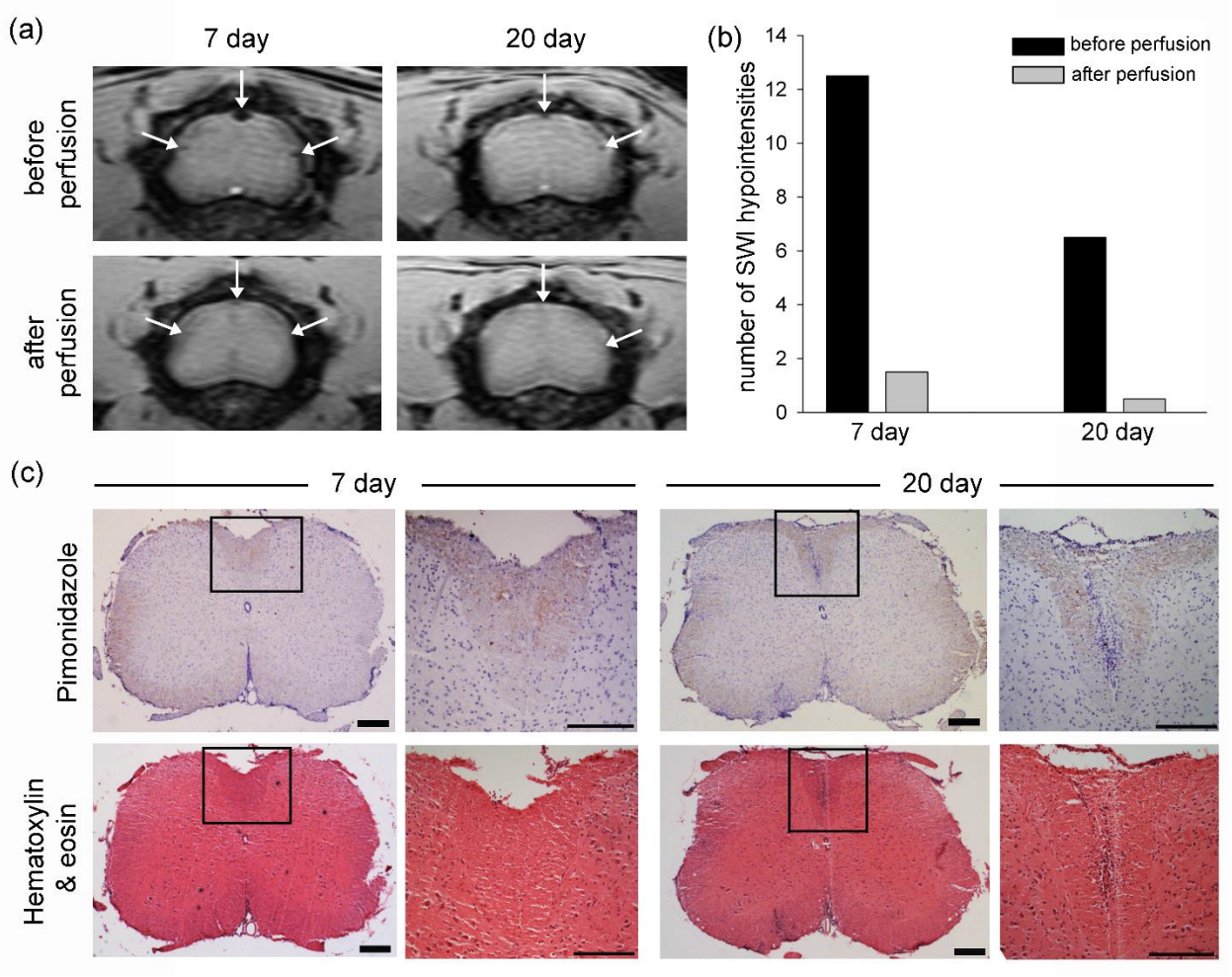
(a)
7 day
20 day
before perfusion
after perfusion
(b)
number of SWI hypointensities
14
12
10
8
6
4
2
0
before perfusion
after perfusion
7 day
20 day
(c)
7 day
20 day
Pimonidazole
Hematoxylin & eosin

Figure 5.7 Single time-point pre- and post-perfusion SWI and histology for 7 days and 20 days post-immunization. (a) SWI MRIs of EAE mice imaged at 7 days and 20 days post-immunization, both before and after perfusion. SWI hypointensities appear more prominent in the 7 day EAE mouse compared to the 20 day EAE mouse before perfusion (white arrows). Hypointensities seen before perfusion disappear after perfusion in both animals (white arrows), supporting that they are due to deoxyhemoglobin. **(b)** The number of SWI hypointensities seen before and after perfusion in the EAE mice shown in (a). The 7 day EAE mouse has more SWI hypointensities than the 20 day EAE mouse, and most of the hypointensities seen before perfusion disappear after perfusion in both mice. **(c)** Pimonidazole and hematoxylin & eosin staining of the lumbar spinal cords of the EAE mice shown in (a) and (b). In the dorsal column of the 7 day EAE mouse, positive pimonidazole staining is seen for hypoxia (brown stain) with no obvious signs of inflammation (hypercellularity) in hematoxylin & eosin staining. In the dorsal column of the 20 day EAE mouse, positive pimonidazole staining is seen for hypoxia (brown stain) which appears to be stronger than that seen in the 7 day EAE mouse. However, inflammation can be seen with hematoxylin & eosin staining in the same region as where there is pimonidazole staining in the day 20 EAE mouse.

Scale bars in (c): 400μm (left images), 200μm (right images).

5.4 Discussion

SWI-visible lesions are seen in MS patients (Haacke et al., 2009a) and in the EAE animal model of MS (Nathoo et al., 2013). However, it is not known if these SWI lesions in MS patients relate to iron deposition, demyelination, deoxyhemoglobin, or some combination of these. Many SWI lesions in this study are likely not due to iron deposition. This is supported by the observation that when the blood is removed and MRI is undertaken immediately, most of these lesions are no longer visible (Nathoo et al., 2013). These observations have lead us to conclude that in the EAE model, most of the SWI lesions are venous in origin, reflecting increases in deoxyhemoglobin in the draining veins. This may be due to enlarged veins, more veins, and/or reduced OEF in the veins.

In MS patients, reports are fairly consistent in reporting changes in the qualitative appearance of vessels using SWI. The two studies that have shown reduced visibility of the venous vasculature with SWI in MS patients reported that the pattern of vessels was less pronounced in various brain regions (Ge et al., 2009; Zivadinov et al., 2011); in one of the studies, they suggested this was due to reduced OEF (Ge et al., 2009). However, they did not report changes elsewhere (e.g. cerebellum, spinal cord). Others have noted hypointensities on SWI that were attributed to iron deposition (Haacke et al., 2009a), but could also be related to tortuous vessels with more deoxyhemoglobin. Both observations are consistent with a heterogeneous response, and with some regions having higher deoxyhemoglobin. To our knowledge, there have not been studies of venous vasculature visibility in the cerebellum or spinal cord in MS patients. We have not quantified SWI-based lesion load in the cortex or basal ganglia. As a result, direct comparisons cannot be made. Until studies with MS patients look in the spinal cord and cerebellum and/or EAE

studies look at the cortex, it will not be known if this phenomenon of SWI hypointensities due to deoxyhemoglobin is a phenomenon only in EAE or in MS as well.

However, it is worth noting that in the EAE mice kept till later time points, particularly until long-term disease (days 40-41 post-induction), the ratio of SWI hypointensities was much lower in 2 of the 3 animals (lower than 1, which is equal to baseline). Based on our data, the venous vasculature is most visible early in the EAE disease course. Therefore, it is possible this phenomenon is seen in MS as well – that early in the disease, the venous vasculature is more visible, but that it decreases over the disease course. Studies of the venous vasculature have been carried out in RRMS (Ge et al., 2009; Zivadinov et al., 2011) and SPMS (Zivadinov et al., 2011) – time points at which MS patients already show symptoms. It is not currently known what the visibility of the venous vasculature is very early in the MS disease course.

The increased deoxyhemoglobin in the veins observed is likely caused either by increased OEF and/or increased vessel diameter. An increased OEF will correlate with a relatively hypoxic environment, meaning that tissue oxygenation will decline. We found only one study reporting OEF using PET; this study reported no changes in MS patients relative to controls (Brooks et al., 1984). The premise of a hypoxic environment is supported not only by our SWI MRI data, but also by increased staining with the hypoxia marker pimonidazole in the lumbar spinal cord of EAE mice. Hypoxia has also been detected in the lumbar spinal cord of a rat EAE model using tissue oxygen measurements and pimonidazole staining (Davies et al., 2013). Increased HIF-1α, a factor regulated in part by hypoxia, has been detected in MS lesions (Juurlink, 2013). SWI lesions such as

those reported in MS (Haacke et al., 2009a) are consistent with increased deoxyhemoglobin and increased OEF, at least in the microenvironment.

The hypoxia observed may or may not be severe enough to cause local cell damage, but any level of hypoxia will act to modulate genetic responses. In particular, there is a growing awareness of the link between hypoxia and inflammation (Eltzschig and Carmeliet, 2011). Inflammation can stimulate similar genetic changes to those caused by hypoxia (Rius et al., 2008) through inhibition of prolyl hydroxylases (Cummins et al., 2006). These include factors which would inhibit mitochondrial respiration such as an elevation in pyruvate dehydrogenase kinase 1 (Papandreou et al., 2006). Inflammation is also associated with increased levels of ROS and nitric oxide which may damage or inhibit mitochondria (Brown and Neher, 2010; Mao and Reddy, 2010). ROS can modulate hypoxia by regulating the stability of HIF-1α (Greer et al., 2012). Inhibition of mitochondria could reduce metabolic rate, which would cause reduced blood flow and an increase in OEF (Hyder et al., 1998; Lei et al., 2001; Buxton et al., 2004). Furthermore, hypoxia can stimulate inflammation through the regulation of nuclear factor kappa-light-chain-enhancer of activated B cells (NF-κB), a master regulator of inflammatory responses (Koong et al., 1994).

It is possible that the venous changes we are seeing are due to inflammation, which coincides with other behavioral changes. An elevation in pro-inflammatory cytokines (IL-1β and TNF-α), concomitant with anxiety and depression-like behaviors, have been shown to take place before motor dysfunction onset in EAE mice (Acharjee et al., 2013). Neuropathic pain behavior, such as allodynia, precedes motor disability in the EAE model as well which appears to be related to inflammation (Olechowski et al., 2009).

Our SWI data show that venous changes may precede the onset of motor disability in EAE mice, and SWI hypointensities are always at a maximum before maximum motor dysfunction. An increase in vascular area and blood vessel density has been reported in the white matter of the spinal cord in EAE mice before changes in motor function (Boroujerdi et al., 2013). There is also a loss of vascular integrity concomitant with breakdown of the BBB by day 7, shown using immunohistochemistry for endothelial cells and fibrinogen (Boroujerdi et al., 2013). In that study, leukocyte infiltration was not seen in the spinal cord until day 14, one week after significant vascular alterations had taken place (Boroujerdi et al., 2013). When leukocytes did infiltrate the spinal cord, they were associated with post-capillary venules (Boroujerdi et al., 2013), which is in agreement with previous reports by others (Agrawal et al., 2006). It is also worth noting that in our study, SWI hypointensities normalize back to baseline in some EAE animals, but not in others. This variation in SWI hypointensities over EAE disease progression may relate to variability in the onset of hypoxia.

Interestingly, in addition to seeing high numbers of SWI hypointensities at the 7 day time point, tissue staining for hypoxia was also present at this time point. This is different from what has been published by another group that has carried out pimonidazole staining in the EAE model (Davies et al., 2013). The study by Davies et al. had observed little to no pimonidazole staining prior to rodents developing neurological deficits, and observed the greatest level of pimonidazole staining in rats with the highest EAE disease score (Davies et al., 2013). Another possible reason differences may have been seen include the fact that Davies et al. used a chronic-relapsing rat EAE model compared to our monophasic mouse EAE model; chronic relapsing EAE in rats typically have ascending

paralysis beginning on days 7-14 (Beeton et al., 2007) while our monophasic EAE mice typically begin showing ascending paralysis on days 9-11. However, both models use MOG as the encephalitogen. The dissimilarities between the models may explain the differences in pimonidazole staining, suggesting that more studies need to be conducted to determine the time points at which pimonidazole staining for hypoxia is present in the EAE disease course.

In summary, SWI data were used to show that there are venous alterations before any obvious motor dysfunction in the EAE mouse model. The increased evidence for SWI-based lesions supports the development of hypoxic conditions, which may be caused by chronic inflammation. This work supports a link between hypoxia and inflammation in the EAE model. This, in turn, suggests that SWI lesions may be a useful biomarker in MS, and supports further examination of venous alterations, hypoxia, OEF, and markers of disease progression.

Chapter Six: Pilot study using susceptibility weighted imaging to assess treatment response to dexamethasone in mice with experimental autoimmune encephalomyelitis

6.1 Introduction

Studies using susceptibility MRI in MS, including SWI, have focused on lesion detection, visualizing the venous vasculature and determining what signal changes mean. To the best of our knowledge, susceptibility MRI has not been used as a marker of treatment response; this is understandable considering it is still debated what susceptibility MRI methods are showing us with respect to pathology. However, with knowledge gleaned from previous aims about the presence of hypointensities with SWI that correspond to intravascular deoxyhemoglobin, we opted to test the usefulness of SWI for assessing treatment response using an anti-inflammatory treatment. The premise for pursuing this was the hypothesis that the elevated number of SWI hypointensities and the dynamic changes those SWI hypointensities undergo in EAE mice are likely related to inflammation, and therefore, administering an anti-inflammatory treatment should reduce the number of SWI hypointensities observed. The anti-inflammatory agent selected was the glucocorticoid dexamethasone.

6.1.1 Dexamethasone

Dexamethasone (dex) is a glucocorticoid that is used as a therapy in MS patients during relapses (Tremlett et al., 1998). Dex has been shown to be effective in models of EAE as well. In an MBP Lewis rat model of EAE, daily treatment with dex was shown to suppress neurological signs of EAE (Nguyen et al., 1997). In that study, dex was shown to

increase apoptosis of T cells, macrophages and microglia (Nguyen et al., 1997). The immunosuppressive effects of glucocorticoids like dex appears to relate to the synthesis of inhibitor of nuclear factor kappa-light-chain-enhancer of activated B cells (IκBα) which is an inhibitory protein that prevents nuclear translocation of NF-κB (Auphan et al., 1995; Scheinman et al., 1995).

Another study used dex in C57BL/6 mice with EAE, finding that administering dex in various paradigms (in a preventative setting vs. a therapeutic setting) was effective in reducing the EAE clinical score (Wust et al., 2008). Dex was effective at various doses ranging from 0.8 mg/kg up to 100 mg/kg. That study found that the therapeutic effects of dex resulted from apoptosis and down-regulation of cell adhesion molecules in T helper 17 cells found in periphery; however, apoptosis of T cells was not observed in the spinal cord (Wust et al., 2008). Dex and other glucocorticoids have also been shown to downregulate cell adhesion molecules on T cells (Wust et al., 2008), which impairs the ability of T cells to extravasate through the BBB to enter the CNS parenchyma.

6.2 Specific methods

6.2.1 Selection of EAE mice for study

For each experiment, at least one extra mouse was immunized to help provide the greatest chance for having mice showing signs of disease by the time mice needed to be selected and assigned to a group. On day 8 post-immunization, EAE mice were weighed and scored, and the two mice closest in EAE clinical score that also weighed the least were selected for dex and vehicle. In cases where mice did not have the exact same weight, which mouse was chosen for dex alternated between the lighter mouse and the heavier one.

6.2.2 Administration of dex

Dex was administered at a daily dose of 20 mg/kg, a dose described by others previously to be effective in EAE in C57BL/6 mice for three consecutive days as a therapeutic regimen (Wust et al., 2008). For this study, dex was administered for four consecutive days (days 8-11 post-immunization). Powder was dissolved in PBS and administered at a final injection volume of 200µL. Dex was administered within a 3 hour time frame daily. EAE mice destined for vehicle were administered 200µL of PBS immediately after EAE mice were injected with dex. Injections were always carried out in this order – dex first, vehicle second.

6.2.3 MRI for vehicle-treated and dex-treated EAE mice

All EAE mice were imaged for SWI 12 days post-immunization (after treatment for four days). EAE mice receiving vehicle (n=5) or receiving Dex (n=5) were always imaged on the same day. Untreated EAE mice (n=2) were also included for MRI.

6.2.4 Statistical analysis

An independent *t*-test was used to compare EAE clinical scores between vehicle-treated and dex-treated EAE mice for each day from days 9 through 12 post-immunization. An independent *t*-test was used to compare body weights between vehicle-treated and dex-treated EAE mice for each day from days 8 through 12 post-immunization. Independent *t*-tests were used to compare the number of SWI hypointensities in the lumbar spinal cord and cerebellum between vehicle-treated and dex-treated EAE mice. Spearman's rank

correlation was used to compare EAE clinical score with the number of SWI hypointensities for the lumbar spinal cord and cerebellum separately.

6.2.5 Consistency of SWI hypointensity counting between two blinded subjects

To determine how consistent counting of hypointensities was between the two blinded researchers, correlation analysis was carried out for data acquired for the lumbar spinal cord and cerebellum separately. There was a moderate positive correlation for counting of hypointensities between the two subjects for the lumbar spinal cord which was nearing significance (r=0.547, p=0.066, Pearson's correlation). There was a significant moderate to strong positive correlation for counting of hypointensities between the two subjects for the cerebellum (r=0.664, p=0.019, Pearson's correlation). Taken together, these values indicate that counting was fairly consistent between individuals.

6.3 Results

6.3.1 EAE clinical scores and body weights for vehicle- and dex-treated EAE mice

At 8 days post-immunization, all EAE mice used for this study had an EAE clinical score of 1 (weak tail), indicating that motor disability was beginning to develop. EAE clinical scores were lower in dex-treated EAE mice than vehicle-treated EAE mice, but these differences were not significantly different for any time points studied: day 9 (p=0.603), day 10 (p=0.496), day 11 (p=0.078), day 12 (p=0.279) (**Figure 6.1a**). Untreated EAE mice had EAE clinical scores of 7 and 8 at 12 days post-immunization.

There was no significant difference in body weight between dex-treated and vehicle-treated EAE mice for any days: day 8 (p=0.956), day 9 (p=0.735), day 10 (p=0.942), day 11 (p=0.715), day 12 (p=0.706) (**Figure 6.1b**).

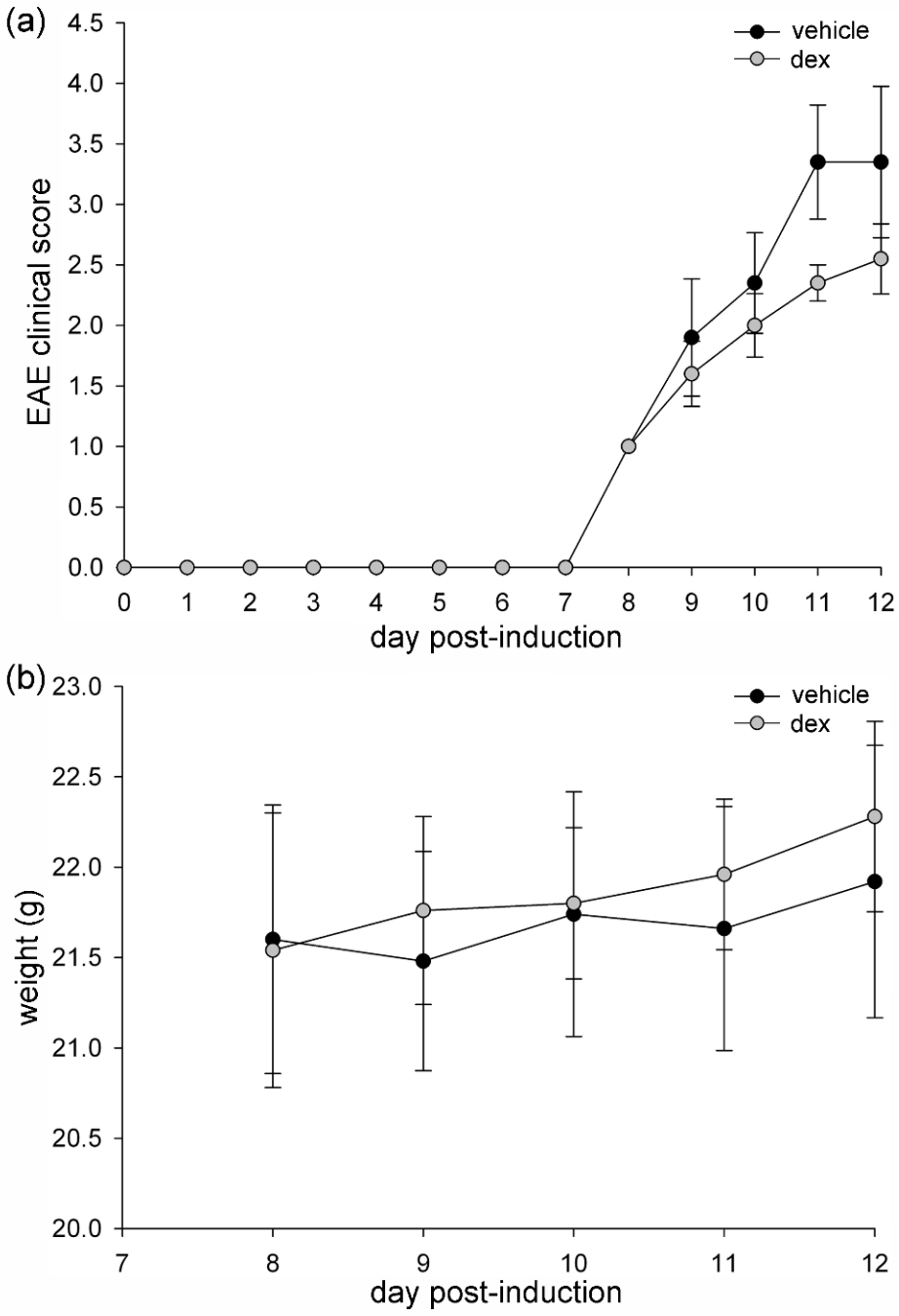
(a)
vehicle
dex
EAE clinical score
4.5
4.0
3.5
3.0
2.5
2.0
1.5
1.0
0.5
0.0
0
1
2
3
4
5
6
7
8
9
10
11
12
day post-induction
(b)
vehicle
dex
weight (g)
23.0
22.5
22.0
21.5
21.0
20.5
20.0
7
8
9
10
11
12
day post-induction

Figure 6.1 EAE clinical scores for motor disability and body weights for vehicle- and dex-treated EAE mice. (a) Scores for motor disability for vehicle- (*n*=5) and dex-treated (*n*=5) EAE mice across the EAE disease course. Values are displayed as mean ± SEM. Individual days were compared between vehicle-treated and dex-treated EAE mice using independent *t*-tests for each day; no significant differences were observed for any days post-immunization for EAE clinical score between the two groups. **(b)** Body weights for vehicle- (*n*=5) and dex-treated (*n*=5) EAE mice across the days mice were used post-immunization for treatment and MRI. Values are displayed as mean ± SEM. Individual days were compared between vehicle-treated and dex-treated EAE mice using independent *t*-tests for each day; no significant differences were observed for any days post-immunization for body weight between the two groups.

6.3.2 Appearance of SWI hypointensities in untreated, vehicle-treated and dex-treated EAE mice at 12 days post-immunization

SWI hypointensities were present in the cerebellar white matter tracts of untreated, vehicle-treated and dex-treated EAE mice. (**Figure 6.2a**). However, the hypointensities appeared darker in the untreated mice as compared to the vehicle-treated and dex-treated EAE mice. SWI hypointensities were present in the lumbar spinal cords of untreated, vehicle-treated and dex-treated EAE mice (**Figure 6.2b**). Generally, hypointensities appeared darker and more prominent in untreated EAE mice compared to vehicle-treated and dex-treated EAE mice.

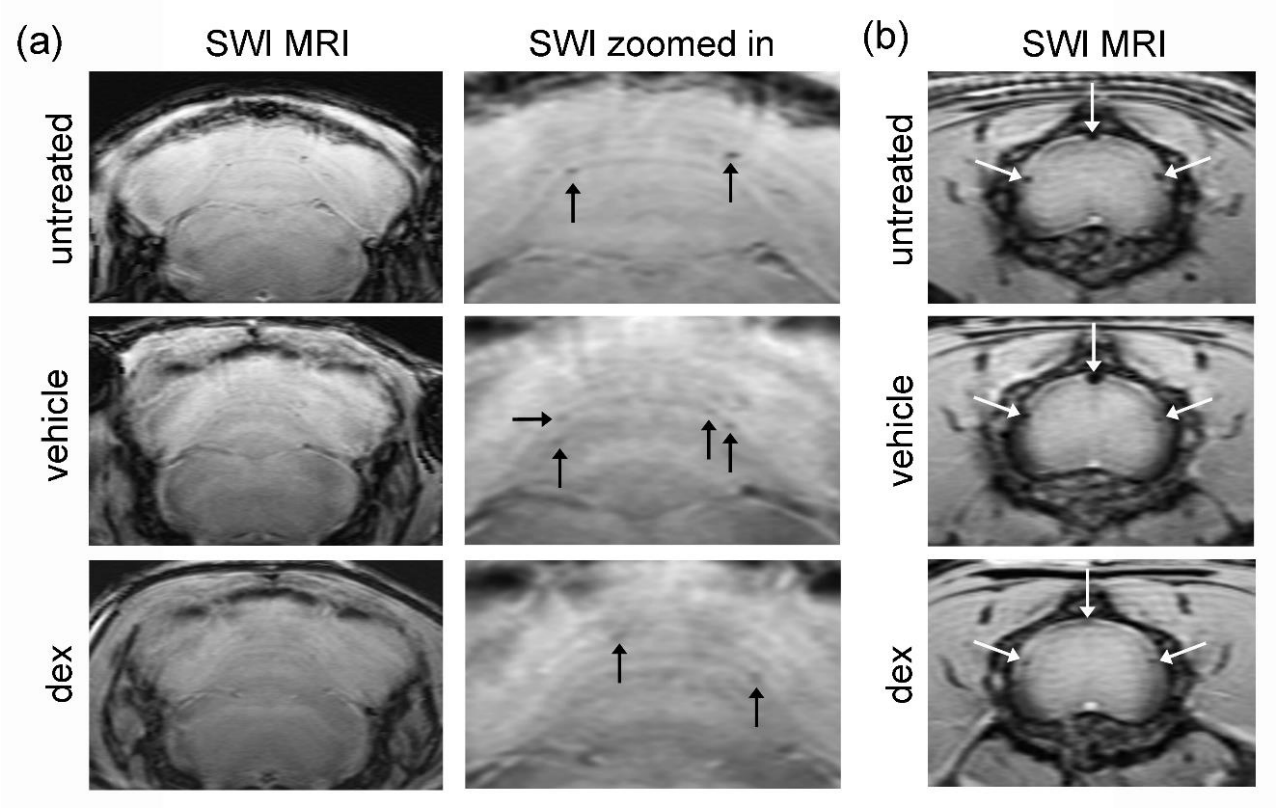

Figure 6.2 Representative SWI MRIs of the cerebella and lumbar spinal cords of untreated, vehicle-treated and dex-treated EAE mice. (a) shows SWI MRIs of the cerebella of untreated, vehicle-treated and dex-treated EAE mice. Hypointensities are seen in the white matter tracts (black arrows). Hypointensities appear most prominent in the untreated EAE mouse. **(b)** shows SWI MRIs of the lumbar spinal cords of untreated, vehicle-treated and dex-treated EAE mice. Hypointensities are seen in all three types of EAE mice (white arrows); however, the hypointensities appear less dark in the dex-treated EAE mouse.

6.3.3 Number of SWI hypointensities in vehicle-treated EAE mice vs. dex-treated EAE mice in the lumbar spinal cord and cerebellum

In the cerebellum, there was no significant difference in the number of SWI hypointensities between vehicle-treated EAE mice (1.6 ± 0.8) and dex-treated EAE mice (1.4 ± 0.5) (p=0.842, independent t-test) (**Figure 6.3**). Although not included in statistical analysis, the number of hypointensities in untreated EAE mice was also obtained; both untreated EAE mice had 3.5 SWI hypointensities in the cerebellum. In the lumbar spinal cord, there was also no significant difference in the number of SWI hypointensities between vehicle-treated EAE mice (10.4 ± 2.4, mean ± SEM) or dex-treated EAE mice (8.3 ± 0.5) (p=0.690, Mann-Whitney U test) (**Figure 6.3**). Although not included in statistical analysis, the number of hypointensities in untreated EAE mice was also obtained which had an average of 10.8 ± 0.8 SWI hypointensities in the lumbar spinal cord.

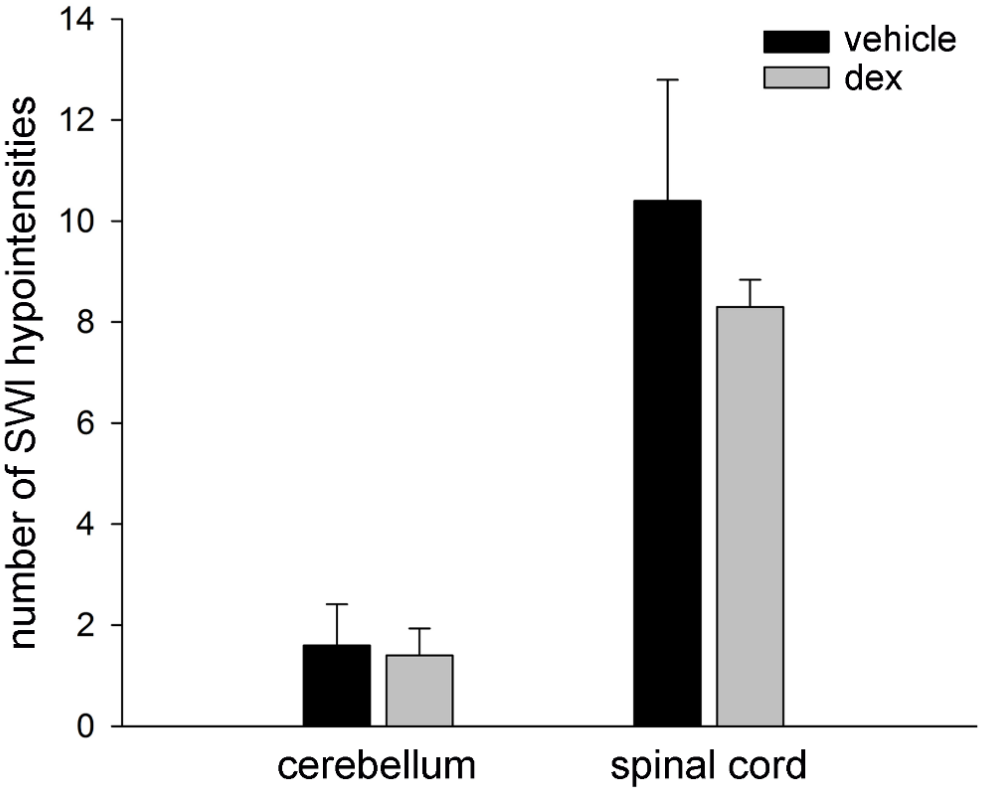

Figure 6.3 Comparison of number of SWI hypointensities between vehicle-treated and dex-treated EAE mice for the cerebellum and lumbar spinal cord. There was no significant difference between vehicle-treated (*n*=5) and dex-treated EAE mice (*n*=5) for the cerebellum and lumbar spinal cord. Comparisons were made using an independent *t*-test for the cerebellum and a Mann-Whitney U test for the lumbar spinal cord.

6.3.4 Comparison of EAE clinical score with number of SWI hypointensities in the lumbar spinal cord and cerebellum of vehicle-treated and dex-treated EAE mice

EAE clinical score (for motor disability) was compared to the number of SWI hypointensities using the vehicle- and dex-treated EAE data which was pooled together for this analysis. No significant relationship was observed between EAE clinical score and number of SWI hypointensities in the lumbar spinal cord (ρ=0.000, p=1.000, Spearman's rank correlation) (**Figure 6.4a**) nor in the cerebellum (ρ=0.099, p=0.759, Spearman's rank correlation) (**Figure 6.4b**).

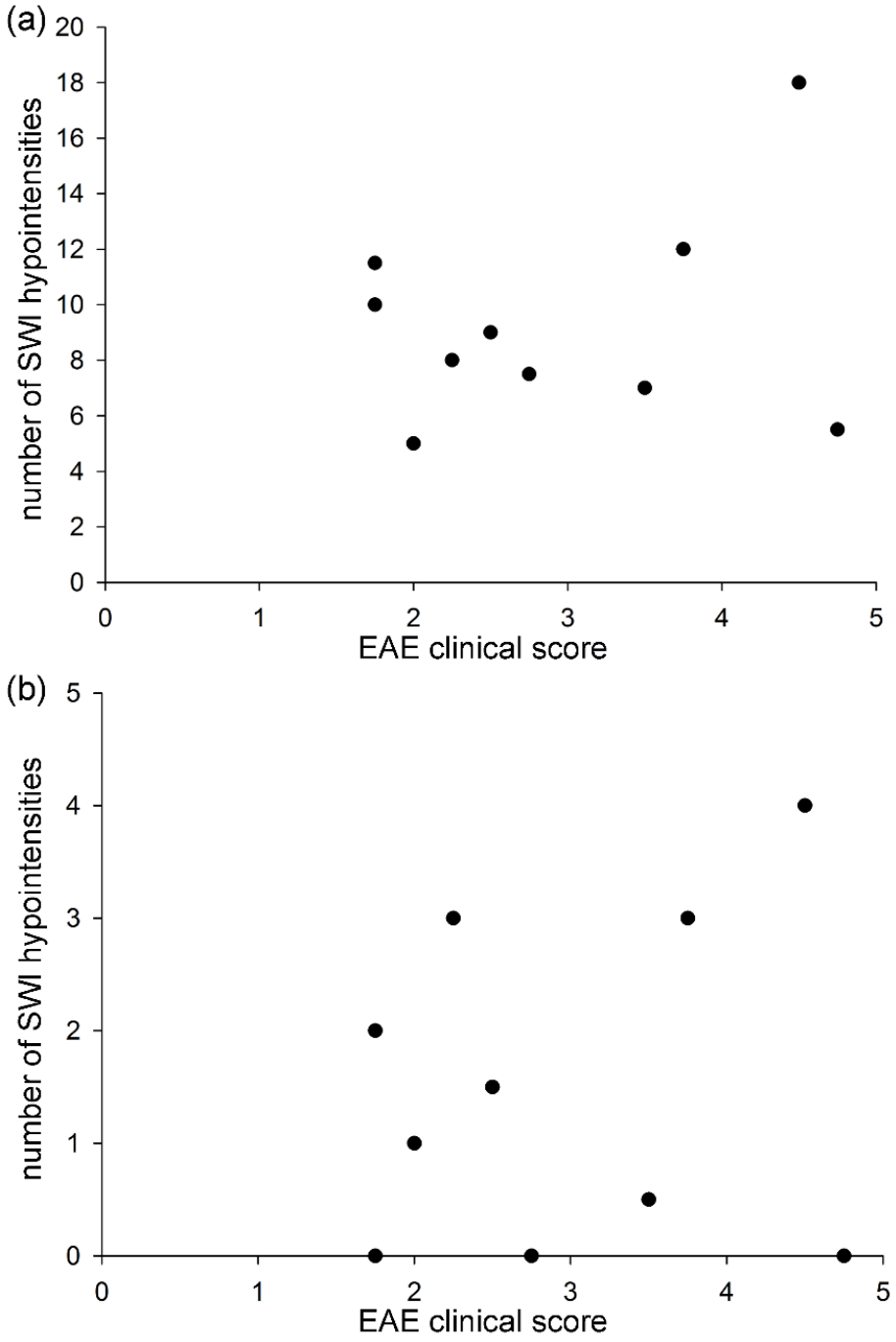
(a)
number of SWI hypointensities
EAE clinical score
(b)
number of SWI hypointensities
EAE clinical score

Figure 6.4 Comparison of EAE clinical score for motor disability with number of SWI hypointensities in lumbar spinal cord and cerebellum of EAE mice. (a) shows the comparison between EAE clinical scores and the number of SWI hypointensities for the lumbar spinal cord; there is no correlation between the two variables (ρ=0.000, p=1.000, Spearman's rank correlation). **(b)** shows the comparison between EAE clinical scores and the number of SWI hypointensities for the cerebellum; again, there is no correlation between the two variables (ρ=0.099, p=0.759, Spearman's rank correlation). The correlation between EAE clinical score and the number of SWI hypointensities was carried out using Spearman's rank correlation for both the lumbar spinal cord and cerebellum.

6.4 Discussion

In this pilot study, EAE mice were treated with either vehicle or dex for four consecutive days after onset of motor disability, but before mice were very physically disabled, corresponding to days 8 through 11 post-immunization; EAE mice from both groups underwent SWI on day 12. No significant differences were observed between the two treatment groups for EAE clinical score at any day comparisons were made (days 9 through 12). However, the difference between groups was nearing significance at the day 11 time point ($p=0.078$). Even so, it would be expected that such a high dose of dex would lead to a dramatic decrease in EAE clinical score, as has been shown to be the case by others using the same dose of dex as we did (20 mg/kg) (Wust et al., 2008).

Although there was no statistically significant difference between vehicle-treated and dex-treated EAE mice with respect to the number of SWI hypointensities in the cerebellum or lumbar spinal cord, dex-treated EAE mice did have lower numbers of SWI hypointensities in both the lumbar spinal cord and cerebellum. The high variability in the number of SWI hypointensities in the lumbar spinal cord of vehicle-treated EAE mice likely contributed to not finding significant differences between groups. Having a greater number of mice would likely make the number of SWI hypointensities significantly different between groups, with dex-treated EAE mice having lower numbers than vehicle-treated EAE mice in the lumbar spinal cord.

It should be noted that there were obvious differences in EAE clinical score between untreated EAE mice and vehicle- treated/dex-treated EAE mice at 12 days post-immunization – the average EAE clinical score for untreated mice was 7.5 as compared to 3.35 for vehicle-treated mice and 2.55 for dex-treated mice. Mice being treated (whether

with vehicle or dex) were receiving an i.p. injection everyday which would be considered a stressor. As mice were exposed to a stressor lasting less than one hour and for less than five days, the stressor would be considered to be in the category of repeated acute stressors (Heesen et al., 2007). The stress associated with the injection likely contributed to the development of EAE and subsequent motor disability; there may also have been an effect on the number of SWI hypointensities observed.

Further to this point, at least one extra animal was immunized for EAE in every experiment. The extra animal(s) not used for this study had a lower EAE clinical score and weighed more than the mice used for the study at the day 8 time point when animals were being selected for the study. By the day 12 time point, it was noted that the mouse not included in the study frequently had a higher EAE clinical score (and therefore, greater motor disability) than the EAE mice used for the study. This supports the notion that the stress of receiving a daily injection may have played a significant role in the observed reduced response to dex with respect to EAE clinical score.

The effects of stress in EAE models have been reviewed by others (Heesen et al., 2007). One of the key points made by that review was that the effects of stress on the development of EAE depends on various factors including the species (mouse vs. rat), the timing and duration of the stressor and the specific EAE model chosen (Heesen et al., 2007). Thus, altering any one of these variables may affect the EAE disease course, which provides an avenue for pursuing a future study using dex in EAE with SWI in future with an altered treatment paradigm which may lead to a more favorable outcome, both with respect to EAE clinical scores and SWI hypointensities. This pilot study supports pursuing future studies with Dex in EAE mice using SWI as a surrogate marker of inflammation.

Chapter Seven: General Discussion

7.1 Introduction

This thesis sought to characterize SWI pathology in the CNS of the EAE model, as there was no literature on any studies carried out using susceptibility MRI in any of the animal models of MS at the time this work was initiated (September 2010). This chapter will review novel findings, discuss limitations of this work and will consider the significance of our findings for the clinical setting.

7.2 Novel findings and discussion

First, we were able to demonstrate that SWI detects lesions (or hypointensities) in the CNS of EAE mice that are regionally specific. Hypointensities were localized to the white matter tracts in the cerebellum. In the lumbar spinal cord, hypointensities were seen in the grey/white matter boundary of the spinal cord, the pia mater, and in the ventral white matter. The location of hypointensities in the cerebellum coincided with regions with perivascular cuffs, but the same phenomenon was not seen in the lumbar spinal cord. With the regional variation seen between the lumbar spinal cord and cerebellum, it would be worthwhile to use SWI in other CNS regions in the EAE model, such as the cortex.

In addition to determining where SWI hypointensities are present, we also discovered that many hypointensities observed were due to intravascular deoxyhemoglobin. This was uncovered by applying a novel imaging paradigm where mice were imaged *in vivo*, perfused to remove blood, and then put back in the MRI where the scan conducted *in vivo* was repeated. This method enabled for directly comparing the two

sets of data, and could be used for future studies aiming to assess the contribution of deoxyhemoglobin to MR signal changes.

Although the majority of hypointensities were due to intravascular deoxyhemoglobin, we found that a small number were due to parenchymal iron deposition and demyelination which was confirmed with histopathology. This was the first time susceptibility MRI signal changes were correlated with histopathology for iron in the EAE model. This was also the second study to correlate MRI with iron histochemistry in the EAE model, with the first being a study that used a cerebral EAE model with T_2-weighted MRI and iron histochemistry (Williams et al., 2011). In contrast, we used a standard EAE model and our MRI results were correlated with iron histochemistry in the lumbar spinal cord and cerebellum – regions which were not covered by the Williams et al. study. Aside from our study and a recent study by Schuh et al. (Schuh et al., 2014), the only other studies that have shown iron deposition in the EAE model with histopathology are those published by Steven LeVine's group (Forge et al., 1998; Williams et al., 2011; Sands et al., 2014).

To build on our work and to make it more applicable to the clinical setting, we established a method to identify SWI hypointensities due to intravascular deoxyhemoglobin *in vivo* by increasing the inspired oxygen concentration. Imaging mice with 30% O_2 followed by 100% O_2 enabled us to discern which hypointensities were deoxyhemoglobin-based, as those were the ones that were hypointense with 30% O_2 changed in appearance with hyperoxygenation. We were also able to confirm that hypointensities which changed in appearance with hyperoxygenation were due to deoxyhemoglobin by imaging some mice after perfusion. This method could be used

clinically to help identify MR signal changes due to deoxyhemoglobin in MS patients. Hyperoxygenation has been used in combination with SWI in healthy humans to alter the appearance of deoxyhemoglobin in the venous vasculature (Rauscher et al., 2005), but not in MS patients.

Although susceptibility MRI has been used to study the venous vasculature in MS patients (Ge et al., 2009; Zivadinov et al., 2011), these studies were cross-sectional in nature. This thesis addressed how the venous vasculature changes over the EAE disease course – an area that has not been investigated by others. We found that hypointensities corresponding to veins were more prominent (as compared to baseline) in many EAE mice even before any signs of motor disability were present. Furthermore, we found that hypointensities evolved in appearance over the disease course, and the way in which hypointensities evolved was different for each mouse. Another key observation made as part of this study was the fact that the maximum number of SWI hypointensities always preceded the time point of maximum motor disability.

In addition, mice kept until they developed long-term or chronic disease generally had lower numbers of hypointensities as compared to baseline. This is interesting because, in contrast to our results, human literature has shown that the visibility of the venous vasculature is reduced in MS patients compared to controls, but these studies looked at RRMS patients (Ge et al., 2009; Zivadinov et al., 2011) and SPMS patients (Zivadinov et al., 2011). In one study, patients had an average disease duration of 5.6 years (Ge et al., 2009), while another study did not state the average disease duration of their MS patients (Zivadinov et al., 2011). By the time MS patients are diagnosed as having clinically definite MS, they have already had MS for a while because the diagnostic criteria requires

more than one MRI, if the 2005 McDonald criteria are applied (Polman et al., 2005). Thus, although EAE is not MS, it would be of interest for human MS studies to look earlier in the MS disease course (possibly in CIS or very early RRMS) to see if the venous vasculature visibility is indeed reduced then too, or if it is increased, as we see in our EAE mice. Another possibility is that the effect of reduced visibility of the venous vasculature is regionally specific – our studies looked in the lumbar spinal cord, whereas the human MS studies focused on the brain.

While our studies have shown that SWI lesions exist, why these lesions are present is unknown. In particular, the presence of elevated deoxyhemoglobin content is intriguing. One possibility for the increase in deoxyhemoglobin is venous hypoxia. This could be caused by an increase in metabolic rate due to the presence of inflammatory cells which require oxygen, but where blood flow/perfusion cannot keep up with the demand for oxygen. This would be suggestive of altered neurovascular coupling, which is defined as the coupling of blood flow to neuronal activity (Leybaert, 2005). Another possibility for increased deoxyhemoglobin content would be that metabolic rate decreases, leading to reduced blood flow and increased OEF; this assumes normal neurovascular coupling. In either instance, deoxyhemoglobin content would be elevated.

Possible reasons for iron deposition include degenerating oligodendrocytes and myelin, infiltrating immune cells, release of heme from vascular hemorrhage, and/or dysregulation of iron transport and/or regulatory proteins, or other pathologies. Previous studies in the EAE model have found areas of iron deposition to be co-localized with staining for macrophages/microglia (Forge et al., 1998; Williams et al., 2011) and astrocytes (Forge et al., 1998). It would be logical for degenerating myelin sheaths to be a

source of iron accumulation in macrophages/microglia. This is supported by the fact that in all areas where we observed iron deposition, demyelination was also present. Currently, little to no work has been done investigating other possibilities for iron accumulation in the EAE model. However, a recent study found that gene levels of ceruloplasmin, a ferroxidase which converts ferrous iron to ferric iron and promotes efflux of iron from astrocytes, was upregulated in the spinal cords of EAE mice (Gresle et al., 2014). They also found that ceruloplasmin knockout mice immunized for EAE had a slower disease evolution compared to wild-type mice immunized for EAE (Gresle et al., 2014). However, interestingly, CNS iron levels measured using mass spectrometry did not reveal an increase in spinal cord iron levels (Gresle et al., 2014), suggesting that there is a redistribution of iron rather than an overall elevation in iron content. With the studies conducted to date, it is clear that the possible reasons why there are alterations in iron content and deoxyhemoglobin require further investigation.

Taken together, the findings from this thesis have provided a foundation for pursuing future studies with susceptibility MRI in the most commonly used animal model of MS, EAE, particularly for studying the interaction between chronic inflammation and its effects on the venous vasculature.

7.3 Limitations

One of the main limitations of this work is the fact that although the EAE model shares many similarities with MS, it has a number of shortcomings and ultimately does not mimic MS accurately. Thus, the transferability of our results to the clinical realm needs to be considered. However, EAE has provided significant knowledge that has been translated

to MS, particularly when it comes to immunology of the condition. There are also a number of similarities between EAE and MS with respect to MRI phenotypes (as discussed in the Introduction), which was why this model was chosen to be investigated with SWI for this thesis.

Another limitation of this study was that we did not investigate regions that are known to have iron deposition in MS – particularly the deep grey matter structures. The deep grey matter has been investigated extensively in MS patients with susceptibility MRI (see Introduction), and in some cases, MRI data has been correlated with another measure of iron (Walsh et al., 2013; Zheng et al., 2013). In contrast, a recent study found that within lesions in EAE animals, there is little to no iron accumulation, depending on the specific EAE model studied (Schuh et al., 2014). However, significant iron accumulation was observed in the basal ganglia in old control animals compared to young control animals; the iron that accumulated in aged rats was seen in oligodendrocytes and myelin, which is also seen in humans (Schuh et al., 2014). For the EAE model used in this thesis, MOG_{35-55}, tissue was only sampled at the 21, 27 and 35 day time points in the Schuh et al. study. It is possible that sampling earlier (days 15-19) would have uncovered more iron deposition in lesions, as this is the time point at which we observed white matter lesions with iron deposition. It is also worth noting that in the Schuh et al. study only ferrous iron was studied, whereas it is usually ferric iron that is investigated in human MS studies. With limited work done in iron deposition in EAE, it would be worth having more studies in this area, and further investigating iron deposition in the basal ganglia in the EAE model. On the other hand, it would be beneficial to use susceptibility MRI in MS patients to look at iron deposition in the spinal cord and cerebellum – regions investigated in this thesis.

Another obvious limitation in this work is the use of a single MRI method, SWI. Our SWI results were not correlated with any other MRI method. The reason for this was mainly due to feasibility – the SWI acquisitions are lengthy (over one hour for the lumbar spinal cord for one animal). It would be worthwhile combining SWI with another method to better understand the pathology being detected in the EAE model. One could use a multi-echo gradient echo sequence by which R_2* and SWI could be obtained as R_2* provides complementary information to phase (Yao et al., 2012) (**Figure 7.1**). However, this would limit the number of slices and the study would be challenging to carry out, as the location of lesions in the EAE mouse spinal cord is highly unpredictable. Another possibility would be to include an MRI method used in MS patients, such as T_2-weighted MRI or Gd-enhanced MRI, to compare with SWI. However, Gd-enhanced MRI has not been effective at detecting lesions in all EAE models (Nathoo et al., 2014a).

There are also limitations related to the EAE scoring paradigm and the relationship between the EAE clinical score and the number of SWI hypointensities. One obvious limitation is that EAE scoring was not blinded, which is something that could be improved on for future studies. Another issue is the lack of correlation between the number of SWI hypointensities and the EAE clinical score. One of the pitfalls of the EAE clinical score is that it is purely based on motor function, and so any sensory changes or cognitive changes are not addressed by using this metric. It is also worth noting that many of the SWI MRI changes (with respect to hypointensities) take place before onset of motor disability. Therefore, different behavioral tests would likely need to be used instead of relying on the EAE clinical score as a correlate for SWI hypointensities. Possible behavioral tests include tests for changes in social behavior or anxiety. Anxiety and depression-like behaviors have

been reported in EAE mice prior to the onset of motor disability (Acharjee et al., 2013) – this is a possible avenue of exploration as a correlate for SWI hypointensities.

Another significant limitation is the inherent difficulty in imaging such small lesions in a mouse; this is particularly important, as we detected very few white matter lesions when we know that there are many which can be visualized using histology. This is a limitation that will be challenging to overcome, as in order to potentially visualize such small lesions, voxel resolution would have to be increased at the expense of signal (SNR) in order to keep imaging time within a reasonable range.

Change in Tissue Content Compared with Normal Tissue	Influence on R2* Signal on MR Images	Influence on Phase Signal on MR Images
Iron increase	Increase	Negative shift (paramagnetic shift)
Iron decrease	Decrease	Positive shift (diamagnetic shift)
Myelin increase	Increase	Positive shift (diamagnetic shift)
Myelin decrease	Decrease	Negative shift (paramagnetic shift)

Figure 7.1 Effects of iron and myelin on R_2* and phase MRI. As iron increases, R_2* increases (becomes hyperintense) while there is a negative phase shift (becomes hypointense). However, as myelin increases, R_2* increases (becomes hyperintense) while phase has a positive phase shift. Thus, obtaining both R_2* and phase information may help distinguish between regions with demyelination and no iron deposition and demyelination with iron deposition.

Adapted from (Yao et al., 2012)

7.4 Significance of findings for the clinical setting

Although EAE is not MS, findings from this thesis have clinical implications. The most obvious is that more care needs to be taken when interpreting SWI or other susceptibility MR images for a link to pathology, as some MR signal changes may be due to deoxyhemoglobin rather than iron deposition. Demyelination is also a major contributing factor to such MR signal changes. Recent work being done on MS patients using modeling with SWI suggests that only a small proportion of lesions (4%) had features on MRI that would be suggestive of iron deposition (Wiggermann et al., 2014).

In order to truly confirm the source of lesions, histopathology needs to be carried out alongside MRI which has only been done in a few studies (Bagnato et al., 2011; Yao et al., 2012) – this is understandable considering the difficulty in obtaining MS tissue post-mortem. Thus, that the EAE model also shows some pathology similar to that in MS (as shown in this thesis), particularly the presence of a minority of SWI lesions that are due to iron deposition (which has been confirmed with histopathology), may provide an avenue to further investigate such lesions. That a significant proportion of SWI hypointensities in the EAE model are due to deoxyhemoglobin also warrants further investigation in the clinical setting in MS patients, as it is likely that these deoxyhemoglobin-based hypointensities are related to chronic inflammation which is prevalent in both EAE and in MS. Furthermore, our observations of dynamic venous alterations throughout the EAE disease course may also be a factor in MS patients – an area that has not been explored yet. Thus, knowledge created from this thesis may help guide future studies in MS patients that can help establish susceptibility MRI as a method for investigating diverse pathology in MS. Ultimately, this work has helped deepen understanding of EAE and the value of SWI in this animal model.

Chapter Eight: Future Directions and Conclusions

8.1 Future Directions

8.1.1 General

To build on work done in this thesis, multiple future studies could be conducted. With the interesting preliminary data obtained on pimonidazole staining and hematoxylin & eosin staining in animals that underwent SWI (presented in Chapter 5), it would be worth carrying out a more in-depth study to investigate the relationship between venous alterations (seen with SWI) and tissue hypoxia (seen with pimonidazole staining) and inflammation (seen with hematoxylin & eosin staining). More specifically, EAE mice could undergo SWI followed by pimonidazole and hematoxylin & eosin staining at baseline, before onset of motor dysfunction, at onset of motor dysfunction, at peak disease and at long-term disease. This would be worth carrying out as the only study carried out doing pimonidazole staining over the EAE disease course found pimonidazole staining only at time points at which animals had motor disability (Davies et al., 2013), while our preliminary results suggest otherwise (see Chapter 5).

Another way of measuring tissue hypoxia would be to implant a pO_2 probe whereby tissue oxygen could be measured regularly and could be supplemented with SWI data. Although repeated measurements would not be feasible in the lumbar spinal cord, they could be carried out in another region investigated in this thesis, the cerebellum. Currently, work is being done by others in our lab to use pO_2 probes in the cerebellum of EAE mice. Regardless of the method, being able to correlate what we believe to be venous hypoxia with tissue hypoxia could add substantially to our understanding of the relationship between chronic inflammation and hypoxia, with possible translation to MS.

Another possible area for investigation to follow up on work done in this thesis would be to carry out susceptibility MRI in MS patients while breathing room air followed by breathing 100% O_2. This could help determine the contribution of deoxyhemoglobin to hypointense signals seen in susceptibility MRI in MS patients, and it could provide a means to differentiate between parenchymal iron deposition and deoxyhemoglobin-based hypointensities.

It would also be worthwhile to incorporate other advanced MRI methods to compare with SWI in the EAE model; methods to consider would include myelin water imaging, MTR, and perfusion MRI.

8.1.2 Dexamethasone study

With the insignificant results obtained in the dex study, it would be worth altering some components of the study. To mitigate stress on the animals, starting saline injections from the day of immunization for EAE (or even before that), so that animals get used to being injected, would be worthwhile. The time point at which dex is administered could also be changed – in our study we had administered dex at a dose of 20 mg/kg from days 8 through 11 post-immunization with imaging taking place on day 12. However, as hypointensities were found to be quite prominent in a number of EAE mice by the 7 day time point (as described in Chapter 5), it would be worthwhile to administer dex earlier and to image instead at the 7 day time point. This would also enable us to incorporate behavior tests that are not motor-driven, and that may correlate better with the number of SWI hypointensities observed. It is also possible that it is not the number of SWI hypointensities that correlates with behavioral changes, but rather the signal intensity of SWI

hypointensities – this could be incorporated as another quantitative measure alongside counting the number of SWI hypointensities.

Changing the time point at which animals undergo imaging, as described in the above paragraph, could also be supplemented by imaging at baseline (as was done in Chapter 5 for the time-course study). This way, ratios could be obtained rather than having to compare absolute numbers of SWI hypointensities which may vary at baseline between animals. The ideal experimental paradigm would involve imaging animals at baseline (before EAE immunization), administering dex for three days (e.g. days 4-6 post immunization), and then re-imaging animals at 7 days post-immunization.

The dose of dex used could also potentially be altered. Our decision to use a higher dose of dex was due to the goal of reducing inflammation substantially so that there would be an obvious and significant effect on SWI hypointensities. However, if the goal is to have this work be clinically relevant, it would be worth including other doses of dex as well. The dose of dex used in other inflammatory models ranges from 0.5 mg/kg in a model of post-traumatic osteoarthritis (Huebner et al., 2014) to 3.0 mg/kg in a model of brain inflammation induced by carrageenan (Gamache and Ellis, 1986). In EAE studies, dex has been effective in MOG_{35-55} induced EAE at doses as low as 0.3 mg/kg (Donia et al., 2010) and 0.8 mg/kg (Wust et al., 2008). In the Wust et al. study, dex was administered on days 9-11 post-immunization which was effective at reducing motor disability in EAE mice. Neither of the studies using dex in MOG_{35-55} EAE mentioned injecting animals before the days post-immunization selected, and so it is not known why our use of a similar paradigm did not reduce motor disability significantly in our study. As mentioned above, mitigating stress may help although this did not appear to be an issue in previous studies

using dex in EAE (Wust et al., 2008; Donia et al., 2010). It is worth mentioning that in humans, high dose dexamethasone is considered to be 40 mg per day which translates to 0.67 mg/kg for a 60 kg person. Thus, our dose for the dex study is far from clinically relevant, but again, the goal of using such a high dose was to effectively eliminate inflammation.

Another possible direction to take the work of trying to determine whether SWI can assess the effect of a treatment would be to use a different anti-inflammatory drug. One obvious option would have been to use anti-VLA-4, but this has been shown to be ineffective and can induce mortality in MOG_{35-55} EAE mice, suggested to be due to its interaction with PTX (Kerfoot et al., 2006; Ji et al., 2011). Another possibility would be to use anti-CD4 to deplete CD4+ T cells, ultimately reducing inflammation. Anti-CD4 has been used in EAE models before, where it has prevented EAE onset in the vast majority of mice studied (Biasi et al., 1997; Montero et al., 2004).

8.2 Conclusions

In summary, we have characterized the SWI phenotype in a mouse EAE model. Our results highlight the different sources for hypointensities detected with SWI (iron deposition and demyelination vs. intravascular deoxyhemoglobin), and emphasize the dynamic changes that take place in the venous vasculature over the EAE disease course which may be linked to venous hypoxia. This thesis underlines the potential for susceptibility MRI methods like SWI to be used to further investigate the relationship between chronic inflammation and changes to the venous vasculature, both in MS and in other chronic inflammatory conditions.

References

(2008). Atlas : multiple sclerosis resources in the world 2008 Geneva, World Health Organization**:** 56.

Aboul-Enein, F., H. Rauschka, B. Kornek, C. Stadelmann, A. Stefferl, W. Bruck, C. Lucchinetti, M. Schmidbauer, K. Jellinger and H. Lassmann (2003). Preferential loss of myelin-associated glycoprotein reflects hypoxia-like white matter damage in stroke and inflammatory brain diseases. J Neuropathol Exp Neurol 62(1): 25-33.

Acharjee, S., N. Nayani, M. Tsutsui, M. N. Hill, S. S. Ousman and Q. J. Pittman (2013). Altered cognitive-emotional behavior in early experimental autoimmune encephalitis--cytokine and hormonal correlates. Brain Behav Immun 33: 164-172.

Adams, C. W. (1988). Perivascular iron deposition and other vascular damage in multiple sclerosis. J Neurol Neurosurg Psychiatry 51(2): 260-265.

Adams, R. D. and C. S. Kubik (1952). The morbid anatomy of the demyelinative disease. Am J Med 12(5): 510-546.

Adhya, S., G. Johnson, J. Herbert, H. Jaggi, J. S. Babb, R. I. Grossman and M. Inglese (2006). Pattern of hemodynamic impairment in multiple sclerosis: dynamic susceptibility contrast perfusion MR imaging at 3.0 T. Neuroimage 33(4): 1029-1035.

Agrawal, S., P. Anderson, M. Durbeej, N. van Rooijen, F. Ivars, G. Opdenakker and L. M. Sorokin (2006). Dystroglycan is selectively cleaved at the parenchymal basement membrane at sites of leukocyte extravasation in experimental autoimmune encephalomyelitis. J Exp Med 203(4): 1007-1019.

Agrawal, S. M., C. Silva, W. W. Tourtellotte and V. W. Yong (2011). EMMPRIN: a novel regulator of leukocyte transmigration into the CNS in multiple sclerosis and experimental autoimmune encephalomyelitis. J Neurosci 31(2): 669-677.

Agrawal, S. M., J. Williamson, R. Sharma, H. Kebir, K. Patel, A. Prat and V. W. Yong (2013). Extracellular matrix metalloproteinase inducer shows active perivascular cuffs in multiple sclerosis. Brain 136(Pt 6): 1760-1777.

Aharoni, R., E. Sasson, T. Blumenfeld-Katzir, R. Eilam, M. Sela, Y. Assaf and R. Arnon (2013). Magnetic resonance imaging characterization of different experimental autoimmune encephalomyelitis models and the therapeutic effect of glatiramer acetate. Exp Neurol 240C: 130-144.

Ahrens, E. T., D. H. Laidlaw, C. Readhead, C. F. Brosnan, S. E. Fraser and R. E. Jacobs (1998). MR microscopy of transgenic mice that spontaneously acquire experimental allergic encephalomyelitis. Magn Reson Med 40(1): 119-132.

Aktas, O., P. Kury, B. Kieseier and H. P. Hartung (2010). Fingolimod is a potential novel therapy for multiple sclerosis. Nat Rev Neurol 6(7): 373-382.

Al-Radaideh, A. M., S. J. Wharton, S. Y. Lim, C. R. Tench, P. S. Morgan, R. W. Bowtell, C. S. Constantinescu and P. A. Gowland (2013). Increased iron accumulation occurs in the earliest stages of demyelinating disease: an ultra-high field susceptibility mapping study in Clinically Isolated Syndrome. Mult Scler 19(7): 896-903.

Aldskogius, H. and J. Fraher (2002). Glial Interfaces in the Nervous System: Role in Repair and Plasticity, IOS Press.

Allen, N. B., J. H. Lichtman, H. W. Cohen, J. Fang, L. M. Brass and M. H. Alderman (2008). Vascular disease among hospitalized multiple sclerosis patients. Neuroepidemiology 30(4): 234-238.

Ansari, K. A., M. Wilson, G. E. Slater, J. J. Haglin and E. Kaplan (1986). Hyperbaric oxygenation and erythrocyte antioxidant enzymes in multiple sclerosis patients. Acta Neurol Scand 74(2): 156-160.

Aoki, I., Y. J. Wu, A. C. Silva, R. M. Lynch and A. P. Koretsky (2004). In vivo detection of neuroarchitecture in the rodent brain using manganese-enhanced MRI. Neuroimage 22(3): 1046-1059.

Arteel, G. E., R. G. Thurman and J. A. Raleigh (1998). Reductive metabolism of the hypoxia marker pimonidazole is regulated by oxygen tension independent of the pyridine nucleotide redox state. Eur J Biochem 253(3): 743-750.

Arteel, G. E., R. G. Thurman, J. M. Yates and J. A. Raleigh (1995). Evidence that hypoxia markers detect oxygen gradients in liver: pimonidazole and retrograde perfusion of rat liver. Br J Cancer 72(4): 889-895.

Ashkanian, M., A. Gjedde, K. Mouridsen, M. Vafaee, K. V. Hansen, L. Ostergaard and G. Andersen (2009). Carbogen inhalation increases oxygen transport to hypoperfused brain tissue in patients with occlusive carotid artery disease: increased oxygen transport to hypoperfused brain. Brain Res 1304: 90-95.

Auphan, N., J. A. DiDonato, C. Rosette, A. Helmberg and M. Karin (1995). Immunosuppression by glucocorticoids: inhibition of NF-kappa B activity through induction of I kappa B synthesis. Science 270(5234): 286-290.

Bagnato, F., S. Hametner, B. Yao, P. van Gelderen, H. Merkle, F. K. Cantor, H. Lassmann and J. H. Duyn (2011). Tracking iron in multiple sclerosis: a combined imaging and histopathological study at 7 Tesla. Brain 134(Pt 12): 3602-3615.

Baik, S. K., W. Choi, S. J. Oh, K. P. Park, M. G. Park, T. I. Yang and H. W. Jeong (2012). Change in cortical vessel signs on susceptibility-weighted images after full recanalization in hyperacute ischemic stroke. Cerebrovasc Dis 34(3): 206-212.

Baxter, A. G. (2007). The origin and application of experimental autoimmune encephalomyelitis. Nat Rev Immunol 7(11): 904-912.

Beeton, C., A. Garcia and K. G. Chandy (2007). Induction and clinical scoring of chronic-relapsing experimental autoimmune encephalomyelitis. J Vis Exp(5): 224.

Bendszus, M., G. Ladewig, L. Jestaedt, B. Misselwitz, L. Solymosi, K. Toyka and G. Stoll (2008). Gadofluorine M enhancement allows more sensitive detection of inflammatory CNS lesions than T2-w imaging: a quantitative MRI study. Brain 131(Pt 9): 2341-2352.

Biasi, G., A. Facchinetti, G. Monastra, S. Mezzalira, S. Sivieri, B. Tavolato and P. Gallo (1997). Protection from experimental autoimmune encephalomyelitis (EAE): non-depleting anti-CD4 mAb treatment induces peripheral T-cell tolerance to MBP in PL/J mice. J Neuroimmunol 73(1-2): 117-123.

Blakemore, W. F. (1973). Demyelination of the superior cerebellar peduncle in the mouse induced by cuprizone. J Neurol Sci 20(1): 63-72.

Blezer, E. L., J. Bauer, H. P. Brok, K. Nicolay and B. A. t Hart (2007). Quantitative MRI-pathology correlations of brain white matter lesions developing in a non-human primate model of multiple sclerosis. NMR Biomed 20(2): 90-103.

Boretius, S., B. Schmelting, T. Watanabe, D. Merkler, R. Tammer, B. Czeh, T. Michaelis, J. Frahm and E. Fuchs (2006). Monitoring of EAE onset and progression in the common marmoset monkey by sequential high-resolution 3D MRI. NMR Biomed 19(1): 41-49.

Boroujerdi, A., J. V. Welser-Alves and R. Milner (2013). Extensive vascular remodeling in the spinal cord of pre-symptomatic experimental autoimmune encephalomyelitis mice; increased vessel expression of fibronectin and the alpha5beta1 integrin. Exp Neurol 250: 43-51.

Bowern, N., I. A. Ramshaw, I. A. Clark and P. C. Doherty (1984). Inhibition of autoimmune neuropathological process by treatment with an iron-chelating agent. J Exp Med 160(5): 1532-1543.

Brenner, R. E., P. M. Munro, S. C. Williams, J. D. Bell, G. J. Barker, C. P. Hawkins, D. N. Landon and W. I. McDonald (1993). The proton NMR spectrum in acute EAE: the significance of the change in the Cho:Cr ratio. Magn Reson Med 29(6): 737-745.

Brochet, B., M. S. Deloire, T. Touil, O. Anne, J. M. Caille, V. Dousset and K. G. Petry (2006). Early macrophage MRI of inflammatory lesions predicts lesion severity and disease development in relapsing EAE. Neuroimage 32(1): 266-274.

Brock, J. H. and J. Stevenson (1987). Replacement of transferrin in serum-free cultures of mitogen-stimulated mouse lymphocytes by a lipophilic iron chelator. Immunol Lett 15(1): 23-25.

Brooks, D. J., K. L. Leenders, G. Head, J. Marshall, N. J. Legg and T. Jones (1984). Studies on regional cerebral oxygen utilisation and cognitive function in multiple sclerosis. J Neurol Neurosurg Psychiatry 47(11): 1182-1191.

Brown, G. C. and J. J. Neher (2010). Inflammatory neurodegeneration and mechanisms of microglial killing of neurons. Mol Neurobiol 41(2-3): 242-247.

Brown, M. A. and R. C. Semelka (2010). MRI: Basic Principles and Applications. USA, Wiley-Blackwell.

Budde, M. D., J. H. Kim, H. F. Liang, J. H. Russell, A. H. Cross and S. K. Song (2008). Axonal injury detected by in vivo diffusion tensor imaging correlates with neurological disability in a mouse model of multiple sclerosis. NMR Biomed 21(6): 589-597.

Budde, M. D., M. Xie, A. H. Cross and S. K. Song (2009). Axial diffusivity is the primary correlate of axonal injury in the experimental autoimmune encephalomyelitis spinal cord: a quantitative pixelwise analysis. J Neurosci 29(9): 2805-2813.

Buenz, E. J., B. M. Sauer, R. G. Lafrance-Corey, C. Deb, A. Denic, C. L. German and C. L. Howe (2009). Apoptosis of hippocampal pyramidal neurons is virus independent in a mouse model of acute neurovirulent picornavirus infection. Am J Pathol 175(2): 668-684.

Burgetova, A., Z. Seidl, J. Krasensky, D. Horakova and M. Vaneckova (2010). Multiple sclerosis and the accumulation of iron in the Basal Ganglia: quantitative assessment of brain iron using MRI t(2) relaxometry. Eur Neurol 63(3): 136-143.

Buxton, R. B., K. Uludag, D. J. Dubowitz and T. T. Liu (2004). Modeling the hemodynamic response to brain activation. Neuroimage 23 Suppl 1: S220-233.

Ceccarelli, A., M. A. Rocca, E. Perego, L. Moiola, A. Ghezzi, V. Martinelli, G. Comi and M. Filippi (2011). Deep grey matter T2 hypo-intensity in patients with paediatric multiple sclerosis. Mult Scler 17(6): 702-707.

Chavhan, G. B., P. S. Babyn, B. Thomas, M. M. Shroff and E. M. Haacke (2009). Principles, techniques, and applications of T2*-based MR imaging and its special applications. Radiographics 29(5): 1433-1449.

Chen, C. C., A. Zechariah, Y. H. Hsu, H. W. Chen, L. C. Yang and C. Chang (2008). Neuroaxonal ion dyshomeostasis of the normal-appearing corpus callosum in experimental autoimmune encephalomyelitis. Exp Neurol 210(2): 322-330.

Chin, C. L., M. Pai, P. F. Bousquet, A. J. Schwartz, E. M. O'Connor, C. M. Nelson, V. P. Hradil, B. F. Cox, B. L. McRae and G. B. Fox (2009). Distinct spatiotemporal pattern of CNS lesions revealed by USPIO-enhanced MRI in MOG-induced EAE rats implicates the involvement of spino-olivocerebellar pathways. J Neuroimmunol 211(1-2): 49-55.

Christiansen, C. F., S. Christensen, D. K. Farkas, M. Miret, H. T. Sorensen and L. Pedersen (2010). Risk of arterial cardiovascular diseases in patients with multiple sclerosis: a population-based cohort study. Neuroepidemiology 35(4): 267-274.

Compston, A. and A. Coles (2008). Multiple sclerosis. Lancet 372(9648): 1502-1517.

Connor, J. R. and S. L. Menzies (1996). Relationship of iron to oligodendrocytes and myelination. Glia 17(2): 83-93.

Cook, L. L., P. J. Foster and S. J. Karlik (2005). Pathology-guided MR analysis of acute and chronic experimental allergic encephalomyelitis spinal cord lesions at 1.5T. J Magn Reson Imaging 22(2): 180-188.

Craelius, W., M. W. Migdal, C. P. Luessenhop, A. Sugar and I. Mihalakis (1982). Iron deposits surrounding multiple sclerosis plaques. Arch Pathol Lab Med 106(8): 397-399.

Crichton, R. R., D. T. Dexter and R. J. Ward (2011). Brain iron metabolism and its perturbation in neurological diseases. J Neural Transm 118(3): 301-314.

Cummings, J. L. (2009). Defining and labeling disease-modifying treatments for Alzheimer's disease. Alzheimers Dement 5(5): 406-418.

Cummins, E. P., E. Berra, K. M. Comerford, A. Ginouves, K. T. Fitzgerald, F. Seeballuck, C. Godson, J. E. Nielsen, P. Moynagh, J. Pouyssegur and C. T. Taylor (2006). Prolyl hydroxylase-1 negatively regulates IkappaB kinase-beta, giving insight into hypoxia-induced NFkappaB activity. Proc Natl Acad Sci U S A 103(48): 18154-18159.

D'Haeseleer, M., M. Cambron, L. Vanopdenbosch and J. De Keyser (2011). Vascular aspects of multiple sclerosis. Lancet Neurol 10(7): 657-666.

Dal Canto, M. C., B. S. Kim, S. D. Miller and R. W. Melvold (1996). Theiler's Murine Encephalomyelitis Virus (TMEV)-Induced Demyelination: A Model for Human Multiple Sclerosis. Methods 10(3): 453-461.

Dal Canto, M. C. and H. L. Lipton (1975). Primary demyelination in Theiler's virus infection. An ultrastructural study. Lab Invest 33(6): 626-637.

Davies, A. L., R. A. Desai, P. S. Bloomfield, P. R. McIntosh, K. J. Chapple, C. Linington, R. Fairless, R. Diem, M. Kasti, M. P. Murphy and K. J. Smith (2013). Neurological deficits caused by tissue hypoxia in neuroinflammatory disease. Ann Neurol 74(6): 815-825.

DeBoy, C. A., J. Zhang, S. Dike, I. Shats, M. Jones, D. S. Reich, S. Mori, T. Nguyen, B. Rothstein, R. H. Miller, J. T. Griffin, D. A. Kerr and P. A. Calabresi (2007). High resolution diffusion tensor imaging of axonal damage in focal inflammatory and demyelinating lesions in rat spinal cord. Brain 130(Pt 8): 2199-2210.

Deloire-Grassin, M. S., B. Brochet, B. Quesson, C. Delalande, V. Dousset, P. Canioni and K. G. Petry (2000). In vivo evaluation of remyelination in rat brain by magnetization transfer imaging. J Neurol Sci 178(1): 10-16.

Deloire, M. S., T. Touil, B. Brochet, V. Dousset, J. M. Caille and K. G. Petry (2004). Macrophage brain infiltration in experimental autoimmune encephalomyelitis is not completely compromised by suppressed T-cell invasion: in vivo magnetic resonance imaging illustration in effective anti-VLA-4 antibody treatment. Mult Scler 10(5): 540-548.

Denic, A., A. J. Johnson, A. J. Bieber, A. E. Warrington, M. Rodriguez and I. Pirko (2011). The relevance of animal models in multiple sclerosis research. Pathophysiology 18(1): 21-29.

Donia, M., K. Mangano, C. Quattrocchi, P. Fagone, S. Signorelli, G. Magro, A. Sfacteria, K. Bendtzen and F. Nicoletti (2010). Specific and strain-independent effects of dexamethasone in the prevention and treatment of experimental autoimmune encephalomyelitis in rodents. Scand J Immunol 72(5): 396-407.

Dousset, V., L. Ballarino, C. Delalande, M. Coussemacq, P. Canioni, K. G. Petry and J. M. Caille (1999). Comparison of ultrasmall particles of iron oxide (USPIO)-enhanced T2-weighted, conventional T2-weighted, and gadolinium-enhanced T1-weighted MR images in rats with experimental autoimmune encephalomyelitis. AJNR Am J Neuroradiol 20(2): 223-227.

Dousset, V., B. Brochet, M. S. Deloire, L. Lagoarde, B. Barroso, J. M. Caille and K. G. Petry (2006). MR imaging of relapsing multiple sclerosis patients using ultra-small-particle iron oxide and compared with gadolinium. AJNR Am J Neuroradiol 27(5): 1000-1005.

Dousset, V., B. Brochet, A. Vital, C. Gross, A. Benazzouz, A. Boullerne, A. M. Bidabe, A. M. Gin and J. M. Caille (1995). Lysolecithin-induced demyelination in primates: preliminary in vivo study with MR and magnetization transfer. AJNR Am J Neuroradiol 16(2): 225-231.

Dragatsis, I., A. Efstratiadis and S. Zeitlin (1998). Mouse mutant embryos lacking huntingtin are rescued from lethality by wild-type extraembryonic tissues. Development 125(8): 1529-1539.

Drayer, B., P. Burger, B. Hurwitz, D. Dawson and J. Cain (1987). Reduced signal intensity on MR images of thalamus and putamen in multiple sclerosis: increased iron content? AJR Am J Roentgenol 149(2): 357-363.

Dunn, J. F., M. A. Roche, R. Springett, M. Abajian, J. Merlis, C. P. Daghlian, S. Y. Lu and M. Makki (2004). Monitoring angiogenesis in brain using steady-state quantification of DeltaR2 with MION infusion. Magn Reson Med 51(1): 55-61.

Dunn, J. F., U. I. Tuor, J. Kmech, N. A. Young, A. K. Henderson, J. C. Jackson, P. A. Valentine and G. C. Teskey (2009). Functional brain mapping at 9.4T using a new MRI-compatible electrode chronically implanted in rats. Magn Reson Med 61(1): 222-228.

Eissa, A., R. M. Lebel, J. R. Korzan, A. E. Zavodni, K. G. Warren, I. Catz, D. J. Emery and A. H. Wilman (2009). Detecting lesions in multiple sclerosis at 4.7 tesla using phase susceptibility-weighting and T2-weighting. J Magn Reson Imaging 30(4): 737-742.

Eltzschig, H. K. and P. Carmeliet (2011). Hypoxia and inflammation. N Engl J Med 364(7): 656-665.

Engberink, R. D., S. M. van der Pol, P. Walczak, A. van der Toorn, M. A. Viergever, C. D. Dijkstra, J. W. Bulte, H. E. de Vries and E. L. Blezer (2010). Magnetic resonance imaging of monocytes labeled with ultrasmall superparamagnetic particles of iron oxide using magnetoelectroporation in an animal model of multiple sclerosis. Mol Imaging 9(5): 268-277.

Filippi, M. and M. Rovaris (2000). Magnetisation transfer imaging in multiple sclerosis. J Neurovirol 6 Suppl 2: S115-120.

Fischer, B. H., M. Marks and T. Reich (1983). Hyperbaric-oxygen treatment of multiple sclerosis. A randomized, placebo-controlled, double-blind study. N Engl J Med 308(4): 181-186.

Fjaer, S., L. Bo, A. Lundervold, K. M. Myhr, T. Pavlin, O. Torkildsen and S. Wergeland (2013). Deep gray matter demyelination detected by magnetization transfer ratio in the cuprizone model. PLoS One 8(12): e84162.

Fletcher, J. M., S. J. Lalor, C. M. Sweeney, N. Tubridy and K. H. Mills (2010). T cells in multiple sclerosis and experimental autoimmune encephalomyelitis. Clin Exp Immunol 162(1): 1-11.

Floris, S., E. L. Blezer, G. Schreibelt, E. Dopp, S. M. van der Pol, I. L. Schadee-Eestermans, K. Nicolay, C. D. Dijkstra and H. E. de Vries (2004). Blood-brain barrier permeability and monocyte infiltration in experimental allergic encephalomyelitis: a quantitative MRI study. Brain 127(Pt 3): 616-627.

Ford, C. C., T. L. Ceckler, J. Karp and R. M. Herndon (1990). Magnetic resonance imaging of experimental demyelinating lesions. Magn Reson Med 14(3): 461-481.

Forge, J. K., T. V. Pedchenko and S. M. LeVine (1998). Iron deposits in the central nervous system of SJL mice with experimental allergic encephalomyelitis. Life Sci 63(25): 2271-2284.

Gaitan, M. I., P. Maggi, J. Wohler, E. Leibovitch, P. Sati, I. L. Calandri, H. Merkle, L. Massacesi, A. C. Silva, S. Jacobson and D. S. Reich (2014). Perivenular brain lesions in a primate multiple sclerosis model at 7-tesla magnetic resonance imaging. Mult Scler 20(1): 64-71.

Gamache, D. A. and E. F. Ellis (1986). Effect of dexamethasone, indomethacin, ibuprofen, and probenecid on carrageenan-induced brain inflammation. J Neurosurg 65(5): 686-692.

Gao, T., Y. Wang and Z. Zhang (2008). Silent cerebral microbleeds on susceptibility-weighted imaging of patients with ischemic stroke and leukoaraiosis. Neurol Res 30(3): 272-276.

Gareau, P. J., B. K. Rutt, S. J. Karlik and J. R. Mitchell (2000). Magnetization transfer and multicomponent T2 relaxation measurements with histopathologic correlation in an experimental model of MS. J Magn Reson Imaging 11(6): 586-595.

Gareau, P. J., A. C. Wymore, G. P. Cofer and G. A. Johnson (2002). Imaging inflammation: direct visualization of perivascular cuffing in EAE by magnetic resonance microscopy. J Magn Reson Imaging 16(1): 28-36.

Ge, Y., J. H. Jensen, H. Lu, J. A. Helpern, L. Miles, M. Inglese, J. S. Babb, J. Herbert and R. I. Grossman (2007). Quantitative assessment of iron accumulation in the deep gray matter of multiple sclerosis by magnetic field correlation imaging. AJNR Am J Neuroradiol 28(9): 1639-1644.

Ge, Y., V. M. Zohrabian, E. O. Osa, J. Xu, H. Jaggi, J. Herbert, E. M. Haacke and R. I. Grossman (2009). Diminished visibility of cerebral venous vasculature in multiple sclerosis by susceptibility-weighted imaging at 3.0 Tesla. J Magn Reson Imaging 29(5): 1190-1194.

Goncalves DaSilva, A. and V. W. Yong (2009). Matrix metalloproteinase-12 deficiency worsens relapsing-remitting experimental autoimmune encephalomyelitis in association with cytokine and chemokine dysregulation. Am J Pathol 174(3): 898-909.

Goodin, D. S., E. M. Frohman, G. P. Garmany, Jr., J. Halper, W. H. Likosky, F. D. Lublin, D. H. Silberberg, W. H. Stuart, S. van den Noort, Therapeutics, N. Technology Assessment Subcommittee of the American Academy of and M. S. C. f. C. P. G. the (2002). Disease modifying therapies in multiple sclerosis: report of the Therapeutics and Technology Assessment Subcommittee of the American Academy of Neurology and the MS Council for Clinical Practice Guidelines. Neurology 58(2): 169-178.

Grabner, G., A. Dal-Bianco, M. Schernthaner, K. Vass, H. Lassmann and S. Trattnig (2011). Analysis of multiple sclerosis lesions using a fusion of 3.0 T FLAIR and 7.0 T SWI phase: FLAIR SWI. J Magn Reson Imaging 33(3): 543-549.

Graca, D. L. and W. F. Blakemore (1986). Delayed remyelination in rat spinal cord following ethidium bromide injection. Neuropathol Appl Neurobiol 12(6): 593-605.

Grant, S. M., J. A. Wiesinger, J. L. Beard and M. T. Cantorna (2003). Iron-deficient mice fail to develop autoimmune encephalomyelitis. J Nutr 133(8): 2635-2638.

Greer, S. N., J. L. Metcalf, Y. Wang and M. Ohh (2012). The updated biology of hypoxia-inducible factor. EMBO J 31(11): 2448-2460.

Gresle, M. M., K. Schulz, A. Jonas, V. M. Perreau, T. Cipriani, A. G. Baxter, S. Miranda-Hernandez, J. Field, V. G. Jokubaitis, R. Cherny, I. Volitakis, S. David, T. J. Kilpatrick and H. Butzkueven (2014). Ceruloplasmin gene-deficient mice with experimental autoimmune encephalomyelitis show attenuated early disease evolution. J Neurosci Res 92(6): 732-742.

Gupta, D., J. Saini, C. Kesavadas, P. S. Sarma and A. Kishore (2010). Utility of susceptibility-weighted MRI in differentiating Parkinson's disease and atypical parkinsonism. Neuroradiology 52(12): 1087-1094.

Haacke, E. M., N. Y. Cheng, M. J. House, Q. Liu, J. Neelavalli, R. J. Ogg, A. Khan, M. Ayaz, W. Kirsch and A. Obenaus (2005). Imaging iron stores in the brain using magnetic resonance imaging. Magn Reson Imaging 23(1): 1-25.

Haacke, E. M., M. Makki, Y. Ge, M. Maheshwari, V. Sehgal, J. Hu, M. Selvan, Z. Wu, Z. Latif, Y. Xuan, O. Khan, J. Garbern and R. I. Grossman (2009a). Characterizing iron deposition in multiple sclerosis lesions using susceptibility weighted imaging. J Magn Reson Imaging 29(3): 537-544.

Haacke, E. M., S. Mittal, Z. Wu, J. Neelavalli and Y. C. Cheng (2009b). Susceptibility-weighted imaging: technical aspects and clinical applications, part 1. AJNR Am J Neuroradiol 30(1): 19-30.

Haacke, E. M. and J. R. Reichenbach (2011). Susceptibility Weighted Imaging in MRI: Basic Concepts and Clinincal Applications, Wiley-Blackwell.

Haacke, E. M., Y. Xu, Y. C. Cheng and J. R. Reichenbach (2004). Susceptibility weighted imaging (SWI). Magn Reson Med 52(3): 612-618.

Hametner, S., I. Wimmer, L. Haider, S. Pfeifenbring, W. Bruck and H. Lassmann (2013). Iron and neurodegeneration in the multiple sclerosis brain. Ann Neurol 74(6): 848-861.

Hammond, K. E., M. Metcalf, L. Carvajal, D. T. Okuda, R. Srinivasan, D. Vigneron, S. J. Nelson and D. Pelletier (2008). Quantitative in vivo magnetic resonance imaging of multiple sclerosis at 7 Tesla with sensitivity to iron. Ann Neurol 64(6): 707-713.

Hart, B. A., J. Bauer, H. J. Muller, B. Melchers, K. Nicolay, H. Brok, R. E. Bontrop, H. Lassmann and L. Massacesi (1998). Histopathological characterization of magnetic resonance imaging-detectable brain white matter lesions in a primate model of multiple sclerosis: a correlative study in the experimental autoimmune encephalomyelitis model in common marmosets (Callithrix jacchus). Am J Pathol 153(2): 649-663.

Heesen, C., S. M. Gold, I. Huitinga and J. M. Reul (2007). Stress and hypothalamic-pituitary-adrenal axis function in experimental autoimmune encephalomyelitis and multiple sclerosis - a review. Psychoneuroendocrinology 32(6): 604-618.

Hopkins, J. A. and F. W. Wehrli (1997). Magnetic susceptibility measurement of insoluble solids by NMR: magnetic susceptibility of bone. Magn Reson Med 37(4): 494-500.

Hopp, K., B. F. Popescu, R. P. McCrea, S. L. Harder, C. A. Robinson, M. E. Haacke, A. H. Rajput, A. Rajput and H. Nichol (2010). Brain iron detected by SWI high pass filtered phase calibrated with synchrotron X-ray fluorescence. J Magn Reson Imaging 31(6): 1346-1354.

Huang, F. W., J. L. Pinkus, G. S. Pinkus, M. D. Fleming and N. C. Andrews (2005). A mouse model of juvenile hemochromatosis. J Clin Invest 115(8): 2187-2191.

Huebner, K. D., N. G. Shrive and C. B. Frank (2014). Dexamethasone inhibits inflammation and cartilage damage in a new model of post-traumatic osteoarthritis. J Orthop Res 32(4): 566-572.

Hyder, F., R. G. Shulman and D. L. Rothman (1998). A model for the regulation of cerebral oxygen delivery. J Appl Physiol (1985) 85(2): 554-564.

Ji, N., N. Rao, N. M. Guentzel, B. P. Arulanandam and T. G. Forsthuber (2011). Anaphylaxis and mortality induced by treatment of mice with anti-VLA-4 antibody and pertussis toxin. J Immunol 186(5): 2750-2756.

Jones, M. V., T. T. Nguyen, C. A. Deboy, J. W. Griffin, K. A. Whartenby, D. A. Kerr and P. A. Calabresi (2008). Behavioral and pathological outcomes in MOG 35-55 experimental autoimmune encephalomyelitis. J Neuroimmunol 199(1-2): 83-93.

Juurlink, B. H. (2013). The evidence for hypoperfusion as a factor in multiple sclerosis lesion development. Mult Scler Int 2013: 598093.

Karlik, S. J., E. A. Grant, D. Lee and J. H. Noseworthy (1993). Gadolinium enhancement in acute and chronic-progressive experimental allergic encephalomyelitis in the guinea pig. Magn Reson Med 30(3): 326-331.

Kau, T., M. Taschwer, H. Deutschmann, M. Schonfelder, J. R. Weber and K. A. Hausegger (2013). The "central vein sign": is there a place for susceptibility weighted imaging in possible multiple sclerosis? Eur Radiol 23(7): 1956-1962.

Keough, M. B. and V. W. Yong (2013). Remyelination therapy for multiple sclerosis. Neurotherapeutics 10(1): 44-54.

Kerfoot, S. M., M. U. Norman, B. M. Lapointe, C. S. Bonder, L. Zbytnuik and P. Kubes (2006). Reevaluation of P-selectin and alpha 4 integrin as targets for the treatment of experimental autoimmune encephalomyelitis. J Immunol 176(10): 6225-6234.

Khalil, M., C. Enzinger, C. Langkammer, M. Tscherner, M. Wallner-Blazek, M. Jehna, S. Ropele, S. Fuchs and F. Fazekas (2009). Quantitative assessment of brain iron by R(2)* relaxometry in patients with clinically isolated syndrome and relapsing-remitting multiple sclerosis. Mult Scler 15(9): 1048-1054.

Khalil, M., C. Langkammer, S. Ropele, K. Petrovic, M. Wallner-Blazek, M. Loitfelder, M. Jehna, G. Bachmaier, R. Schmidt, C. Enzinger, S. Fuchs and F. Fazekas (2011). Determinants of brain iron in multiple sclerosis: a quantitative 3T MRI study. Neurology 77(18): 1691-1697.

Kipp, M., B. Van Der Star, D. Y. S. Vogel, F. Puentes, P. Van Der Valk, D. Baker and S. Amor (2012). Experimental in vivo and in vitro models of multiple sclerosis: EAE and beyond. Multiple Sclerosis and Related Disorders 1(1): 15-28.

Koong, A. C., E. Y. Chen and A. J. Giaccia (1994). Hypoxia causes the activation of nuclear factor kappa B through the phosphorylation of I kappa B alpha on tyrosine residues. Cancer Res 54(6): 1425-1430.

Kuharik, M. A., M. K. Edwards, M. R. Farlow, G. J. Becker, B. Azzarelli, E. C. Klatte, G. T. Augustyn and R. G. Dreesen (1988). Gd-enhanced MR imaging of acute and chronic experimental demyelinating lesions. AJNR Am J Neuroradiol 9(4): 643-648.

Kuvibidila, S., M. Dardenne, W. Savino and F. Lepault (1990). Influence of iron-deficiency anemia on selected thymus functions in mice: thymulin biological activity, T-cell subsets, and thymocyte proliferation. Am J Clin Nutr 51(2): 228-232.

Ladewig, G., L. Jestaedt, B. Misselwitz, L. Solymosi, K. Toyka, M. Bendszus and G. Stoll (2009). Spatial diversity of blood-brain barrier alteration and macrophage invasion in experimental autoimmune encephalomyelitis: a comparative MRI study. Exp Neurol 220(1): 207-211.

Langer-Gould, A., S. W. Atlas, A. J. Green, A. W. Bollen and D. Pelletier (2005). Progressive multifocal leukoencephalopathy in a patient treated with natalizumab. N Engl J Med 353(4): 375-381.

Langkammer, C., N. Krebs, W. Goessler, E. Scheurer, F. Ebner, K. Yen, F. Fazekas and S. Ropele (2010). Quantitative MR imaging of brain iron: a postmortem validation study. Radiology 257(2): 455-462.

Larsen, P. H., J. E. Wells, W. B. Stallcup, G. Opdenakker and V. W. Yong (2003). Matrix metalloproteinase-9 facilitates remyelination in part by processing the inhibitory NG2 proteoglycan. J Neurosci 23(35): 11127-11135.

Laule, C., I. M. Vavasour, E. Leung, D. K. Li, P. Kozlowski, A. L. Traboulsee, J. Oger, A. L. Mackay and G. R. Moore (2011). Pathological basis of diffusely abnormal white matter: insights from magnetic resonance imaging and histology. Mult Scler 17(2): 144-150.

Lebel, R. M., A. Eissa, P. Seres, G. Blevins and A. H. Wilman (2012). Quantitative high field imaging of sub-cortical gray matter in multiple sclerosis. Mult Scler 18: 433-441.

Lee, J., K. Shmueli, B. T. Kang, B. Yao, M. Fukunaga, P. van Gelderen, S. Palumbo, F. Bosetti, A. C. Silva and J. H. Duyn (2012a). The contribution of myelin to magnetic susceptibility-weighted contrasts in high-field MRI of the brain. Neuroimage 59(4): 3967-3975.

Lee, J. H., T. I. Yang, M. Cho, K. T. Yoon, S. K. Baik and Y. H. Han (2012b). Widespread cerebral cortical mineralization in Wilson's disease detected by susceptibility-weighted imaging. J Neurol Sci 313(1-2): 54-56.

Lei, H., O. Grinberg, C. I. Nwaigwe, H. G. Hou, H. Williams, H. M. Swartz and J. F. Dunn (2001). The effects of ketamine-xylazine anesthesia on cerebral blood flow and oxygenation observed using nuclear magnetic resonance perfusion imaging and electron paramagnetic resonance oximetry. Brain Res 913(2): 174-179.

LeVine, S. M. (1997). Iron deposits in multiple sclerosis and Alzheimer's disease brains. Brain Res 760(1-2): 298-303.

Leybaert, L. (2005). Neurobarrier coupling in the brain: a partner of neurovascular and neurometabolic coupling? J Cereb Blood Flow Metab 25(1): 2-16.

Li, D. K., M. J. Li, A. Traboulsee, G. Zhao, A. Riddehough and D. Paty (2006). The use of MRI as an outcome measure in clinical trials. Adv Neurol 98: 203-226.

Liu, C., W. Li, G. A. Johnson and B. Wu (2011). High-field (9.4 T) MRI of brain dysmyelination by quantitative mapping of magnetic susceptibility. Neuroimage 56(3): 930-938.

Lu, M., M. H. Cohen, D. Rieves and R. Pazdur (2010). FDA report: Ferumoxytol for intravenous iron therapy in adult patients with chronic kidney disease. Am J Hematol 85(5): 315-319.

Lublin, F. D. and S. C. Reingold (1996). Defining the clinical course of multiple sclerosis: results of an international survey. National Multiple Sclerosis Society (USA) Advisory Committee on Clinical Trials of New Agents in Multiple Sclerosis. Neurology 46(4): 907-911.

Ludwin, S. K., J. M. Henry and M. H.F. (2001). Vascular proliferation and angiogenesis in MS: clinical and pathogenic implications. J Neuropathol Exp Neurol 60: 505.

Lycke, J., C. Wikkelso, A. C. Bergh, L. Jacobsson and O. Andersen (1993). Regional cerebral blood flow in multiple sclerosis measured by single photon emission tomography with technetium-99m hexamethylpropyleneamine oxime. Eur Neurol 33(2): 163-167.

MacKay, A., K. Whittall, J. Adler, D. Li, D. Paty and D. Graeb (1994). In vivo visualization of myelin water in brain by magnetic resonance. Magn Reson Med 31(6): 673-677.

MacKenzie-Graham, A., G. A. Rinek, A. Avedisian, S. M. Gold, A. J. Frew, C. Aguilar, D. R. Lin, E. Umeda, R. R. Voskuhl and J. R. Alger (2012). Cortical atrophy in

experimental autoimmune encephalomyelitis: in vivo imaging. Neuroimage 60(1): 95-104.

MacKenzie-Graham, A., M. R. Tinsley, K. P. Shah, C. Aguilar, L. V. Strickland, J. Boline, M. Martin, L. Morales, D. W. Shattuck, R. E. Jacobs, R. R. Voskuhl and A. W. Toga (2006). Cerebellar cortical atrophy in experimental autoimmune encephalomyelitis. Neuroimage 32(3): 1016-1023.

MacKenzie-Graham, A., S. K. Tiwari-Woodruff, G. Sharma, C. Aguilar, K. T. Vo, L. V. Strickland, L. Morales, B. Fubara, M. Martin, R. E. Jacobs, G. A. Johnson, A. W. Toga and R. R. Voskuhl (2009). Purkinje cell loss in experimental autoimmune encephalomyelitis. Neuroimage 48(4): 637-651.

Macmillan, C. J., R. J. Starkey and A. S. Easton (2011). Angiogenesis is regulated by angiopoietins during experimental autoimmune encephalomyelitis and is indirectly related to vascular permeability. J Neuropathol Exp Neurol 70(12): 1107-1123.

Mao, P. and P. H. Reddy (2010). Is multiple sclerosis a mitochondrial disease? Biochim Biophys Acta 1802(1): 66-79.

Markl, M. and J. Leupold (2012). Gradient echo imaging. J Magn Reson Imaging 35(6): 1274-1289.

Matsushima, G. K. and P. Morell (2001). The neurotoxicant, cuprizone, as a model to study demyelination and remyelination in the central nervous system. Brain Pathol 11(1): 107-116.

Matute, C. (2011). Glutamate and ATP signalling in white matter pathology. J Anat 219(1): 53-64.

McCreary, C. R., T. A. Bjarnason, V. Skihar, J. R. Mitchell, V. W. Yong and J. F. Dunn (2009). Multiexponential T2 and magnetization transfer MRI of demyelination and remyelination in murine spinal cord. Neuroimage 45(4): 1173-1182.

McDonald, W. I., A. Compston, G. Edan, D. Goodkin, H. P. Hartung, F. D. Lublin, H. F. McFarland, D. W. Paty, C. H. Polman, S. C. Reingold, M. Sandberg-Wollheim, W. Sibley, A. Thompson, S. van den Noort, B. Y. Weinshenker and J. S. Wolinsky (2001). Recommended diagnostic criteria for multiple sclerosis: guidelines from the International Panel on the diagnosis of multiple sclerosis. Ann Neurol 50(1): 121-127.

McGahan, M. C., J. Harned, M. Mukunnemkeril, M. Goralska, L. Fleisher and J. B. Ferrell (2005). Iron alters glutamate secretion by regulating cytosolic aconitase activity. Am J Physiol Cell Physiol 288(5): C1117-1124.

McRobbie, D. W., E. A. Moore, M. J. Graves and M. R. Prince (2003). MRI from Picture to Proton, Cambridge University Press.

Meding, J., M. Urich, K. Licha, M. Reinhardt, B. Misselwitz, Z. A. Fayad and H. J. Weinmann (2007). Magnetic resonance imaging of atherosclerosis by targeting extracellular matrix deposition with Gadofluorine M. Contrast Media Mol Imaging 2(3): 120-129.

Mengozzi, M., I. Cervellini, P. Bigini, S. Martone, A. Biondi, R. Pedotti, B. Gallo, S. Barbera, T. Mennini, M. Boraso, M. Marinovich, E. Petit, M. Bernaudin, R. Bianchi, B. Viviani and P. Ghezzi (2008). Endogenous erythropoietin as part of the cytokine network in the pathogenesis of experimental autoimmune encephalomyelitis. Mol Med 14(11-12): 682-688.

Merkler, D., S. Boretius, C. Stadelmann, T. Ernsting, T. Michaelis, J. Frahm and W. Bruck (2005). Multicontrast MRI of remyelination in the central nervous system. NMR Biomed 18(6): 395-403.

Merrill, J. E. (2009). In vitro and in vivo pharmacological models to assess demyelination and remyelination. Neuropsychopharmacology 34(1): 55-73.

Miller, D., F. Barkhof, X. Montalban, A. Thompson and M. Filippi (2005). Clinically isolated syndromes suggestive of multiple sclerosis, part I: natural history, pathogenesis, diagnosis, and prognosis. Lancet Neurol 4(5): 281-288.

Millward, J. M., J. Schnorr, M. Taupitz, S. Wagner, J. T. Wuerfel and C. Infante-Duarte (2013). Iron oxide magnetic nanoparticles highlight early involvement of the choroid plexus in central nervous system inflammation. ASN Neuro 5(1): e00110.

Mistry, N., J. Dixon, E. Tallantyre, C. Tench, R. Abdel-Fahim, T. Jaspan, P. S. Morgan, P. Morris and N. Evangelou (2013). Central Veins in Brain Lesions Visualized With High-Field Magnetic Resonance Imaging: A Pathologically Specific Diagnostic Biomarker for Inflammatory Demyelination in the Brain. JAMA Neurol: 1-6.

Mitchell, K. M., A. L. Dotson, K. M. Cool, A. Chakrabarty, S. H. Benedict and S. M. LeVine (2007). Deferiprone, an orally deliverable iron chelator, ameliorates experimental autoimmune encephalomyelitis. Mult Scler 13(9): 1118-1126.

Montalban, X., M. Tintore, J. Swanton, F. Barkhof, F. Fazekas, M. Filippi, J. Frederiksen, L. Kappos, J. Palace, C. Polman, M. Rovaris, N. de Stefano, A. Thompson, T. Yousry, A. Rovira and D. H. Miller (2010). MRI criteria for MS in patients with clinically isolated syndromes. Neurology 74(5): 427-434.

Montero, E., G. Nussbaum, J. F. Kaye, R. Perez, A. Lage, A. Ben-Nun and I. R. Cohen (2004). Regulation of experimental autoimmune encephalomyelitis by CD4+, CD25+ and CD8+ T cells: analysis using depleting antibodies. J Autoimmun 23(1): 1-7.

Mori, Y., M. Murakami, Y. Arima, D. Zhu, Y. Terayama, Y. Komai, Y. Nakatsuji, D. Kamimura and Y. Yoshioka (2014). Early pathological alterations of lower lumbar cords detected by ultrahigh-field MRI in a mouse multiple sclerosis model. Int Immunol 26(2): 93-101.

Myhr, K. M. and S. I. Mellgren (2009). Corticosteroids in the treatment of multiple sclerosis. Acta Neurol Scand Suppl(189): 73-80.

Nathoo, N., S. Agrawal, Y. Wu, S. Haylock-Jacobs, V. W. Yong, T. Foniok, S. Barnes, A. Obenaus and J. F. Dunn (2013). Susceptibility-weighted imaging in the experimental autoimmune encephalomyelitis model of multiple sclerosis indicates elevated deoxyhemoglobin, iron deposition and demyelination. Mult Scler 19(6): 721-731.

Nathoo, N., V. W. Yong and J. F. Dunn (2014a). Understanding disease processes in multiple sclerosis through magnetic resonance imaging studies in animal models. NeuroImage: Clinical 4: 743-756.

Nathoo, N., V. W. Yong and J. F. Dunn (2014b). Using magnetic resonance imaging in animal models to guide drug development in multiple sclerosis. Mult Scler 20(1): 3-11.

Neema, M., A. Arora, B. C. Healy, Z. D. Guss, S. D. Brass, Y. Duan, G. J. Buckle, B. I. Glanz, L. Stazzone, S. J. Khoury, H. L. Weiner, C. R. Guttmann and R. Bakshi

(2009). Deep gray matter involvement on brain MRI scans is associated with clinical progression in multiple sclerosis. J Neuroimaging 19(1): 3-8.

Nessler, S., S. Boretius, C. Stadelmann, A. Bittner, D. Merkler, H. P. Hartung, T. Michaelis, W. Bruck, J. Frahm, N. Sommer and B. Hemmer (2007). Early MRI changes in a mouse model of multiple sclerosis are predictive of severe inflammatory tissue damage. Brain 130(Pt 8): 2186-2198.

Nguyen, K. B., P. A. McCombe and M. P. Pender (1997). Increased apoptosis of T lymphocytes and macrophages in the central and peripheral nervous systems of Lewis rats with experimental autoimmune encephalomyelitis treated with dexamethasone. J Neuropathol Exp Neurol 56(1): 58-69.

Ogawa, S., R. S. Menon, D. W. Tank, S. G. Kim, H. Merkle, J. M. Ellermann and K. Ugurbil (1993). Functional brain mapping by blood oxygenation level-dependent contrast magnetic resonance imaging. A comparison of signal characteristics with a biophysical model. Biophys J 64(3): 803-812.

Olechowski, C. J., J. J. Truong and B. J. Kerr (2009). Neuropathic pain behaviours in a chronic-relapsing model of experimental autoimmune encephalomyelitis (EAE). Pain 141(1-2): 156-164.

Oweida, A. J., E. A. Dunn, S. J. Karlik, G. A. Dekaban and P. J. Foster (2007). Iron-oxide labeling of hematogenous macrophages in a model of experimental autoimmune encephalomyelitis and the contribution to signal loss in fast imaging employing steady state acquisition (FIESTA) images. J Magn Reson Imaging 26(1): 144-151.

Paling, D., D. Tozer, C. Wheeler-Kingshott, R. Kapoor, D. H. Miller and X. Golay (2012). Reduced R2' in multiple sclerosis normal appearing white matter and lesions may reflect decreased myelin and iron content. J Neurol Neurosurg Psychiatry 83(8): 785-792.

Papandreou, I., R. A. Cairns, L. Fontana, A. L. Lim and N. C. Denko (2006). HIF-1 mediates adaptation to hypoxia by actively downregulating mitochondrial oxygen consumption. Cell Metab 3(3): 187-197.

Pauling, L. and C. D. Coryell (1936). The Magnetic Properties and Structure of Hemoglobin, Oxyhemoglobin and Carbonmonoxyhemoglobin. Proc Natl Acad Sci U S A 22(4): 210-216.

Pedchenko, T. V. and S. M. LeVine (1998). Desferrioxamine suppresses experimental allergic encephalomyelitis induced by MBP in SJL mice. J Neuroimmunol 84(2): 188-197.

Petrella, J. R. and J. M. Provenzale (2000). MR perfusion imaging of the brain: techniques and applications. AJR Am J Roentgenol 175(1): 207-219.

Piraino, P. S., T. A. Yednock, S. B. Freedman, E. K. Messersmith, M. A. Pleiss and S. J. Karlik (2005). Suppression of acute experimental allergic encephalomyelitis with a small molecule inhibitor of alpha4 integrin. Mult Scler 11(6): 683-690.

Pirko, I., J. Gamez, A. J. Johnson, S. I. Macura and M. Rodriguez (2004a). Dynamics of MRI lesion development in an animal model of viral-induced acute progressive CNS demyelination. Neuroimage 21(2): 576-582.

Pirko, I., A. Johnson, J. Gamez, S. I. Macura and M. Rodriguez (2004b). Disappearing "T1 black holes" in an animal model of multiple sclerosis. Front Biosci 9: 1222-1227.

Pirko, I., A. J. Johnson, Y. Chen, D. M. Lindquist, A. K. Lohrey, J. Ying and R. S. Dunn (2011). Brain atrophy correlates with functional outcome in a murine model of multiple sclerosis. Neuroimage 54(2): 802-806.

Pirko, I., A. J. Johnson, A. K. Lohrey, Y. Chen and J. Ying (2009). Deep gray matter T2 hypointensity correlates with disability in a murine model of MS. J Neurol Sci 282(1-2): 34-38.

Plewes, D. B. and W. Kucharczyk (2012). Physics of MRI: a primer. J Magn Reson Imaging 35(5): 1038-1054.

Polman, C. H., S. C. Reingold, B. Banwell, M. Clanet, J. A. Cohen, M. Filippi, K. Fujihara, E. Havrdova, M. Hutchinson, L. Kappos, F. D. Lublin, X. Montalban, P. O'Connor, M. Sandberg-Wollheim, A. J. Thompson, E. Waubant, B. Weinshenker and J. S. Wolinsky (2011). Diagnostic criteria for multiple sclerosis: 2010 revisions to the McDonald criteria. Ann Neurol 69(2): 292-302.

Polman, C. H., S. C. Reingold, G. Edan, M. Filippi, H. P. Hartung, L. Kappos, F. D. Lublin, L. M. Metz, H. F. McFarland, P. W. O'Connor, M. Sandberg-Wollheim, A. J. Thompson, B. G. Weinshenker and J. S. Wolinsky (2005). Diagnostic criteria for multiple sclerosis: 2005 revisions to the "McDonald Criteria". Ann Neurol 58(6): 840-846.

Preece, N. E., D. Baker, C. Butter, D. G. Gadian and J. Urenjak (1993). Experimental allergic encephalomyelitis raises betaine levels in the spinal cord of strain 13 guinea-pigs. NMR Biomed 6(3): 194-200.

Ransohoff, R. M. (2012). Animal models of multiple sclerosis: the good, the bad and the bottom line. Nat Neurosci 15(8): 1074-1077.

Rausch, M., P. Hiestand, D. Baumann, C. Cannet and M. Rudin (2003). MRI-based monitoring of inflammation and tissue damage in acute and chronic relapsing EAE. Magn Reson Med 50(2): 309-314.

Rausch, M., P. Hiestand, C. A. Foster, D. R. Baumann, C. Cannet and M. Rudin (2004). Predictability of FTY720 efficacy in experimental autoimmune encephalomyelitis by in vivo macrophage tracking: clinical implications for ultrasmall superparamagnetic iron oxide-enhanced magnetic resonance imaging. J Magn Reson Imaging 20(1): 16-24.

Rausch, M., P. Tofts, P. Lervik, A. Walmsley, A. Mir, A. Schubart and T. Seabrook (2009). Characterization of white matter damage in animal models of multiple sclerosis by magnetization transfer ratio and quantitative mapping of the apparent bound proton fraction f. Mult Scler 15(1): 16-27.

Rauscher, A., J. Sedlacik, M. Barth, E. M. Haacke and J. R. Reichenbach (2005). Nonnvasive assessment of vascular architecture and function during modulated blood oxygenation using susceptibility weighted magnetic resonance imaging. Magn Reson Med 54(1): 87-95.

Recks, M. S., K. Addicks and S. Kuerten (2011). Spinal cord histopathology of MOG peptide 35-55-induced experimental autoimmune encephalomyelitis is time- and score-dependent. Neurosci Lett 494(3): 227-231.

Richards, T. L., E. C. Alvord, Jr., J. Peterson, S. Cosgrove, R. Petersen, K. Petersen, A. C. Heide, J. Cluff and L. M. Rose (1995). Experimental allergic encephalomyelitis in

non-human primates: MRI and MRS may predict the type of brain damage. NMR Biomed 8(2): 49-58.
Rius, J., M. Guma, C. Schachtrup, K. Akassoglou, A. S. Zinkernagel, V. Nizet, R. S. Johnson, G. G. Haddad and M. Karin (2008). NF-kappaB links innate immunity to the hypoxic response through transcriptional regulation of HIF-1alpha. Nature 453(7196): 807-811.
Saidha, S., C. Eckstein and P. A. Calabresi (2012). New and emerging disease modifying therapies for multiple sclerosis. Ann N Y Acad Sci 1247: 117-137.
Sands, S. A., R. Williams, S. Marshall, 3rd and S. M. LeVine (2014). Perivascular iron deposits are associated with protein nitration in cerebral experimental autoimmune encephalomyelitis. Neurosci Lett.
Scheinman, R. I., P. C. Cogswell, A. K. Lofquist and A. S. Baldwin, Jr. (1995). Role of transcriptional activation of I kappa B alpha in mediation of immunosuppression by glucocorticoids. Science 270(5234): 283-286.
Schellenberg, A. E., R. Buist, V. W. Yong, M. R. Del Bigio and J. Peeling (2007). Magnetic resonance imaging of blood-spinal cord barrier disruption in mice with experimental autoimmune encephalomyelitis. Magn Reson Med 58(2): 298-305.
Schenck, J. F. (1992). Health and physiological effects of human exposure to whole-body four-tesla magnetic fields during MRI. Ann N Y Acad Sci 649: 285-301.
Schenck, J. F. (1996). The role of magnetic susceptibility in magnetic resonance imaging: MRI magnetic compatibility of the first and second kinds. Med Phys 23(6): 815-850.
Schrag, M., G. McAuley, J. Pomakian, A. Jiffry, S. Tung, C. Mueller, H. V. Vinters, E. M. Haacke, B. Holshouser, D. Kido and W. M. Kirsch (2010). Correlation of hypointensities in susceptibility-weighted images to tissue histology in dementia patients with cerebral amyloid angiopathy: a postmortem MRI study. Acta Neuropathol 119(3): 291-302.
Schröder, L. and C. Faber (2011). In Vivo NMR Imaging: Methods and Protocols, Humana Press.
Schuh, C., I. Wimmer, S. Hametner, L. Haider, A. M. Van Dam, R. S. Liblau, K. J. Smith, L. Probert, C. J. Binder, J. Bauer, M. Bradl, D. Mahad and H. Lassmann (2014). Oxidative tissue injury in multiple sclerosis is only partly reflected in experimental disease models. Acta Neuropathol.
Seabrook, T. J., A. Littlewood-Evans, V. Brinkmann, B. Pollinger, C. Schnell and P. C. Hiestand (2010). Angiogenesis is present in experimental autoimmune encephalomyelitis and pro-angiogenic factors are increased in multiple sclerosis lesions. J Neuroinflammation 7: 95.
Serres, S., C. Bristow, R. M. de Pablos, D. Merkler, M. S. Soto, N. R. Sibson and D. C. Anthony (2013). Magnetic resonance imaging reveals therapeutic effects of interferon-beta on cytokine-induced reactivation of rat model of multiple sclerosis. J Cereb Blood Flow Metab 33(5): 744-753.
Silva, A. C. and N. A. Bock (2008). Manganese-enhanced MRI: an exceptional tool in translational neuroimaging. Schizophr Bull 34(4): 595-604.
Skripuletz, T., M. Lindner, A. Kotsiari, N. Garde, J. Fokuhl, F. Linsmeier, C. Trebst and M. Stangel (2008). Cortical demyelination is prominent in the murine cuprizone model and is strain-dependent. Am J Pathol 172(4): 1053-1061.

Smorodchenko, A., J. Wuerfel, E. E. Pohl, J. Vogt, E. Tysiak, R. Glumm, S. Hendrix, R. Nitsch, F. Zipp and C. Infante-Duarte (2007). CNS-irrelevant T-cells enter the brain, cause blood-brain barrier disruption but no glial pathology. Eur J Neurosci 26(6): 1387-1398.

Soares, D. P. and M. Law (2009). Magnetic resonance spectroscopy of the brain: review of metabolites and clinical applications. Clin Radiol 64(1): 12-21.

Song, S. K., S. W. Sun, W. K. Ju, S. J. Lin, A. H. Cross and A. H. Neufeld (2003). Diffusion tensor imaging detects and differentiates axon and myelin degeneration in mouse optic nerve after retinal ischemia. Neuroimage 20(3): 1714-1722.

Song, S. K., J. Yoshino, T. Q. Le, S. J. Lin, S. W. Sun, A. H. Cross and R. C. Armstrong (2005). Demyelination increases radial diffusivity in corpus callosum of mouse brain. Neuroimage 26(1): 132-140.

Stadelmann, C., S. Ludwin, T. Tabira, A. Guseo, C. F. Lucchinetti, L. Leel-Ossy, A. T. Ordinario, W. Bruck and H. Lassmann (2005). Tissue preconditioning may explain concentric lesions in Balo's type of multiple sclerosis. Brain 128(Pt 5): 979-987.

Steinman, L. and S. S. Zamvil (2005). Virtues and pitfalls of EAE for the development of therapies for multiple sclerosis. Trends Immunol 26(11): 565-571.

Steinman, L. and S. S. Zamvil (2006). How to successfully apply animal studies in experimental allergic encephalomyelitis to research on multiple sclerosis. Ann Neurol 60(1): 12-21.

Stephenson, E., N. Nathoo, Y. Mahjoub, J. F. Dunn and V. W. Yong (2014). Iron in multiple sclerosis: roles in neurodegeneration and repair. Nat Rev Neurol.

Stoll, G. and M. Bendszus (2010). New approaches to neuroimaging of central nervous system inflammation. Curr Opin Neurol 23(3): 282-286.

Stoll, G., C. Kleinschnitz, S. G. Meuth, S. Braeuninger, C. W. Ip, C. Wessig, I. Nolte and M. Bendszus (2009). Transient widespread blood-brain barrier alterations after cerebral photothrombosis as revealed by gadofluorine M-enhanced magnetic resonance imaging. J Cereb Blood Flow Metab 29(2): 331-341.

Sun, S. W., H. F. Liang, R. E. Schmidt, A. H. Cross and S. K. Song (2007). Selective vulnerability of cerebral white matter in a murine model of multiple sclerosis detected using diffusion tensor imaging. Neurobiol Dis 28(1): 30-38.

Sun, S. W., H. F. Liang, K. Trinkaus, A. H. Cross, R. C. Armstrong and S. K. Song (2006). Noninvasive detection of cuprizone induced axonal damage and demyelination in the mouse corpus callosum. Magn Reson Med 55(2): 302-308.

Sun, X., M. Tanaka, S. Kondo, K. Okamoto and S. Hirai (1998). Clinical significance of reduced cerebral metabolism in multiple sclerosis: a combined PET and MRI study. Ann Nucl Med 12(2): 89-94.

Swanton, J. K., K. Fernando, C. M. Dalton, K. A. Miszkiel, A. J. Thompson, G. T. Plant and D. H. Miller (2006). Modification of MRI criteria for multiple sclerosis in patients with clinically isolated syndromes. J Neurol Neurosurg Psychiatry 77(7): 830-833.

Swanton, J. K., A. Rovira, M. Tintore, D. R. Altmann, F. Barkhof, M. Filippi, E. Huerga, K. A. Miszkiel, G. T. Plant, C. Polman, M. Rovaris, A. J. Thompson, X. Montalban and D. H. Miller (2007). MRI criteria for multiple sclerosis in patients presenting

with clinically isolated syndromes: a multicentre retrospective study. Lancet Neurol 6(8): 677-686.
Tanaka, R., Y. Iwasaki and H. Koprowski (1975). Ultrastructural studies of perivascular cuffing cells in multiple sclerosis brain. Am J Pathol 81(3): 467-478.
Thiessen, J. D., Y. Zhang, H. Zhang, L. Wang, R. Buist, M. R. Del Bigio, J. Kong, X. M. Li and M. Martin (2013). Quantitative MRI and ultrastructural examination of the cuprizone mouse model of demyelination. NMR Biomed 26(11): 1562-1581.
Tonra, J. R. (2002). Cerebellar susceptibility to experimental autoimmune encephalomyelitis in SJL/J mice: potential interaction of immunology with vascular anatomy. Cerebellum 1(1): 57-68.
Tourdias, T., S. Roggerone, M. Filippi, M. Kanagaki, M. Rovaris, D. H. Miller, K. G. Petry, B. Brochet, J. P. Pruvo, E. W. Radue and V. Dousset (2012). Assessment of disease activity in multiple sclerosis phenotypes with combined gadolinium- and superparamagnetic iron oxide-enhanced MR imaging. Radiology 264(1): 225-233.
Trapp, B. D. and P. K. Stys (2009). Virtual hypoxia and chronic necrosis of demyelinated axons in multiple sclerosis. Lancet Neurol 8(3): 280-291.
Tremlett, H. L., D. K. Luscombe and C. M. Wiles (1998). Use of corticosteroids in multiple sclerosis by consultant neurologists in the United Kingdom. J Neurol Neurosurg Psychiatry 65(3): 362-365.
Tysiak, E., P. Asbach, O. Aktas, H. Waiczies, M. Smyth, J. Schnorr, M. Taupitz and J. Wuerfel (2009). Beyond blood brain barrier breakdown - in vivo detection of occult neuroinflammatory foci by magnetic nanoparticles in high field MRI. J Neuroinflammation 6: 20.
Vellinga, M. M., R. D. Oude Engberink, A. Seewann, P. J. Pouwels, M. P. Wattjes, S. M. van der Pol, C. Pering, C. H. Polman, H. E. de Vries, J. J. Geurts and F. Barkhof (2008). Pluriformity of inflammation in multiple sclerosis shown by ultra-small iron oxide particle enhancement. Brain 131(Pt 3): 800-807.
Vigue, B., C. Ract, N. Zlotine, P. E. Leblanc, K. Samii and B. Bissonnette (2000). Relationship between intracranial pressure, mild hypothermia and temperature-corrected PaCO2 in patients with traumatic brain injury. Intensive Care Med 26(6): 722-728.
Waiczies, H., J. M. Millward, S. Lepore, C. Infante-Duarte, A. Pohlmann, T. Niendorf and S. Waiczies (2012). Identification of cellular infiltrates during early stages of brain inflammation with magnetic resonance microscopy. PLoS One 7(3): e32796.
Walsh, A. J., G. Blevins, R. M. Lebel, P. Seres, D. J. Emery and A. H. Wilman (2014). Longitudinal MR imaging of iron in multiple sclerosis: an imaging marker of disease. Radiology 270(1): 186-196.
Walsh, A. J., R. M. Lebel, A. Eissa, G. Blevins, I. Catz, J. Q. Lu, L. Resch, E. S. Johnson, D. J. Emery, K. G. Warren and A. H. Wilman (2013). Multiple Sclerosis: Validation of MR Imaging for Quantification and Detection of Iron. Radiology 267(2): 531-542.
Wang, X., J. K. Brieland, J. H. Kim, Y. J. Chen, J. O'Neal, S. R. O'Neil, T. W. Tu, K. Trinkaus and S. K. Song (2013). Diffusion tensor imaging detects treatment effects of FTY720 in experimental autoimmune encephalomyelitis mice. NMR Biomed.
Waring, M. J. (1965). Complex formation between ethidium bromide and nucleic acids. J Mol Biol 13(1): 269-282.

Weaver, A., A. Goncalves da Silva, R. K. Nuttall, D. R. Edwards, S. D. Shapiro, S. Rivest and V. W. Yong (2005). An elevated matrix metalloproteinase (MMP) in an animal model of multiple sclerosis is protective by affecting Th1/Th2 polarization. FASEB J 19(12): 1668-1670.

Wiggermann, V., L. E. Lee, E. H. Torres, D. K. Li, A. L. MacKay, I. M. Vavasour, A. Traboulsee and A. Rauscher (2014). Iron accumulation is a rare feature in multiple sclerosis lesions. International Society for Magnetic Resonance in Medicine, Milan, Italy.

Williams, R., C. L. Buchheit, N. E. Berman and S. M. Levine (2012). Pathogenic implications of iron accumulation in multiple sclerosis. J Neurochem 120: 7-25.

Williams, R., A. M. Rohr, W. T. Wang, I. Y. Choi, P. Lee, N. E. Berman, S. G. Lynch and S. M. LeVine (2011). Iron deposition is independent of cellular inflammation in a cerebral model of multiple sclerosis. BMC Neurosci 12: 59.

Wolff, S. D. and R. S. Balaban (1989). Magnetization transfer contrast (MTC) and tissue water proton relaxation in vivo. Magn Reson Med 10(1): 135-144.

Woodruff, R. H. and R. J. Franklin (1999). Demyelination and remyelination of the caudal cerebellar peduncle of adult rats following stereotaxic injections of lysolecithin, ethidium bromide, and complement/anti-galactocerebroside: a comparative study. Glia 25(3): 216-228.

Wu, Q. Z., Q. Yang, H. S. Cate, D. Kemper, M. Binder, H. X. Wang, K. Fang, M. J. Quick, M. Marriott, T. J. Kilpatrick and G. F. Egan (2008). MRI identification of the rostral-caudal pattern of pathology within the corpus callosum in the cuprizone mouse model. J Magn Reson Imaging 27(3): 446-453.

Wuerfel, E., C. Infante-Duarte, R. Glumm and J. T. Wuerfel (2010). Gadofluorine M-enhanced MRI shows involvement of circumventricular organs in neuroinflammation. J Neuroinflammation 7: 70.

Wuerfel, J., E. Tysiak, T. Prozorovski, M. Smyth, S. Mueller, J. Schnorr, M. Taupitz and F. Zipp (2007). Mouse model mimics multiple sclerosis in the clinico-radiological paradox. Eur J Neurosci 26(1): 190-198.

Wust, S., J. van den Brandt, D. Tischner, A. Kleiman, J. P. Tuckermann, R. Gold, F. Luhder and H. M. Reichardt (2008). Peripheral T cells are the therapeutic targets of glucocorticoids in experimental autoimmune encephalomyelitis. J Immunol 180(12): 8434-8443.

Xie, M., J. E. Tobin, M. D. Budde, C. I. Chen, K. Trinkaus, A. H. Cross, D. P. McDaniel, S. K. Song and R. C. Armstrong (2010). Rostrocaudal analysis of corpus callosum demyelination and axon damage across disease stages refines diffusion tensor imaging correlations with pathological features. J Neuropathol Exp Neurol 69(7): 704-716.

Xu, S., E. K. Jordan, S. Brocke, J. W. Bulte, L. Quigley, N. Tresser, J. L. Ostuni, Y. Yang, H. F. McFarland and J. A. Frank (1998). Study of relapsing remitting experimental allergic encephalomyelitis SJL mouse model using MION-46L enhanced in vivo MRI: early histopathological correlation. J Neurosci Res 52(5): 549-558.

Yao, B., F. Bagnato, E. Matsuura, H. Merkle, P. van Gelderen, F. K. Cantor and J. H. Duyn (2012). Chronic Multiple Sclerosis Lesions: Characterization with High-Field-Strength MR Imaging. Radiology 262(1): 206-215.

Yates, P. A., R. Sirisriro, V. L. Villemagne, S. Farquharson, C. L. Masters and C. C. Rowe (2011). Cerebral microhemorrhage and brain beta-amyloid in aging and Alzheimer disease. Neurology 77(1): 48-54.

Yednock, T. A., C. Cannon, L. C. Fritz, F. Sanchez-Madrid, L. Steinman and N. Karin (1992). Prevention of experimental autoimmune encephalomyelitis by antibodies against alpha 4 beta 1 integrin. Nature 356(6364): 63-66.

Yong, V. W. (2002). Differential mechanisms of action of interferon-beta and glatiramer acetate in MS. Neurology 59(6): 802-808.

Yu, J., Y. Guo, M. Sun, B. Li, Y. Zhang and C. Li (2009). Iron is a potential key mediator of glutamate excitotoxicity in spinal cord motor neurons. Brain Res 1257: 102-107.

Zaaraoui, W., M. Deloire, M. Merle, C. Girard, G. Raffard, M. Biran, M. Inglese, K. G. Petry, O. Gonen, B. Brochet, J. M. Franconi and V. Dousset (2008). Monitoring demyelination and remyelination by magnetization transfer imaging in the mouse brain at 9.4 T. MAGMA 21(5): 357-362.

Zeis, T., U. Graumann, R. Reynolds and N. Schaeren-Wiemers (2008). Normal-appearing white matter in multiple sclerosis is in a subtle balance between inflammation and neuroprotection. Brain 131(Pt 1): 288-303.

Zetterstrom, M., J. Lundkvist, D. Malinowsky, G. Eriksson and T. Bartfai (1998). Interleukin-1-mediated febrile responses in mice and interleukin-1 beta activation of NFkappaB in mouse primary astrocytes, involves the interleukin-1 receptor accessory protein. Eur Cytokine Netw 9(2): 131-138.

Zhang, J., M. V. Jones, M. T. McMahon, S. Mori and P. A. Calabresi (2012). In vivo and ex vivo diffusion tensor imaging of cuprizone-induced demyelination in the mouse corpus callosum. Magn Reson Med 67(3): 750-759.

Zhang, J., Y. Zhang, J. Wang, P. Cai, C. Luo, Z. Qian, Y. Dai and H. Feng (2010a). Characterizing iron deposition in Parkinson's disease using susceptibility-weighted imaging: an in vivo MR study. Brain Res 1330: 124-130.

Zhang, X., M. Haaf, B. Todorich, E. Grosstephan, H. Schieremberg, N. Surguladze and J. R. Connor (2005). Cytokine toxicity to oligodendrocyte precursors is mediated by iron. Glia 52(3): 199-208.

Zhang, Y., L. M. Metz, V. W. Yong and J. R. Mitchell (2010b). 3T deep gray matter T2 hypointensity correlates with disability over time in stable relapsing-remitting multiple sclerosis: a 3-year pilot study. J Neurol Sci 297(1-2): 76-81.

Zheng, W., H. Nichol, S. Liu, Y. C. Cheng and E. M. Haacke (2013). Measuring iron in the brain using quantitative susceptibility mapping and X-ray fluorescence imaging. Neuroimage 78: 68-74.

Zivadinov, R., M. H. Brown, C. V. Schirda, G. U. Poloni, N. Bergsland, C. R. Magnano, J. Durfee, C. Kennedy, E. Carl, J. Hagemeier, R. H. Benedict, B. Weinstock-Guttman and M. G. Dwyer (2012). Abnormal subcortical deep-gray matter susceptibility-weighted imaging filtered phase measurements in patients with multiple sclerosis A case-control study. Neuroimage 59(1): 331-339.

Zivadinov, R., G. U. Poloni, K. Marr, C. V. Schirda, C. R. Magnano, E. Carl, N. Bergsland, D. Hojnacki, C. Kennedy, C. B. Beggs, M. G. Dwyer and B. Weinstock-Guttman (2011). Decreased brain venous vasculature visibility on susceptibility-

weighted imaging venography in patients with multiple sclerosis is related to chronic cerebrospinal venous insufficiency. BMC Neurol 11: 128.

Zivadinov, R., C. Schirda, M. G. Dwyer, M. E. Haacke, B. Weinstock-Guttman, E. Menegatti, M. Heininen-Brown, C. Magnano, A. M. Malagoni, D. S. Wack, D. Hojnacki, C. Kennedy, E. Carl, N. Bergsland, S. Hussein, G. Poloni, I. Bartolomei, F. Salvi and P. Zamboni (2010). Chronic cerebrospinal venous insufficiency and iron deposition on susceptibility-weighted imaging in patients with multiple sclerosis: a pilot case-control study. Int Angiol 29(2): 158-175.